Diploma Thesis

Stresses in a concrete pavement resulting from transient heat conduction: engineering analysis of in situ temperature measurements

submitted in satisfaction of the requirements for the degree of
Diplom-Ingenieur
of the TU Wien, Department of Civil Engineering

Diplomarbeit

Spannungen in einer Betonfahrbahn zufolge instationärer Wärmeleitung: Ingenieurmechanische Analyse von Temperaturfeldmessungen

ausgeführt zum Zwecke der Erlangung des akademischen Grades einer
Diplom-Ingenieurin
eingereicht an der Technischen Universität Wien, Fakultät für Bauingenieurwesen

von

Sophie Schmid, BSc

Matr.Nr.: 01425820

unter der Anleitung von

Univ. Prof. Dipl.-Ing. Dr. techn. **Bernhard Pichler**
Dipl.-Ing. **Rodrigo Díaz Flores**

Institut für Mechanik der Werkstoffe und Strukturen
Technische Universität Wien
Karlsplatz 13/202, 1040 Wien, Österreich

Wien, im November 2020

Abstract

Concrete pavements are subjected to transient heat conduction in thickness direction during most of the time. Stresses resulting from this thermal loading are of great importance for the design of such pavements. This provides the motivation to quantify thermal stresses based on temperature measurements from a field testing site in Lower Austria, at which the temperature inside a concrete pavement was monitored, in autumn 2015, over a period of 23 days. A thermo-elastic analysis is performed. The simulation of heat conduction in thickness direction yields realistic distributions of the temperature across the thickness of the plate. Thermal eigenstrains are computed by multiplying temperature changes with the coefficient of thermal expansion of concrete. Every eigenstrain distribution is subdivided into three parts: its mean value, representing eigenstretches of the plate, its first moment, representing eigencurvatures of the plate, and the spatially nonlinear rest, representing eigendistortions of the generators of the plate. The eigenstretches are free to develop, because of the joints between neighboring plates. The eigencurvatures are constrained by the subgrade on which the plate rests. This results in bending of the plate. Corresponding stress distributions are linear and antisymmetric across the thickness of the plate. These stresses are computed by means of nonlinear Finite Element simulations, whereby the subgrade is accounted for by means of a Winkler foundation. The eigendistortions are prevented, because Kirchhoff's normal hypothesis states that generators of plates remain straight, even if the plate is subjected to transient heat conduction. Thus, the eigendistortions are nullified by mechanical strains of the same size and distribution, but of opposite sign. Linear elasticity is used to translate these mechanical strains to corresponding stresses. Analytical formulae are provided for these stresses. They are distributed nonlinearly across the thickness of the plate, they have a vanishing mean value, and a vanishing first moment. Daily extreme values of total thermal stresses of the monitored plate are typically found in the early morning and in the early afternoon. The daily maxima of the tensile stresses amount to $0.50 \pm 0.17\,\mathrm{MPa}$ at the top and to $0.42 \pm 0.37\,\mathrm{MPa}$ at the bottom of the plate. International codes for pavement design usually consider the effects of thermal eigenstretches and eigencurvatures only, while disregarding the effects of eigendistortions of the plate generators. In the analyzed time interval of 23 days, such a simplified approach is shown to underestimate the daily maxima of tensile stresses at the top of the plate by 22 % and to overestimate these maxima at the bottom of the plate by 45 %. Thus, performing a few additional analytical calculations, such as presented in this study, is inexpensive and has the potential to lead to pavement designs that can be both safer and more economic.

Kurzfassung

Betondecken sind meist instationärer Wärmeleitung in Dickenrichtung ausgesetzt. Spannungen zufolge dieser thermischen Belastung sind für die Bemessung von Betonplatten von großer Bedeutung. Das ist die Motivation, Thermospannungen ausgehend von Temperaturmessungen aus einem Feldversuch in Niederösterreich zu quantifizieren, bei dem die Temperatur innerhalb einer Betonplatte im Herbst 2015 über einen Zeitraum von 23 Tagen gemessen wurde. Eine thermoelastische Analyse wird durchgeführt. Die Simulation der Wärmeleitung in Dickenrichtung ergibt realistische Temperaturverteilungen über die Plattendicke. Thermische Eigenverzerrungen werden durch Multiplikation der Temperaturänderungen mit dem Wärmeausdehnungskoeffizienten von Beton berechnet. Eigenverzerrungsverteilungen werden in drei Teile zerlegt: den Mittelwert, der Eigendehnungen der Platte darstellt, das Moment I. Ordnung, das Eigenverkrümmungen der Platte entspricht, und den räumlich nichtlinearen Rest, der sich auf Eigenverwölbungen der Plattengeneratoren bezieht. Die Eigendehnungen können sich aufgrund der Fugen zwischen benachbarten Platten frei entwickeln. Die Eigenkrümmungen werden durch den Plattenunterbau behindert. Das führt zur Biegung der Platte. Entsprechende Spannungsverteilungen sind linear und antimetrisch über die Plattendicke. Diese Spannungen werden mit nichtlinearen Finite-Elemente-Simulationen berechnet. Der Unterbau wird dabei als Winklerbettung idealisiert. Die Eigenverwölbungen sind zufolge der Kirchhoff'schen Normalenhypothese verhindert. Sie besagt, dass Plattengeneratoren selbst dann gerade bleiben, wenn die Platte instationärer Wärmeleitung ausgesetzt ist. Somit werden die Eigenverwölbungen durch mechanische Dehnungen gleicher Größe und Verteilung, jedoch mit entgegengesetztem Vorzeichen, aufgehoben. Mit der linearen Elastizitätstheorie werden die mechanischen Dehnungen in entsprechende Spannungen übersetzt. Die Spannungen, für die analytische Formeln angegeben werden, sind nichtlinear über die Plattendicke verteilt, haben einen verschwindenden Mittelwert und ein verschwindendes Moment I. Ordnung. Extremwerte der gesamten Thermospannungen der untersuchten Platte werden typischerweise am frühen Morgen und am frühen Nachmittag gefunden. Die täglichen Maxima der Zugspannungen betragen $0{,}50 \pm 0{,}17\,\mathrm{MPa}$ an der Plattenoberseite und $0{,}42 \pm 0{,}37\,\mathrm{MPa}$ an der Unterseite. Internationale Richtlinien für die Fahrbahndimensionierung berücksichtigen normalerweise nur die Auswirkungen von thermischen Eigendehnungen und Eigenkrümmungen, während die Eigenverwölbungen der Plattengeneratoren unberücksichtigt bleiben. Für das untersuchte Zeitintervall von 23 Tagen wird gezeigt, dass ein derart vereinfachter Ansatz die täglichen Zugspannungsmaxima an der Plattenoberseite um 22 % unterschätzt und an der Plattenunterseite um 45 % überschätzt. Die einfachen, zusätzlichen, analytischen Berechnungen, die in dieser Arbeit beschrieben sind, können zu sichereren und wirtschaftlicheren Fahrbahnkonstruktionen führen.

Danksagung / Acknowledgements

Die Erstellung der vorliegenden Diplomarbeit wurde durch das Mitwirken mehrerer Mitarbeiter der Fakultät für Bauingenieurwesen der TU Wien ermöglicht. Allen voran möchte ich mich bei Herrn Univ. Prof. Dipl.-Ing. Dr. techn. Bernhard Pichler für die Hauptbetreuung der Arbeit, für die ausgiebigen fachlichen Diskussionen, die wertvolle sprachliche und inhaltliche Unterstützung sowie die exzellente Zusammenarbeit bedanken. Großer Dank gebührt auch Herrn Dipl.-Ing. Rodrigo Díaz Flores für die kontinuierliche Begleitung sowie den sprachlichen, fachlichen und persönlichen Beistand. Herrn Ass. Prof. Dipl.-Ing. Dr. techn. Lukas Eberhardsteiner sei für das Bereitstellen der Temperaturmessdaten gedankt, Herrn Ass. Prof. Dipl.-Ing. Dr. techn. Mehdi Aminbaghai für die kurzfristige Unterstützung in der Simulation der elastischen Winklerbettung. Dieser Diplomarbeit gingen eine Reihe wissenschaftlicher Diskussionen zu den theoretischen Aspekten der Arbeit voraus, für die ich stellvertretend Herrn Dr. Hui Wang von der Shanghai Jiao Tong University in Shanghai, China, danke.

Meiner Mama Elisabeth und meiner Schwester Katharina danke ich für die großartige und bedingungslose Unterstützung Zeit meines Lebens und im Besonderen während meiner Studienzeit an der TU Wien. Ihr habt mir stets den nötigen Rückhalt, Ausgleich und Rat geboten, den ich für ein gutes Vorankommen benötigt habe. Besonderen Dank möchte ich auch meinem Schwager Florian sowie meinen lieben Freunden und Freundinnen aussprechen.

The present diploma thesis was made possible by the cooperation of several employees of the Department of Civil Engineering of the TU Wien. In particular, I would like to thank Univ. Prof. Dipl.-Ing. Dr. techn. Bernhard Pichler for his supervision of the thesis, for the extensive discussions, the valuable linguistic and content-related support and for the excellent cooperation. Many thanks to Dipl.-Ing. Rodrigo Díaz Flores for his linguistic, technical and personal support. Thank you to Ass. Prof. Dipl.-Ing. Dr. techn. Lukas Eberhardsteiner for providing the data of temperature measurements, and to Ass. Prof. Dipl.-Ing. Dr. techn. Mehdi Aminbaghai for his support in the simulation of the elastic Winkler foundation. A series of scientific discussions preceded this diploma thesis. In representation, I would like to thank Dr. Hui Wang from Shanghai Jiao Tong University, Shanghai, China.

Contents

1 Introduction **8**

2 Engineering Thermo-Mechanical Analysis **11**

2.1 Transient heat conduction in thickness direction 12

2.2 Thermal eigenstrains 13

2.3 Thermal stresses 19

3 Application to temperature measurements from in situ monitoring **20**

3.1 Experimental data from in situ monitoring 20

3.2 Temperature histories at the top and bottom surface 26

3.3 Transient heat conduction in thickness direction 29

3.4 Thermal eigenstrains 32

3.5 Stresses resulting from constrained eigencurvatures of the plate 33

3.6 Stresses resulting from prevented eigendistortions of the generators of the plate . 37

3.7 Total thermal stresses 38

4 Discussion of results obtained for the entire monitoring period **40**

4.1 Bounding envelopes of temperature and stress distributions 40

4.2 Daytime heating is typically faster than nighttime cooling 40

4.3 Tensile stresses and implications for the design of concrete pavements 42

4.4 Sign changes of thermal stresses resulting from daily temperature fluctuations . . 43

4.5 Limitations of the present study and future outlook 44

5 Conclusions **46**

Appendices **48**

A Summary of results: temperature, eigenstrain, and stress distributions **49**

B List of symbols **73**

Chapter 1

Introduction

Concrete pavements are exposed to variable atmospheric conditions. Changes of temperature refer to time scales spanning over several orders of magnitude. The sequence of the seasons results in a yearly rhythm. The alternating arrival of cold fronts and warm fronts refers to characteristic periods of time ranging from a few weeks to a few days. Cycles of days and nights result in a daily rhythm [6, 18]. Transitions from sunshine to sudden precipitation events and vice versa occur sometimes within a few minutes only. Thus, concrete pavements are subjected to transient heat conduction during most of the time.

Concrete pavements consist of plates with characteristic in-plane dimensions of 3 to 5 meters [24]. This is significantly smaller than the characteristic size of weather phenomena, e.g. the width of bands of clouds usually ranges from several hundreds of meters to several dozens of kilometers. Consequently, spatial temperature variations are usually small along the top surface of individual pavement plates. Together with characteristic plate thicknesses ranging from 20 to 30 centimeters, this results in predominantly uniaxial heat conduction in the direction normal to the midplane.

The origin of stress analysis of concrete pavements, including thermal stresses, dates back to pioneering contributions published in the late 1920ies. Westergaard [32] assumed linear stress distributions due to temperature fluctuations. In situ temperature measurements were carried out by Teller and Sutherland as early as in the 1930ies [27]. They observed and documented spatially nonlinear temperature distributions. Thomlinson [28] subdivided, in 1940, the temperature distributions into a constant, a linear, and a nonlinear part, and analyzed the spatially nonlinear stresses resulting from the nonlinear part of the temperature distribution. The development of the Finite Element method opened new possibilities for the design of concrete pavements. Such numerical analyses are capable of accounting, e.g., for dowels connecting neighboring plates and for general distributions of temperature and moisture [5, 17, 26]. Finite Element analysis of multi-layered concrete pavements was carried by Ioannides and Khazanovich [15]. The temperature response and the corresponding vertical and horizontal displacements of concrete pavements were studied by Armaghani et. al. [1]. In the 1990s, nonlinear thermal stresses were approximated, e.g., by quadratic or cubic polynomials [6, 20, 34], including the comparison of computed data with field measurements [20]. Hiller and Roesler [12] compared linear and nonlinear thermal stresses. Finally, Wang et al. [31] introduced a semi-analytical solution for the calculation of nonlinear thermal stresses. In the context of a pavement plate subjected to a hail shower, it turned out that thermal stresses resulting from constrained eigencurvatures are significantly

smaller than the stresses resulting from prevented eigendistortions [31]. However, the findings concerning the thermal effect of nonlinear temperature distribution have not been included yet in the practical application in the field of pavement design, e. g. the US Mechanistic Empirical Pavement Design Guide [23]. Instead of nonlinear distributions, it considers "equivalent" linear temperature gradients in thickness direction of the plate.

The present master thesis is focused on a thermo-mechanical analysis of pavement plates, based on analytical methods and series solutions taken from engineering sciences. This analysis is organized in three steps. The first one refers to the solution of the transient heat conduction problem. Known temperature histories referring to the top and bottom surfaces of the plate of interest enter the analysis as input. This provides access to the chronological development of the temperature distribution along the thickness of concrete pavements. The second step of the thermo-mechanical analysis refers to the quantification of eigenstrains and mechanical strains (= stress-related strains). The chronological development of the thermal eigenstrain distribution along the thickness of concrete pavements is computed by multiplying the thermal expansion coefficient of concrete with temperature changes. At every time instant of the analysis, the obtained eigenstrain profile is spatially nonlinear along the thickness direction. It is decomposed into three contributions.

- The first one is spatially constant. It represents the mean value of the eigenstrain profile and can be interpreted as an eigenstretch of the plate.
- The second contribution is spatially linear with a vanishing mean value. It represents the first moment of the eigenstrain profile and can be interpreted as an eigencurvature of the plate.
- The third contribution is the spatially nonlinear rest of the eigenstrain profile. It has a vanishing mean value, a vanishing first moment, and it can be interpreted as an eigendistortion of the generators of the plate.

The final third step of the thermo-mechanical analysis refers to quantifying contributions to the total thermal stresses:

- The thermal eigenstretch of the plate is free to develop, because of the joints between neighboring plates. Thus, no thermal stresses are activated.
- The thermal eigencurvature of the plate is constrained by the subgrade on which the plate rests. Thus, bending stresses are activated. The subgrade is usually modeled by means of an elastic Winkler foundation [33]. The latter is only active when the plate is pressed against the foundation [9, 13, 21]. It is inactive, if the plate lifts off from the Winkler foundation. The region, in which contact between the plate and the subgrade is lost, is a priori unknown. Thus, computing thermal stresses resulting from constrained eigencurvatures of a plate represents a nonlinear contact problem. It needs to be solved iteratively, usually by means of nonlinear Finite Element simulations.

- Thermal eigendistortions of the generators of the plate are prevented, because the generators of the plate remain straight even if the plate is subjected to transient heat conduction [31]. Thus, the eigendistortions are nullified by mechanical strains of the same size and distribution, but of opposite sign. These mechanical strains are translated, based on the theory of linear elasticity, into thermal stresses.

In order to show the significance of nonlinear temperature distributions and corresponding thermal stresses, the theoretical developments are exemplarily applied to temperature measurements from in situ monitoring of a concrete plate which is part of the highway "A2 – Süd Autobahn" in Austria. Structural monitoring took place during three weeks in September and October 2015. Every 60 minutes, the temperature was measured in depths amounting to 5 cm, 10 cm, 15 cm, and 20 cm under the top surface of the plate. The thermo-mechanical analysis starts with identifying the numerical value of the thermal conductivity of concrete, which ensures that the temperature measurements are reproduced in a best-possible fashion. After that, the thermal stresses are computed as described above.

The present master thesis is organized as follows. Chapter 2 refers to the mechanical fundamentals of the described thermo-mechanical analysis. Chapter 3 is devoted to exemplary application of the theoretical developments, Chapter 4 to the discussion of the results, and Chapter 5 to the conclusions drawn from the presented analysis.

Chapter 2

Engineering Thermo-Mechanical Analysis

The following engineering thermo-mechanical analysis is designed to be both "as simple as possible" and "as complex as necessary". This requires simplifying assumptions. As far as the analyzed structure is concerned, they read as follows. Plates with constant thickness h are analyzed, whereby h is significantly smaller than the in-plane dimensions, say the length l_x and the width l_y of a rectangular plate, see Fig. 2.1. Points within the volume V and at the

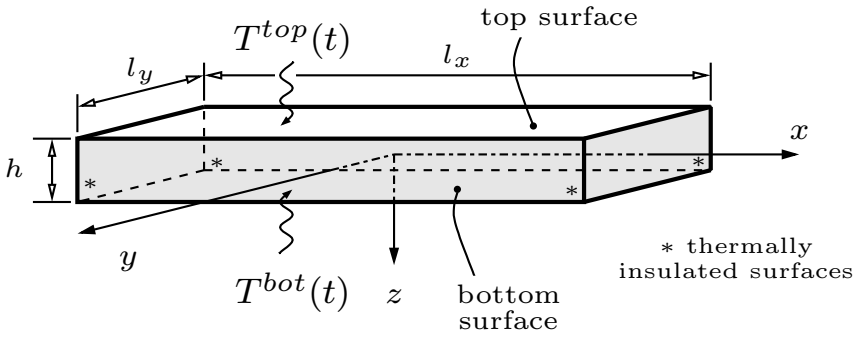

Fig. 2.1: One dimensional heat conduction within a plate in thickness-direction.

boundary S of the plate are described by a Cartesian coordinate system. Its origin is located at the center of gravity of the plate. The x- and y-axes resolve the midplane of the plate. The z-axis runs along the thickness direction and is oriented downwards. Thus, $z = +h/2$ describes the bottom surface of the plate, and $z = -h/2$ the upper surface. For later reference, it is noted that

$$\int_{-\frac{h}{2}}^{+\frac{h}{2}} z \; \mathrm{d}z = 0 \tag{2.1}$$

and

$$\int_{-\frac{h}{2}}^{+\frac{h}{2}} z^2 \; \mathrm{d}z = \frac{h^3}{12} \,. \tag{2.2}$$

The plate rests on a Winkler foundation and is made from a homogeneous and isotropic material. Thus, material properties are constant throughout the structure, e.g. the thermal diffusivity a, the thermal expansion coefficient α_T, the modulus of elasticity E, and Poisson's ratio ν.

2.1 Transient heat conduction in thickness direction

Heat conduction is a spatio-temporal problem, representing an initial and boundary value problem. The field equation, the initial condition, and the boundary conditions are described next.

The field equation is the heat equation. Because of the reasons described in the first two paragraphs of Chapter 1, the present analysis is focused on transient heat conduction along the thickness direction. Denoting the temperature as T and the time variable as t, the field equation reads as

$$\frac{\partial T(z,t)}{\partial t} - a\,\frac{\partial^2 T(z,t)}{\partial z^2} = 0\,, \qquad \forall\ z \in V\,. \tag{2.3}$$

The initial condition is an isothermal state at the reference temperature T_{ref}:

$$T(z, t{=}0) = T_{ref}\,. \tag{2.4}$$

Boundary conditions are either defined in terms of the heat flux or the temperature. The heat flux is set equal to zero at the lateral surfaces, in agreement with the idealization of one-dimensional heat transfer in thickness direction. Known temperature histories are prescribed at the remaining top and bottom surfaces. There, it is assumed that the temperature is spatially uniform but variable in time, as described by the functions $T^{top}(t)$ and $T^{bot}(t)$:

$$T(z{=}-\tfrac{h}{2}, t) \;=\; T^{top}(t)\,, \tag{2.5}$$
$$T(z{=}+\tfrac{h}{2}, t) \;=\; T^{bot}(t)\,. \tag{2.6}$$

In order to render an analytical series solution possible, the histories of the surface temperature are approximated by a superposition of temperature steps, mathematically described based on the Heaviside function $H(t - t_i)$. The latter is equal to 0 if $t < t_i$, and it is equal to 1 if $t \geq t_i$:

$$T(z{=}-\tfrac{h}{2}, t) \;=\; T_{ref} + \sum_{i=1}^{N_i} \Delta T_i^{top}\, H(t - t_i)\,, \tag{2.7}$$
$$T(z{=}+\tfrac{h}{2}, t) \;=\; T_{ref} + \sum_{i=1}^{N_i} \Delta T_i^{bot}\, H(t - t_i)\,, \tag{2.8}$$

see also Fig. 2.2. In Eqs. (2.7) and (2.8), N_i denotes the number of considered temperature steps, ΔT_i^{top} the i^{th} temperature step at the top surface, and ΔT_i^{bot} the i^{th} temperature step at the bottom surface. The temperature steps follow from the temperature histories (2.5) and (2.6) as

$$\Delta T_i^{top} \;=\; T^{top}(t_i) - T^{top}(t_{i-1})\,, \tag{2.9}$$
$$\Delta T_i^{bot} \;=\; T^{bot}(t_i) - T^{bot}(t_{i-1})\,, \tag{2.10}$$

with $T^{top}(t_0) = T^{bot}(t_0) = T_{ref}$.

The solution for one temperature step prescribed at one of the two opposite surfaces is documented in the literature, e.g. [4] analyzed a concrete beam subjected to one temperature

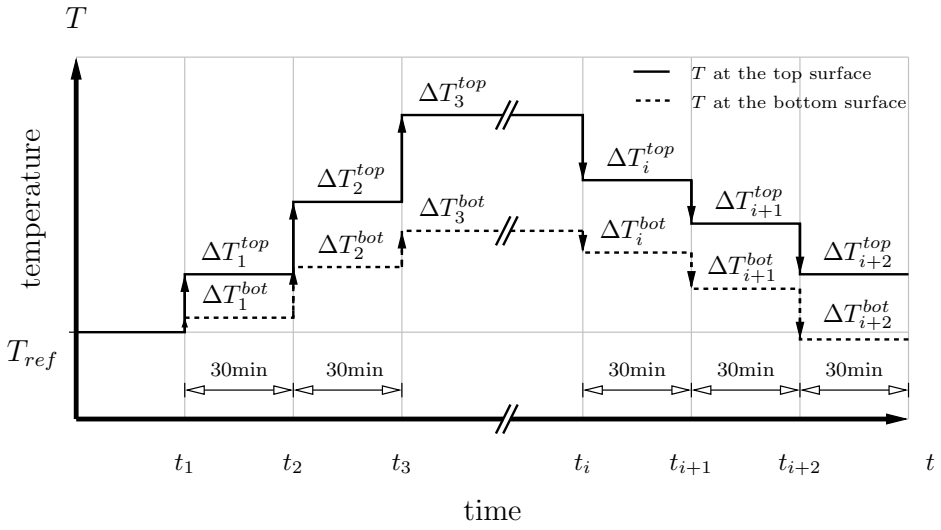

Fig. 2.2: Approximation of continuous temperature histories at the top and bottom surfaces of the plate by means of step functions, starting from the reference temperature T_{ref}.

step at the top, and a constant temperature at the bottom. Because of the linearity of the heat equation (2.3), such elementary solutions can be superimposed in order to solve the problem of many temperature steps, e.g. [31] analyzed a pavement plate subjected to a series of temperature steps at the top surface, and a constant temperature at the bottom. Herein, the solution of [31] is further extended in order to account for a series of temperature steps both at the top *and* the bottom surface. This extended solution reads as

$$\begin{aligned} T(z,t) \;=\; & T_{ref} + \sum_{i=1}^{N_i} \Delta T_i^{bot} + \left(\Delta T_i^{top} - \Delta T_i^{bot}\right)\left[\left(\frac{1}{2} - \frac{z}{h}\right)\right. \\ & \left. - \sum_{n=1}^{\infty} \frac{(-1)^n}{n\pi} \sin\left(\frac{2n\pi z}{h}\right) \exp\left(-(2n\pi)^2 \frac{a\langle t - t_i\rangle}{h^2}\right)\right] \\ & + \left(\Delta T_i^{top} + \Delta T_i^{bot}\right) \sum_{n=1}^{\infty} \frac{2(-1)^n}{(2n-1)\pi} \cos\left(\frac{(2n-1)\pi z}{h}\right) \exp\left(-(2n-1)^2\pi^2 \frac{a\langle t - t_i\rangle}{h^2}\right), \end{aligned} \tag{2.11}$$

where the angled brackets denote the Macaulay operator:

$$\langle t - t_i\rangle := \frac{1}{2}\Big(t - t_i + |t - t_i|\Big)\,. \tag{2.12}$$

2.2 Thermal eigenstrains

Thermal eigenstrains are equal to the coefficient of thermal expansion, α_T, multiplied with the change of temperature, measured relative to the reference configuration, herein: $\Delta T(z,t) = T(z,t) - T_{ref}$:

$$\varepsilon_{xx}^e = \varepsilon_{yy}^e = \varepsilon_{zz}^e = \alpha_T \Delta T\,, \tag{2.13}$$

with

$$\begin{aligned}\alpha_T \Delta T \;=\; & \alpha_T \sum_{i=1}^{N_i} \Delta T_i^{bot} + \Bigg[\left(\Delta T_i^{top} - \Delta T_i^{bot} \right) \Bigg[\left(\frac{1}{2} - \frac{z}{h} \right) \\ & - \sum_{n=1}^{\infty} \frac{(-1)^n}{n\pi} \sin\left(\frac{2n\pi z}{h} \right) \exp\left(-(2n\pi)^2 \frac{a\langle t - t_i \rangle}{h^2} \right) \Bigg] \\ & + \left(\Delta T_i^{top} + \Delta T_i^{bot} \right) \sum_{n=1}^{\infty} \frac{2(-1)^n}{(2n-1)\pi} \cos\left(\frac{(2n-1)\pi z}{h} \right) \exp\left(-(2n-1)^2 \pi^2 \frac{a\langle t - t_i \rangle}{h^2} \right) \Bigg] . \end{aligned} \tag{2.14}$$

Notably, Eq. (2.14) is independent of the reference temperature. The thermal eigenstrains are spatially nonlinear along the thickness direction, because transient heat conduction goes along with spatially nonlinear temperature distributions, see Eq. (2.14).

When it comes to the quantification of thermal stresses, the question must be answered whether the eigenstrains are free to develop, constrained, or prevented [31]. This question must be answered partly at the larger level of the plate, and partly at the smaller level of the generators of the plate representing material points on a straight line normal to the midplane of the plate, in its initial configuration. To this end, the spatially nonlinear eigenstrains are subdivided into three parts. They refer to an eigenstretch of the plate, an eigencurvature of the plate, and an eigendistortion of the generators of the plate [31]. In the interest of clarity, this decomposition is derived in a step-by-step fashion.

The first step refers to the kinematics of the Kirchhoff theory for thin plates [19]:

$$u = u_m - \frac{\partial w_m}{\partial x} z , \tag{2.15}$$

$$v = v_m - \frac{\partial w_m}{\partial y} z , \tag{2.16}$$

$$w = w_m , \tag{2.17}$$

where u, v, and w denote the displacement components in x-, y- and z-direction, at any point of the plate. u_m, v_m, and w_m denote the displacement components at the midplane, hence the subscript "m". Eqs. (2.15)–(2.17) essentially describe that generators of the plate remain straight and normal to the tangential plane of the midsurface of the plate, also in the deformed configuration (= Kirchhoff's normal hypothesis), see also Fig. 2.3.

The second step refers to "total" normal strain components ε_{xx} and ε_{yy} of the linearized strain tensor. They are defined as

$$\varepsilon_{xx} = \frac{\partial u}{\partial x} , \tag{2.18}$$

$$\varepsilon_{yy} = \frac{\partial v}{\partial y} . \tag{2.19}$$

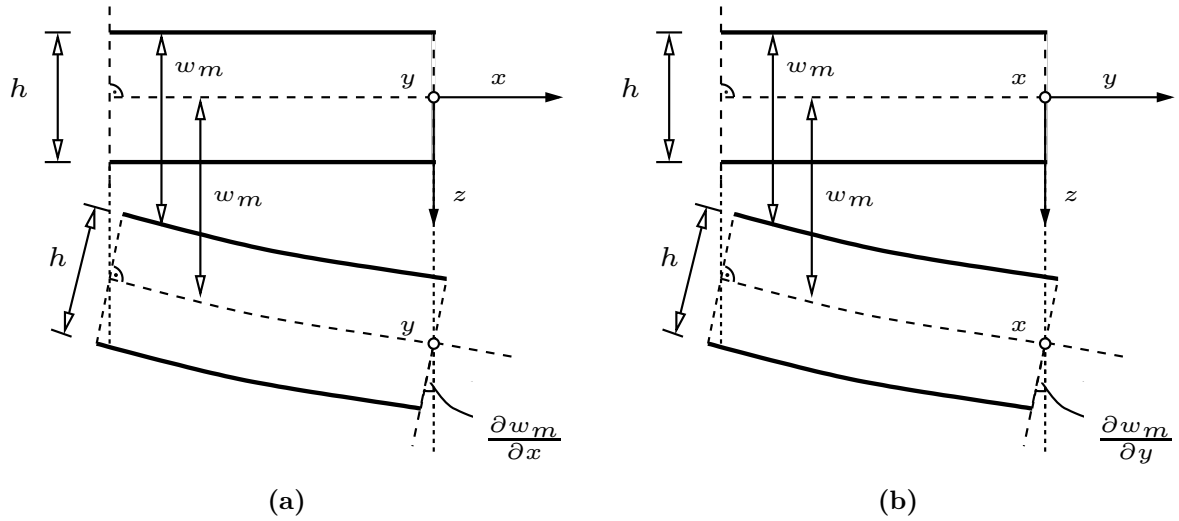

(a) **(b)**

Fig. 2.3: Kinematic description of the deformed configuration of a thin plate based in the Kirchhoff's normal hypothesis; after Fig. 8.13 in [19].

Inserting Eqs. (2.15) and (2.16) into Eqs. (2.18) and (2.19) yields

$$\varepsilon_{xx} = \frac{\partial u_m}{\partial x} - \frac{\partial^2 w_m}{\partial x^2} z \,, \tag{2.20}$$

$$\varepsilon_{yy} = \frac{\partial v_m}{\partial y} - \frac{\partial^2 w_m}{\partial y^2} z \,. \tag{2.21}$$

Eqs. (2.20) and (2.21) are usually reformulated in terms of stretches of the midsurface, $\varepsilon_{m,x}$ and $\varepsilon_{m,y}$, and curvatures of the midsurface, $\kappa_{m,x}$ and $\kappa_{m,y}$. This yields

$$\varepsilon_{xx} = \varepsilon_{m,x} + \kappa_{m,x} z \,, \tag{2.22}$$

$$\varepsilon_{yy} = \varepsilon_{m,y} + \kappa_{m,y} z \,. \tag{2.23}$$

The third step refers to normal stress components σ_{xx} and σ_{yy} of Cauchy's stress tensor. In thermoelasticity, they read as

$$\sigma_{xx} = \frac{E}{1-\nu^2}\left[\varepsilon_{xx} - \varepsilon^e_{xx} + \nu\left(\varepsilon_{yy} - \varepsilon^e_{yy}\right)\right], \tag{2.24}$$

$$\sigma_{yy} = \frac{E}{1-\nu^2}\left[\varepsilon_{yy} - \varepsilon^e_{yy} + \nu\left(\varepsilon_{xx} - \varepsilon^e_{xx}\right)\right]. \tag{2.25}$$

Inserting Eqs. (2.13), (2.22), and (2.23) into (2.24) and (2.25) yields

$$\sigma_{xx} = \frac{E}{1-\nu^2}\Big[\varepsilon_{m,x} + \kappa_{m,x}\, z - \alpha_T \Delta T + \nu\left(\varepsilon_{m,y} + \kappa_{m,y}\, z - \alpha_T \Delta T\right)\Big], \tag{2.26}$$

$$\sigma_{yy} = \frac{E}{1-\nu^2}\Big[\varepsilon_{m,y} + \kappa_{m,y}\, z - \alpha_T \Delta T + \nu\left(\varepsilon_{m,x} + \kappa_{m,x}\, z - \alpha_T \Delta T\right)\Big]. \tag{2.27}$$

The fourth step refers to normal forces per unit length n_{xx} and n_{yy}. They are energetically conjugate to the displacements u_m and v_m and read as [13]

$$n_{xx} = \int_{-\frac{h}{2}}^{+\frac{h}{2}} \sigma_{xx}\ \mathrm{d}z\,, \tag{2.28}$$

$$n_{yy} = \int_{-\frac{h}{2}}^{+\frac{h}{2}} \sigma_{yy}\ \mathrm{d}z\,. \tag{2.29}$$

Inserting Eqs. (2.26) and (2.27) into (2.28) and (2.29) yields under consideration of (2.1)

$$n_{xx} = \frac{Eh}{1-\nu^2}\left[\varepsilon_{m,x} - \frac{1}{h}\int_{-\frac{h}{2}}^{+\frac{h}{2}} \alpha_T \Delta T\ \mathrm{d}z + \nu\left(\varepsilon_{m,y} - \frac{1}{h}\int_{-\frac{h}{2}}^{+\frac{h}{2}} \alpha_T \Delta T\ \mathrm{d}z\right)\right], \tag{2.30}$$

$$n_{yy} = \frac{Eh}{1-\nu^2}\left[\varepsilon_{m,y} - \frac{1}{h}\int_{-\frac{h}{2}}^{+\frac{h}{2}} \alpha_T \Delta T\ \mathrm{d}z + \nu\left(\varepsilon_{m,x} - \frac{1}{h}\int_{-\frac{h}{2}}^{+\frac{h}{2}} \alpha_T \Delta T\ \mathrm{d}z\right)\right]. \tag{2.31}$$

Eqs. (2.30) and (2.31) are the motivation to introduce the eigenstretch of the midsurface of the plate as

$$\varepsilon_m^e = \frac{1}{h}\int_{-\frac{h}{2}}^{+\frac{h}{2}} \alpha_T \Delta T\ \mathrm{d}z\,. \tag{2.32}$$

Inserting Eq. (2.32) in Eqs. (2.30) and (2.31) yields

$$n_{xx} = \frac{Eh}{1-\nu^2}\left[\varepsilon_{m,x} - \varepsilon_m^e + \nu\left(\varepsilon_{m,y} - \varepsilon_m^e\right)\right], \tag{2.33}$$

$$n_{yy} = \frac{Eh}{1-\nu^2}\left[\varepsilon_{m,y} - \varepsilon_m^e + \nu\left(\varepsilon_{m,x} - \varepsilon_m^e\right)\right]. \tag{2.34}$$

The fifth step refers to bending moments per unit length m_{xx} and m_{yy}. They are energetically conjugate to the rotations $\partial w_m/\partial y$ and $\partial w_m/\partial x$ and read as [13]

$$m_{xx} = \int_{-\frac{h}{2}}^{+\frac{h}{2}} \sigma_{xx}\, z \;\mathrm{d}z\,, \tag{2.35}$$

$$m_{yy} = \int_{-\frac{h}{2}}^{+\frac{h}{2}} \sigma_{yy}\, z \;\mathrm{d}z\,. \tag{2.36}$$

Inserting Eqs. (2.26) and (2.27) into (2.35) and (2.36) yields under consideration of Eqs. (2.1) and (2.2)

$$m_{xx} = \frac{Eh^3}{12(1-\nu^2)}\left[\kappa_{m,x} - \frac{12}{h^3}\int_{-\frac{h}{2}}^{+\frac{h}{2}} \alpha_T \Delta T\, z \;\mathrm{d}z + \nu\left(\kappa_{m,y} - \frac{12}{h^3}\int_{-\frac{h}{2}}^{+\frac{h}{2}} \alpha_T \Delta T\, z \;\mathrm{d}z\right)\right], \tag{2.37}$$

$$m_{yy} = \frac{Eh^3}{12(1-\nu^2)}\left[\kappa_{m,y} - \frac{12}{h^3}\int_{-\frac{h}{2}}^{+\frac{h}{2}} \alpha_T \Delta T\, z \;\mathrm{d}z + \nu\left(\kappa_{m,x} - \frac{12}{h^3}\int_{-\frac{h}{2}}^{+\frac{h}{2}} \alpha_T \Delta T\, z \;\mathrm{d}z\right)\right]. \tag{2.38}$$

Eqs. (2.37) and (2.38) are the motivation to introduce the eigencurvature of the midsurface of the plate as

$$\kappa_m^e = \frac{12}{h^3}\int_{-\frac{h}{2}}^{+\frac{h}{2}} \alpha_T \Delta T\, z \;\mathrm{d}z\,. \tag{2.39}$$

Inserting Eq. (2.39) in Eqs. (2.37) and (2.38) yields

$$m_{xx} = \frac{Eh^3}{12(1-\nu^2)}\left[\kappa_{m,x} - \kappa_m^e + \nu\left(\kappa_{m,y} - \kappa_m^e\right)\right], \tag{2.40}$$

$$m_{yy} = \frac{Eh^3}{12(1-\nu^2)}\left[\kappa_{m,y} - \kappa_m^e + \nu\left(\kappa_{m,x} - \kappa_m^e\right)\right]. \tag{2.41}$$

The completed derivation underlines that the spatially nonlinear eigenstrain distribution $\alpha_T \Delta T$ can be decomposed into three contributions:

$$\alpha_T \Delta T = \varepsilon_m^e + \kappa_m^e\, z + \varepsilon_{dist}^e\,, \tag{2.42}$$

see also Fig. 2.4. In Eq. (2.42), ε^e_m denotes a spatially constant contribution which is equal to the mean value of the eigenstrain distribution, see Eq. (2.32). It can be interpreted as an eigenstretch of the plate. ε^e_m follows from inserting (2.14) into (2.32) as

$$\varepsilon^e_m = \sum_{i=1}^{N_i} \alpha_T (\Delta T_i^{bot} + \Delta T_i^{top}) \left[\frac{1}{2} - \sum_{n=1}^{\infty} \frac{4}{(2n-1)^2 \pi^2} \exp\left(-(2n-1)^2 \pi^2 \frac{a\langle t - t_i \rangle}{h^2} \right) \right]. \tag{2.43}$$

In Eq. (2.42), $\kappa^e_m\, z$ denotes a spatially linear contribution with vanishing mean value. It refers to the first moment of the eigenstrain distribution, see Eq. (2.39), and it can be interpreted as an eigencurvature of the plate. κ^e_m follows from inserting (2.14) into (2.39) as

$$\kappa^e_m = \sum_{i=1}^{N_i} \frac{\alpha_T}{h} (\Delta T_i^{bot} - \Delta T_i^{top}) \left[1 - \sum_{n=1}^{\infty} \frac{6}{n^2 \pi^2} \exp\left(-(2n\pi)^2 \frac{a\langle t - t_i \rangle}{h^2} \right) \right]. \tag{2.44}$$

In Eq. (2.42), ε^e_{dist} denotes the spatially nonlinear rest of the eigenstrain distribution, with vanishing mean value and vanishing first moment. It can be interpreted as an eigendistortion of the generators of the plate.

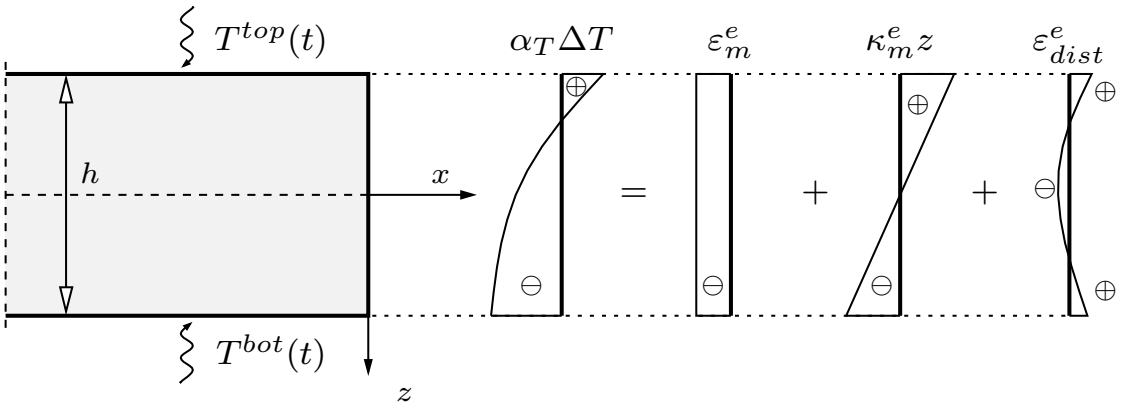

Fig. 2.4: Decomposition of thermal eigenstrains into three parts: (i) a spatially constant part, ε^e_m, which is equal to the mean value of the eigenstrain distribution and which can be interpreted as an eigenstretch of the plate, (ii) a spatially linear part with a vanishing mean value, $\kappa^e_m\, z$, which represents the first moment of the eigenstrain distribution and which can be interpreted as an eigencurvature of the plate, and (iii) the spatially nonlinear rest of the eigenstrain distribution, ε^e_{dist}, which has a vanishing mean value, a vanishing first moment, and which can be interpreted as an eigendistortion of the generators of the plate.

2.3 Thermal stresses

Thermal stresses are activated provided that thermal eigenstrains are restrained or prevented.

- The eigenstretch results in an in-plane expansion or contraction of the plate. This is unconstrained, because of the joints between neighboring plates. Thus, ε_m^e does not activate thermal stresses.
- The eigencurvature results in a convex or concave warping of the plate. This is restrained by the foundation on which the plate rests. Thermal stresses resulting from κ_m^e show a linear distribution in thickness direction and can be computed semi-analytically [13] or by means of a nonlinear Finite element simulation.
- Nonlinear eigenstrains ε_{dist}^e correspond to eigendistortions of the generators of the plates. This eigendistortion is prevented, because the generators of the plate remain straight even if the plate is subjected to transient heat conduction, see Eqs. (2.15)–(2.17). Thus, the eigendistortions are nullified by mechanical strains of the same size and distribution, but of opposite sign. This can be derived as follows.

Eqs. (2.33), (2.34), (2.40), and (2.41) are re-arranged as

$$\varepsilon_{m,x} + \nu\,\varepsilon_{m,y} = n_{xx}\frac{(1-\nu)^2}{Eh} + (1+\nu)\,\varepsilon_m^e\,, \tag{2.45}$$

$$\varepsilon_{m,y} + \nu\,\varepsilon_{m,x} = n_{yy}\frac{(1-\nu)^2}{Eh} + (1+\nu)\,\varepsilon_m^e\,, \tag{2.46}$$

$$\kappa_{m,x} + \nu\,\kappa_{m,y} = m_{xx}\frac{(1-\nu)^2}{Eh^3/12} + (1+\nu)\,\kappa_m^e\,, \tag{2.47}$$

$$\kappa_{m,y} + \nu\,\kappa_{m,x} = m_{yy}\frac{(1-\nu)^2}{Eh^3/12} + (1+\nu)\,\kappa_m^e\,. \tag{2.48}$$

Inserting Eqs. (2.45) and (2.47) into Eq. (2.26), as well as of Eqs. (2.46) and (2.48) into Eq. (2.27) yields

$$\sigma_{xx} = \frac{n_{xx}}{h} + \frac{m_{xx}}{h^3/12}\,z - \frac{E}{1-\nu}\Big(\alpha_T\Delta T - \varepsilon_m^e - \kappa_m^e z\Big)\,, \tag{2.49}$$

$$\sigma_{yy} = \frac{n_{yy}}{h} + \frac{m_{yy}}{h^3/12}\,z - \frac{E}{1-\nu}\Big(\alpha_T\Delta T - \varepsilon_m^e - \kappa_m^e z\Big)\,. \tag{2.50}$$

Thus, thermal stresses resulting from prevented eigendistortion of the generators of the plate read as

$$\sigma_T(\varepsilon_{dist}^e) = -\frac{E}{1-\nu}\Big(\alpha_T\Delta T - \varepsilon_m^e - \kappa_m^e z\Big)\,. \tag{2.51}$$

The expression in the round bracket of Eq. (2.51) is equal to the nonlinear part of the eigenstrains, ε_{dist}^e, see Eq. (2.42).

Chapter 3

Application to temperature measurements from in situ monitoring

The engineering thermo-mechanical analysis of Chapter 2 is applied to a concrete pavement plate which is part of a highway in the eastern part of Austria.

3.1 Experimental data from in situ monitoring

Field measurements refer to a concrete plate with a thickness

$$h = 25\,\text{cm}\,. \tag{3.1}$$

The plate is located at kilometer 21 of highway "A2 – Süd Autobahn", near the junction *Bad Vöslau*, in Lower Austria, see Fig. 3.1.

Fig. 3.1: Location of the analyzed concrete plate at kilometer 21 of the highway "A2 – Süd Autobahn", near Bad Vöslau in Lower Austria [3].

The objective of the installation of the field testing site was to monitor the daily temperature fluctuations in the concrete plate. As for the installation of temperature sensors of type "PT100A", four cuts with depths amounting to 5 cm, 10 cm, 15 cm, and 20 cm, respectively, were produced

using a diamond-tooth saw, see Fig. 3.2 (a). One sensor was placed at the bottom of each cut. Each sensor was connected to a data logger inside a nearby switch box, see Fig. 3.2 (b). The connecting cables were placed inside the cuts until they reached the lateral edge of the plate. From there on, they were running above ground to the data logger. Finally, the cuts were closed using the resin "Roadplast", see Fig. 3.2 (c).

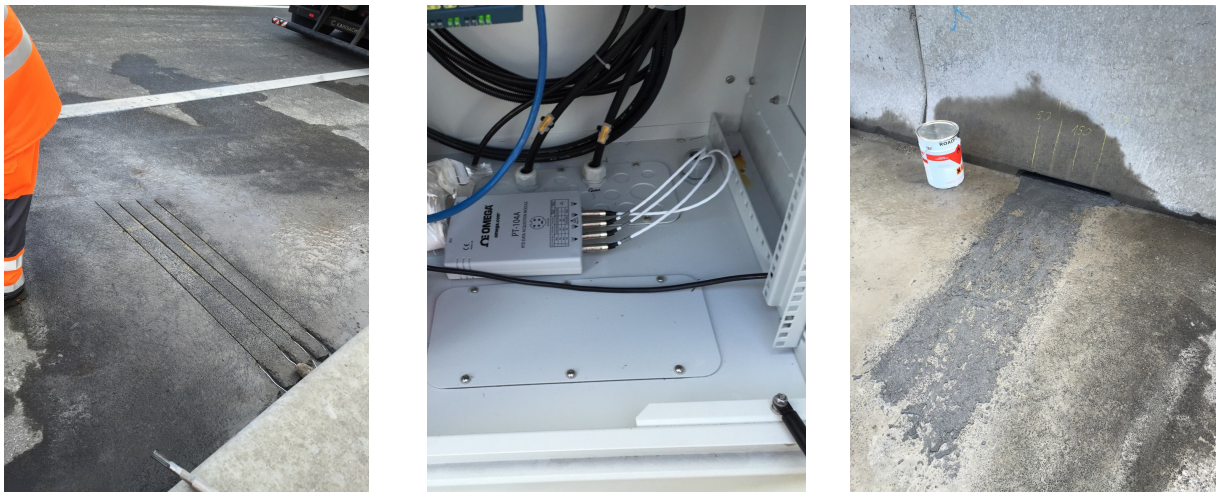

(a) **(b)** **(c)**

Fig. 3.2: Photos from the field testing site: (a) cuts hosting the temperature sensors and their cables, (b) view into the switch box containing the data logger, and (c) situation after closing the cuts with a resin; reproduction of photos from [8] with the permission of Dr. Lukas Eberhardsteiner.

Once every hour, the temperature measurements were recorded, from Wednesday, September 23, to Thursday, October 15, 2015, see Figs. 3.3 to 3.6. Therein, circles label the recorded temperature measurements. The continuous graphs represent splines reproducing the actual measurements and interpolating between them.

The temperature histories reflect the changing weather conditions at the field testing site in September and October 2015 [29].

- Significant daily variations of temperature are observed, similar to the findings of [6, 10, 11, 18, 25]. Usually, the temperature started to increase around 7 o'clock in the morning. The highest temperature was typically measured between 2 and 4 o'clock in the afternoon, followed by a decrease of the temperature until the next morning.

- The size of the daily temperature amplitudes depends on the general weather situation. Sunny conditions in September 2015 resulted in significant daily temperature changes. Rainy weather in the second week of October resulted in almost constant temperatures throughout the plate.

It is also noteworthy that the fluctuations of temperature decrease with increasing depth.

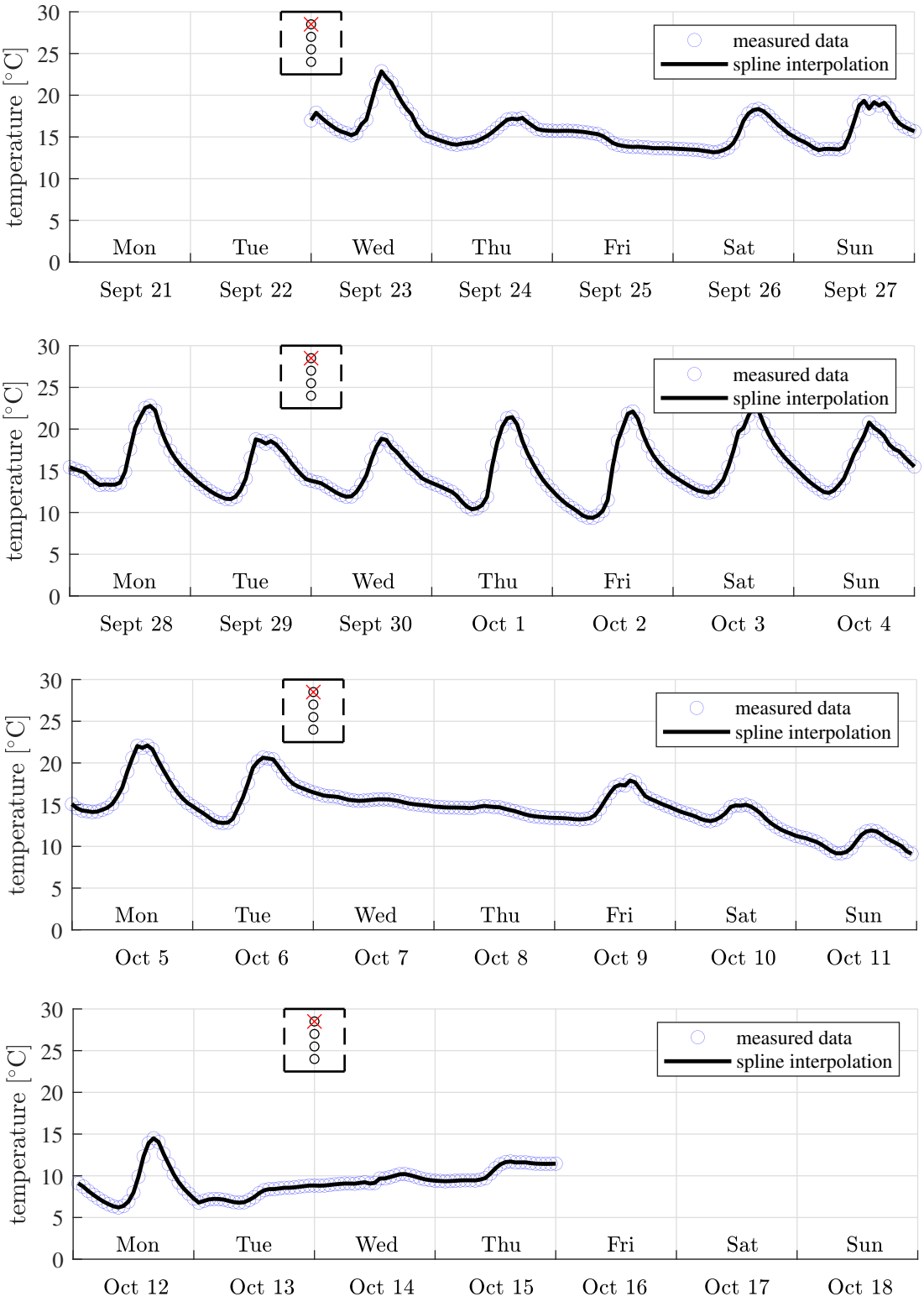

Fig. 3.3: Temperature evolution measured 5 cm underneath the top surface.

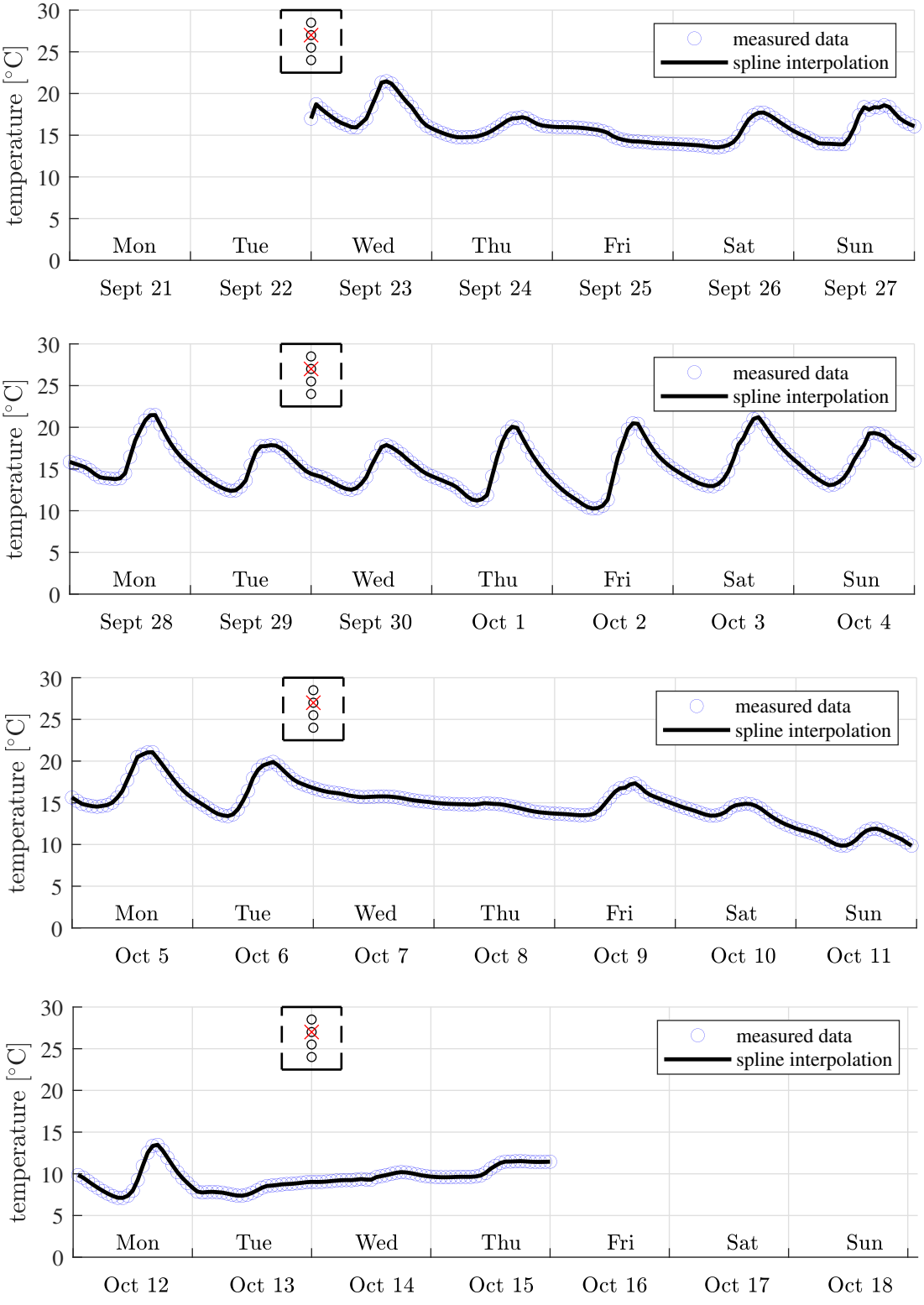

Fig. 3.4: Temperature evolution measured 10 cm underneath the top surface.

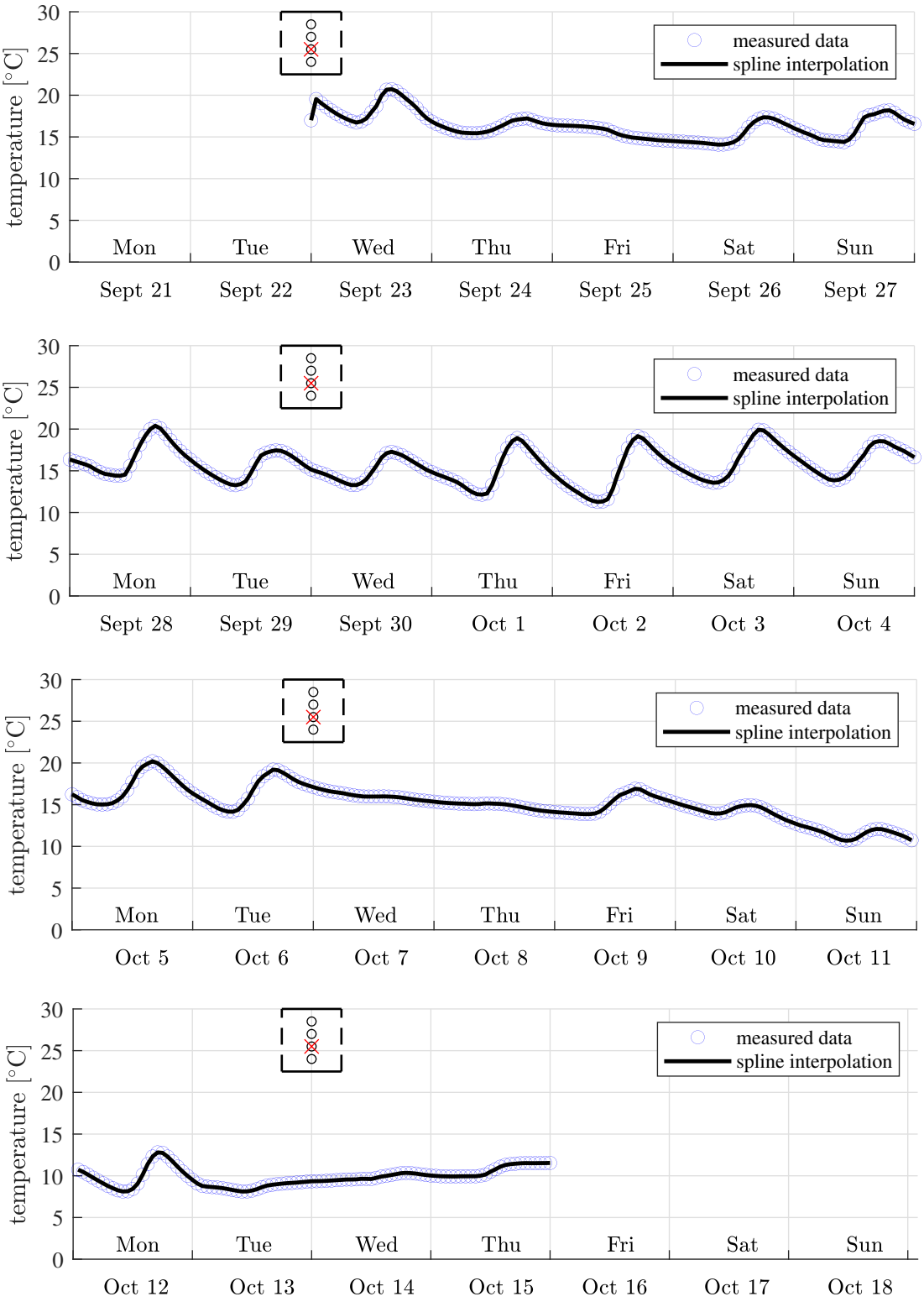

Fig. 3.5: Temperature evolution measured 15 cm underneath the top surface.

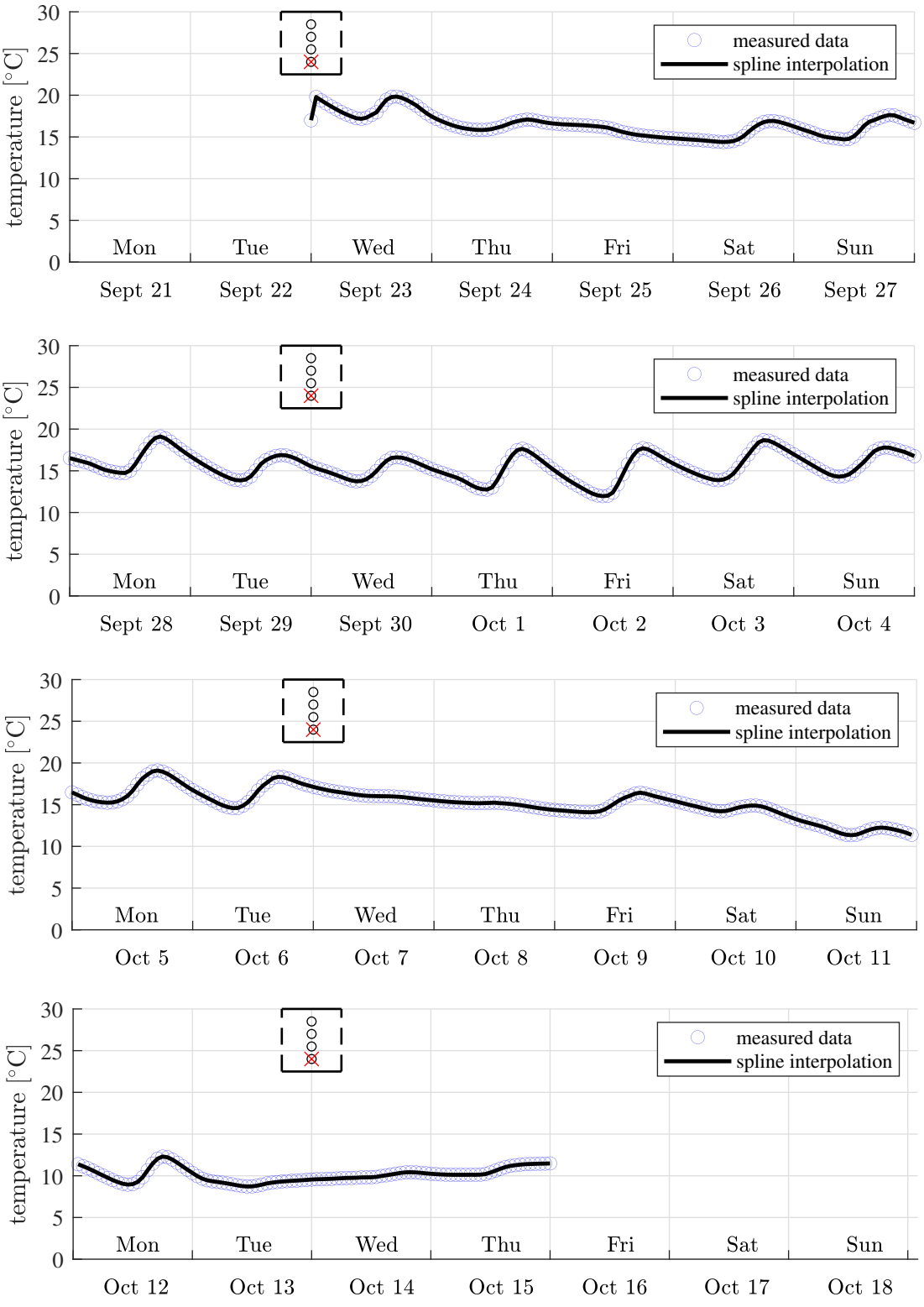

Fig. 3.6: Temperature evolution measured 20 cm underneath the top surface.

3.2 Temperature histories at the top and bottom surface

The temperature histories at the top and bottom surfaces of the plate are input to the thermo-mechanical analysis of Chapter 2. They are reconstructed by means of spatial extrapolation of available measurement data. For every time instant of available temperature measurements, the readings of the three topmost sensors are extrapolated quadratically along the vertical axis to the top surface, see Figs. 3.7 (a) and 3.8, and the readings of the two bottommost sensors are extrapolated linearly to the bottom surface [25], see Figs. 3.7 (b) and 3.9.

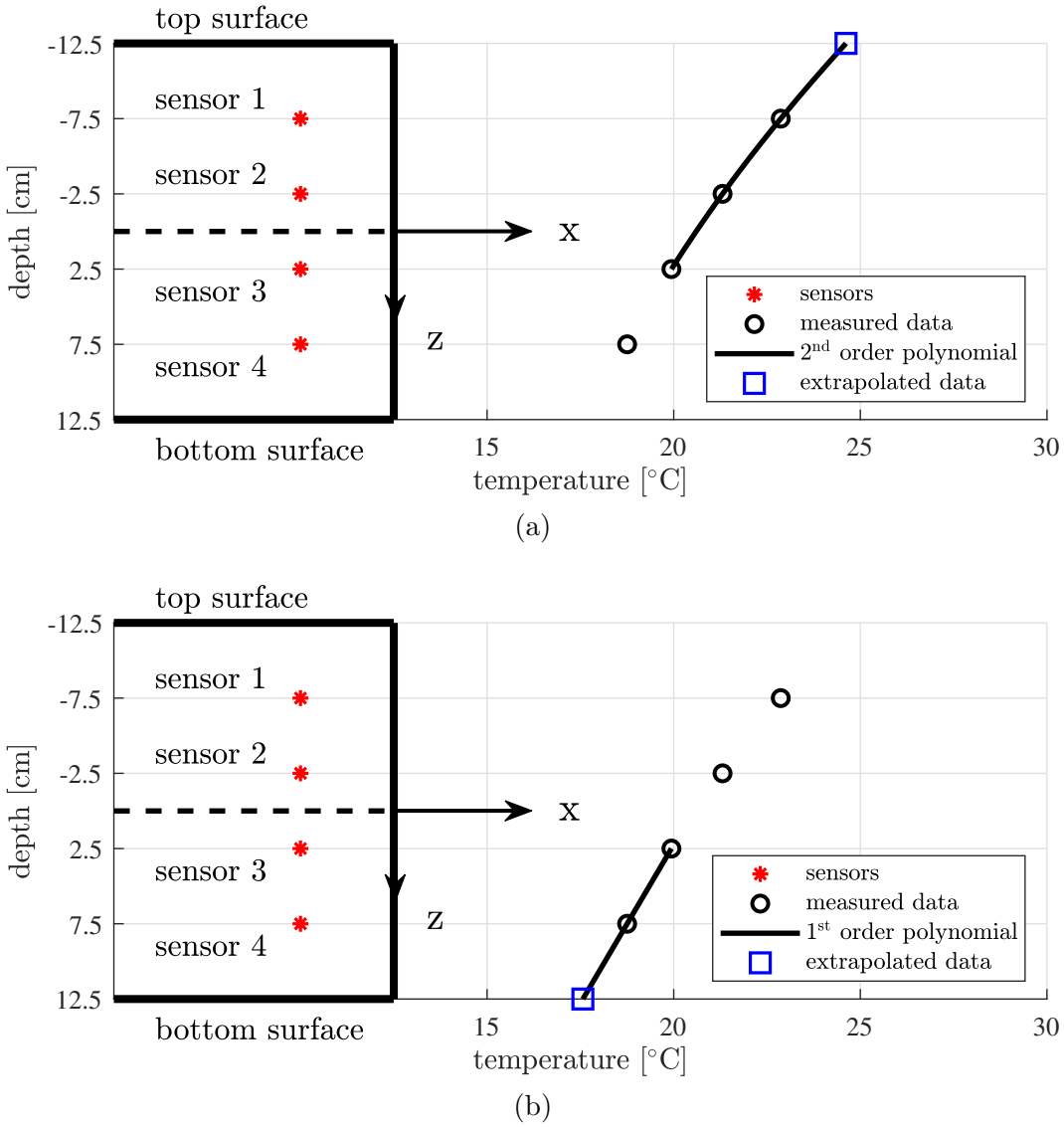

Fig. 3.7: Reconstruction of the temperature (a) at the top surface by means of quadratic extrapolation of the readings of the three topmost temperature sensors, and (b) at the bottom surface by means of linear extrapolation of the readings of the two bottommost temperature sensors.

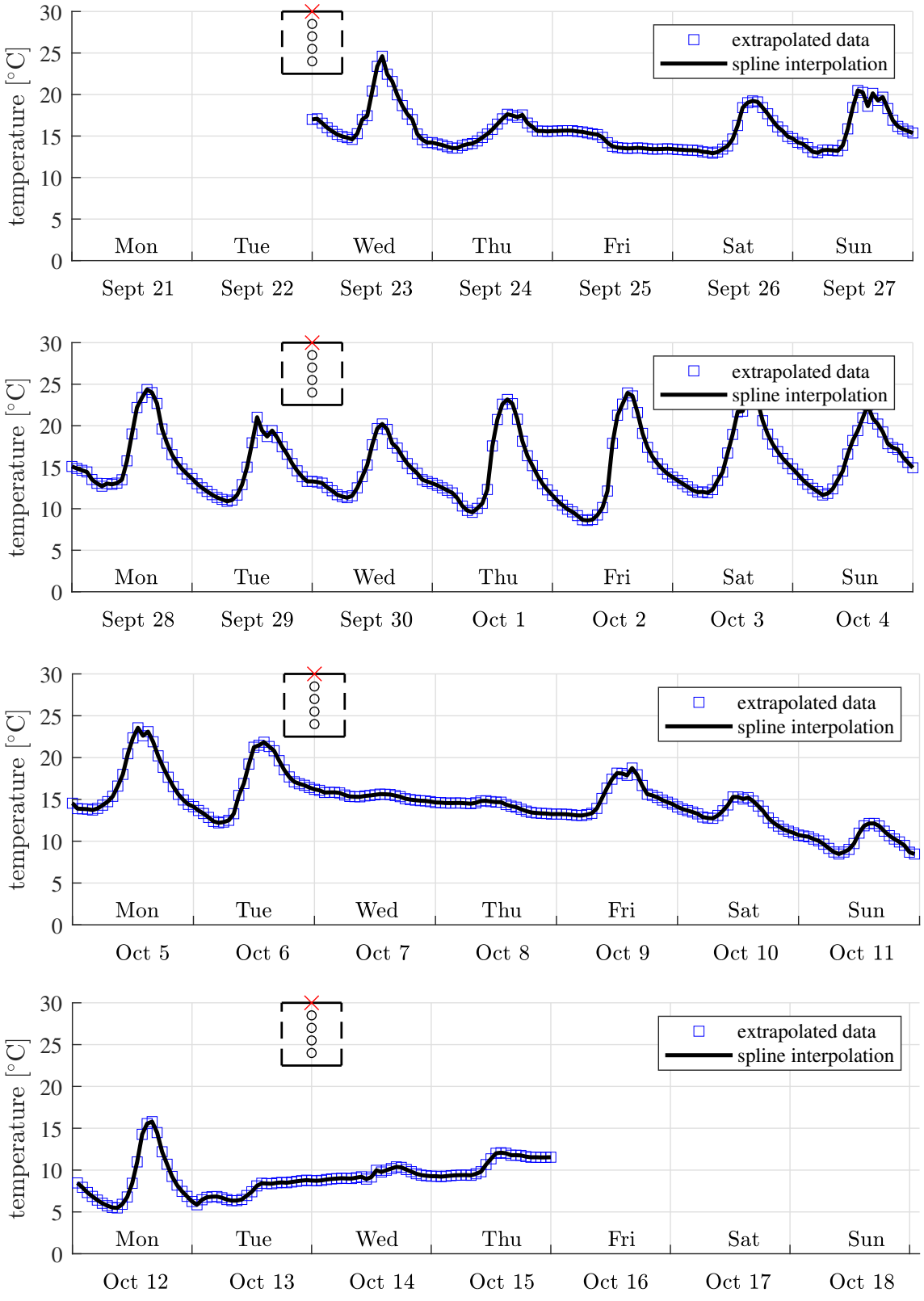

Fig. 3.8: Reconstructed temperature evolution at the top surface, see also Fig. 3.7 (a).

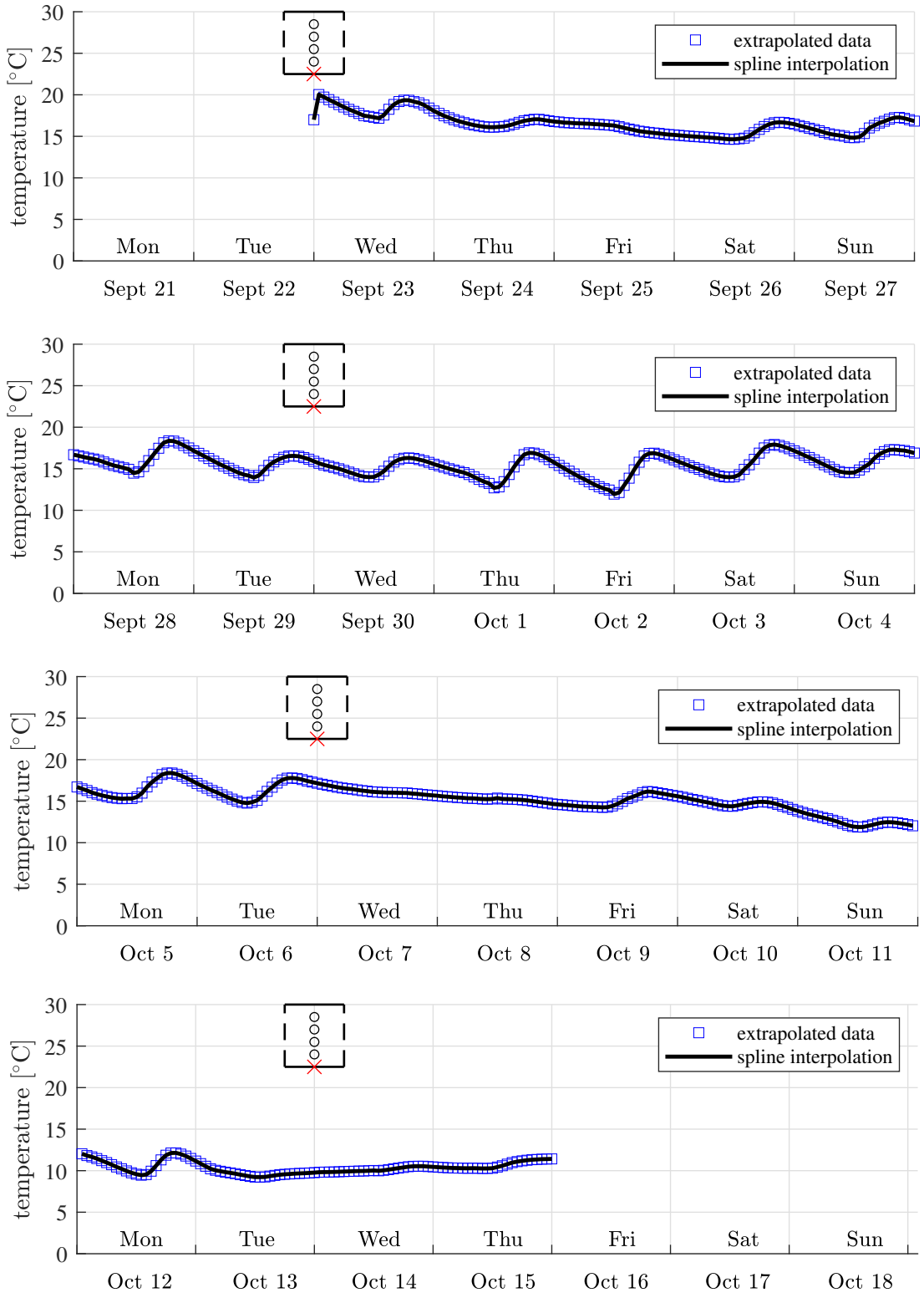

Fig. 3.9: Reconstructed temperature evolution at the bottom surface, see also Fig. 3.7 (b).

3.3 Transient heat conduction in thickness direction

The temperature evolutions at the top and bottom surfaces, $T^{top}(t)$ and $T^{bot}(t)$, see the continuous graphs in Figs. 3.8 and 3.9, are approximated in a stepwise fashion, with one temperature step every 30 minutes, see Figs. 3.10 and 3.11. This results in

$$N_i = 1104 \tag{3.2}$$

temperature steps. Their values are computed based on Eqs. (2.9) and (2.10), with the reference temperature reading as

$$T_{ref} = 17°\mathrm{C}\,. \tag{3.3}$$

Temperature distributions are computed according to Eq. (2.11). Therein, the infinite sums are truncated after the first five summands. This was found in the context of a corresponding sensitivity analysis as the optimal trade-off between approximation reliability and computational efficiency. The truncated version of Eq. (2.11) is evaluated for h according to Eq. (3.1) and the temperature steps illustrated in Figs. 3.10 and 3.11. The numerical value of the thermal diffusivity of concrete, a, is optimized such as to reproduce the temperature measurements in a best-possible fashion. This yields

$$a = 1.5 \times 10^{-6}\,\mathrm{m}^2/\mathrm{s}\,. \tag{3.4}$$

The plausibility of this result is checked as follows. The thermal conductivity k is equal to the product of the thermal diffusivity a, the mass density ρ, and the heat capacity c, i.e. $k = a\,\rho\,c$. Evaluating this expression based on Eq. (3.4) and the standard values

$$\rho = 2400\,\mathrm{kg}/\mathrm{m}^3\,, \tag{3.5}$$

see [14], and $c = 900\,\mathrm{J}/(\mathrm{kg\,K})$, see [22], yields $k = 3.24\,\mathrm{W}/(\mathrm{m\,K})$. This result is within the range of values reported in the literature $k \in [\,2.24\,,\,3.85\,]\,\mathrm{W}/(\mathrm{m\,K})$, see [2]. Thus, the check of plausibility of a according to Eq. (3.4) is accomplished successfully.

The computed temperature distributions reproduce the corresponding measurements in a satisfactory fashion, see e.g. Fig. 3.12. Based on these results, the following conclusions are drawn:

- The quadratic and linear extrapolations of temperature to the upper and lower surfaces of the plate, respectively, have delivered reliable surface temperature evolutions.
- The discretization of continuous temperature histories at the upper and lower surfaces of the plate by means of piecewise constant temperatures, with temperature steps once every 30 minutes, is accurate enough in order to obtain meaningful results.
- The assumption of an isothermal initial state of the plate, see Eqs. (2.4) and (3.3), is well suited for obtaining conclusive results, because already six hours after the start of the

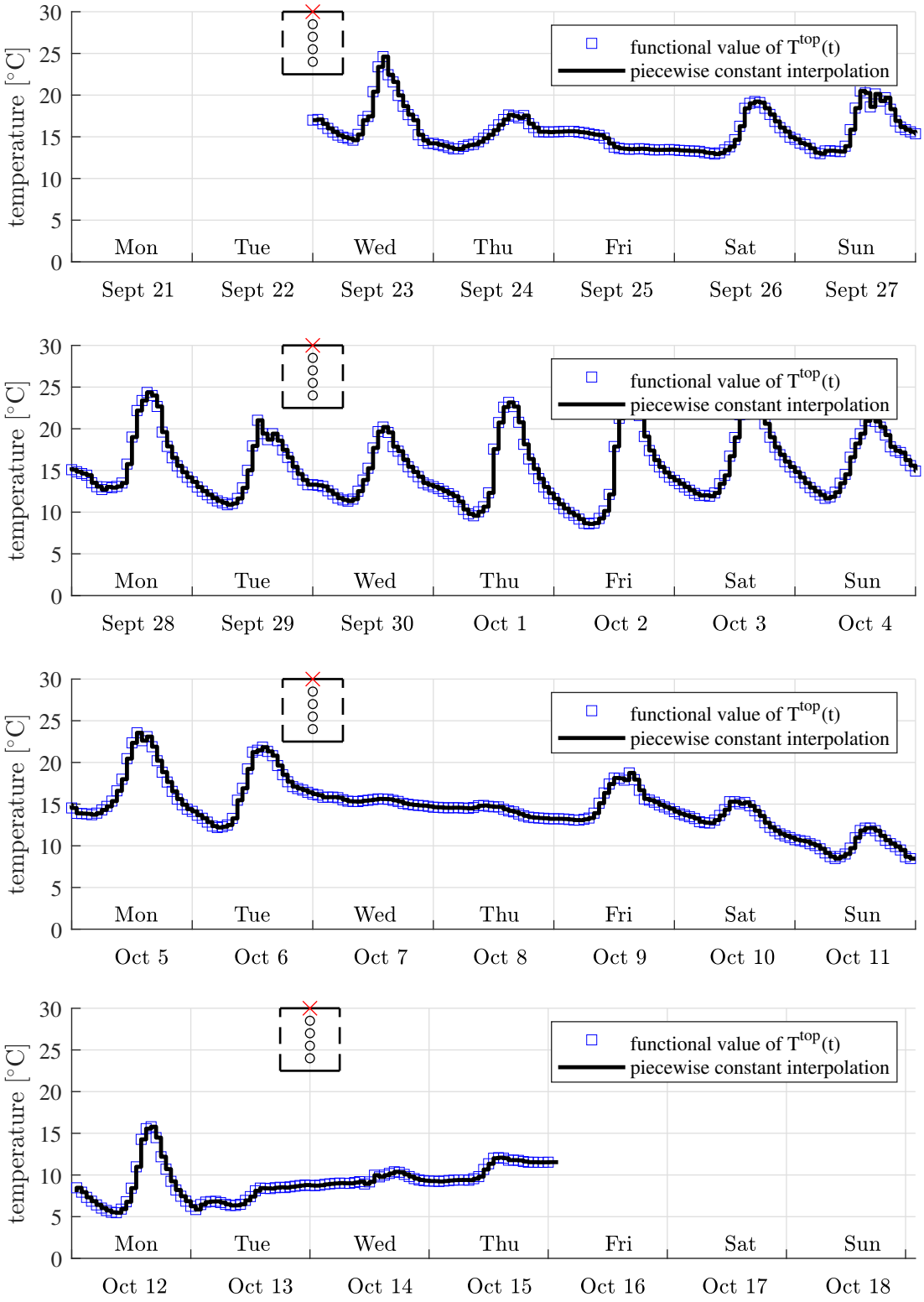

Fig. 3.10: Boundary conditions for the thermal analysis: stepwise approximation of the temperature evolution illustrated in Fig. 3.8, prescribed at the top surface of the plate.

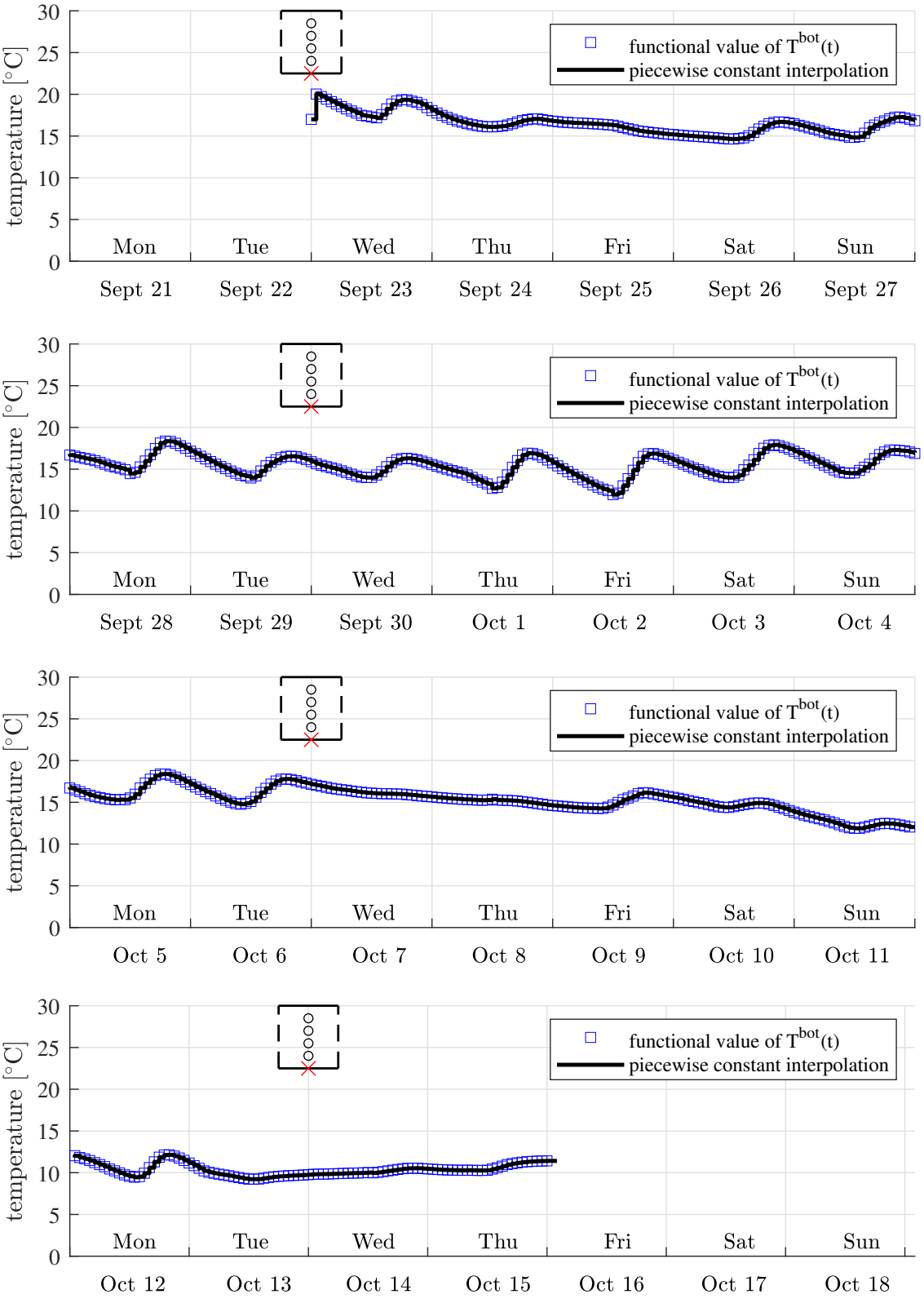

Fig. 3.11: Boundary conditions for the thermal analysis: stepwise approximation of the temperature evolution illustrated in Fig. 3.9, prescribed at the bottom surface of the plate.

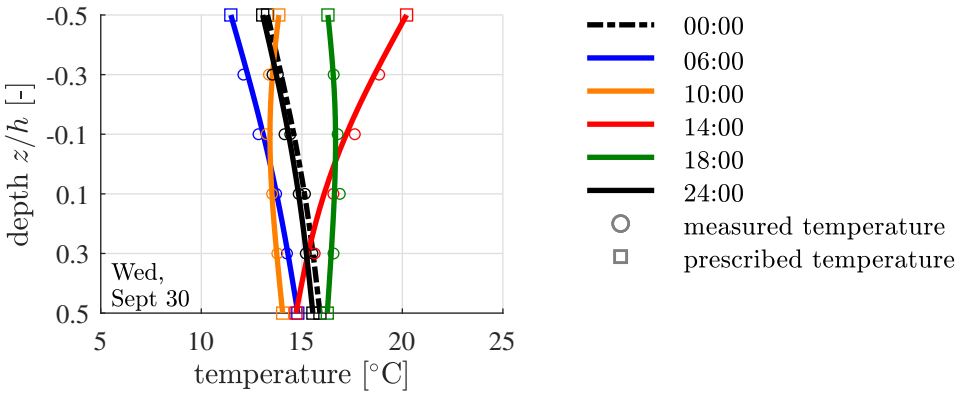

Fig. 3.12: Exemplary results of thermal analysis: computed distributions of temperature (see solid lines) and measured temperatures (see circles) referring to September 30, 2015, see Fig. A.1 of Appendix A for all results.

analysis, a satisfactory temperature distribution is obtained, see the temperature data referring to Wednesday, September 23, 6 a.m, in Fig. A.1, on page 50.

The largest deviations between the simulated and the measured temperatures occur during periods of rapid temperature changes. These residual deviations could be further reduced by introducing the thermal diffusivity as a function of the temperature and of the moisture content [16], rather than setting it equal to a constant. Such a refinement of the analysis, however, is beyond the scope of the present thesis.

3.4 Thermal eigenstrains

The total eigenstrains are computed according to Eq. (2.14), truncated after the first five summands and evaluated for h according to Eq. (3.1), a according to Eq. (3.4), and the temperature steps illustrated in Figs. 3.10 and 3.11. The coefficient of thermal expansion of concrete, α_T, is taken from [31] and reads as

$$\alpha_T = 1.153 \times 10^{-5}\,^{\circ}\mathrm{C}^{-1}\,. \tag{3.6}$$

The computed distributions of the total eigenstrains are qualitatively similar to the temperature distributions, compare Fig. 3.12 with Fig. 3.13(a).

The total eigenstrains are subdivided into three parts as illustrated in Fig. 2.4. The eigenstrains referring to eigenstretches ε^e_m of the plate are computed according to Eq. (2.43), truncated after the first five summands, see Fig. 3.13(b). The eigenstrains referring to eigencurvatures κ^e_m of the plate are computed according to Eq. (2.44), truncated after the first five summands, see Fig. 3.13(c). The eigenstrains referring to eigendistortions ε^e_{dist} of the generators of the plate are computed according to Eq. (2.42), see Fig. 3.13(d).

The eigenstretches result in in-plane expansion or contraction of the plate. This is unconstrained, because of the joints between neighboring plates. Thus, eigenstretches do not activate thermal

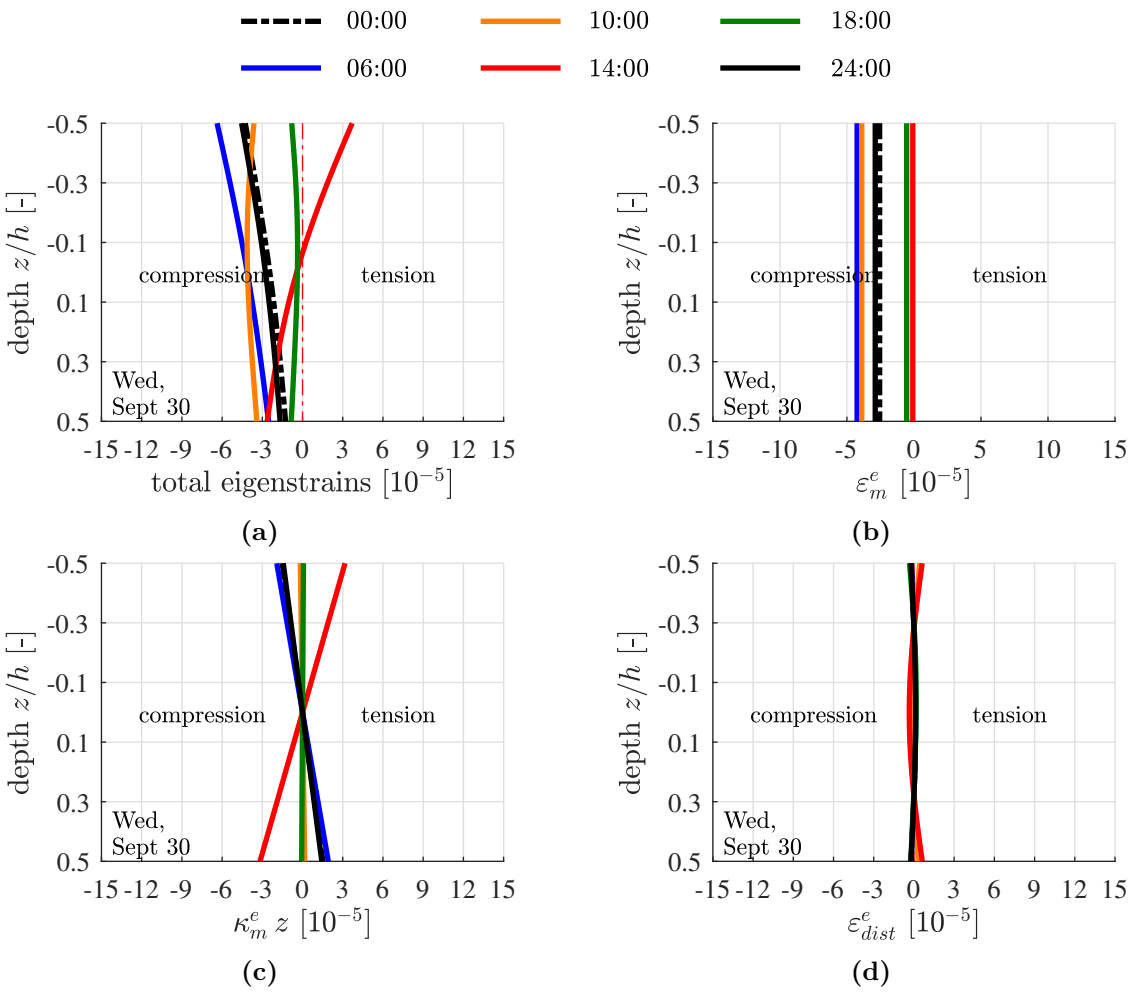

Fig. 3.13: Exemplary results of eigenstrain analysis: Decomposition of (a) the total eigenstrains into (b) eigenstrains referring to eigenstretches ε^e_m of the plate, (c) eigenstrains referring to eigencurvatures κ^e_m of the plate, and (d) eigenstrains referring to eigendistortions ε^e_{dist} of the generators of the plate; the shown results refer to September 30, 2015, see Fig. A.1 of Appendix A for all results.

stresses. Stresses resulting from the constrained eigencurvature of the plate and from the prevented eigendistortion of the generators of the plate are computed in the following two Sections.

3.5 Stresses resulting from constrained eigencurvatures of the plate

Thermal stresses resulting from constrained eigencurvatures are quantified by means of nonlinear Finite Element (FE) analysis. The length and the width of the simulated plate read as

$$l_x = 5.00\,\mathrm{m}\,, \tag{3.7}$$

$$l_y = 3.75\,\mathrm{m}\,. \tag{3.8}$$

The modulus of elasticity E and Poisson's ratio ν of concrete are taken from [31]:

$$E = 31.76\,\text{GPa}\,, \tag{3.9}$$

$$\nu = 0.203\,. \tag{3.10}$$

The plate rests on an elastic Winkler foundation [30, 33]. The modulus of subgrade reaction, K, is set equal to a typical value and reads as

$$K = 100\,\text{MPa/m}\,. \tag{3.11}$$

The plate is subjected to an eigencurvature and dead load. The latter represents a uniform vertical force per area. It is equal to the product of the mass density ρ, see Eq. (3.5), the gravitational acceleration $g = 9.81\,\text{m/s}^2$, and the thickness of the plate, h, see Eq. (3.1):

$$p = \rho\, g\, h = 5.89\,\text{kN/m}^2\,. \tag{3.12}$$

As for the numerical simulations, the midplane of the plate is discretized by means of $100 \times 75 = 7500$ quadratic Finite Elements with side length amounting to 5 cm, resulting in a mesh with 7676 nodes, see Fig. 3.14. The simulations are carried out with elements of type "Kirchhoff bending theory" available in commercial software RFEM [7].

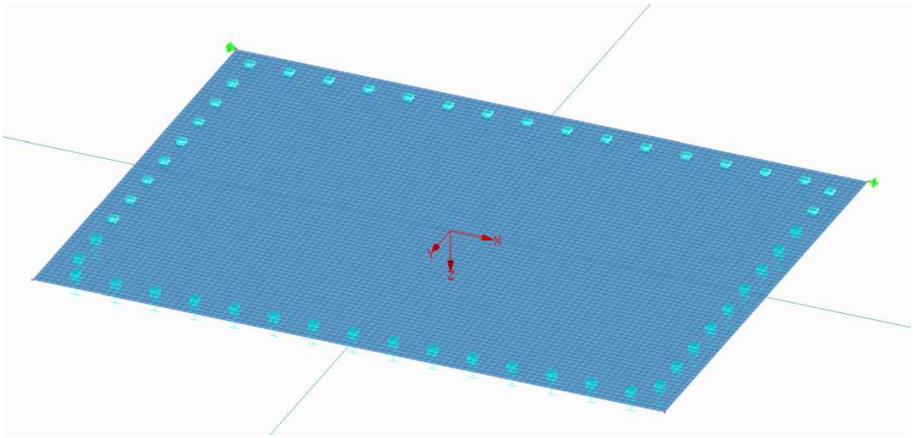

Fig. 3.14: Discretized of the midplane of the plate by means of $100 \times 75 = 7500$ quadratic Finite Elements of type "Kirchhoff plate theory".

The problem at hand is a nonlinear contact problem. Provided that the plate is pressed into the Winkler foundation, compressive normal stresses are activated in the interface between the plate and the elastic Winkler foundation. The absolute values of the activated stresses are equal to the deflections times the modulus of subgrade reaction. Provided that the plate lifts off from the Winkler foundation, no stresses are transmitted between the plate and the Winkler foundation. The region in which the plate lifts off from the subgrade is a priori unknown. The used software RFEM provides a built-in solver for the iterative solution of the described contact problem.

Ten nonlinear FE simulations are carried out. In each one of them, a spatially uniform eigencurvature is prescribed. From simulation to simulation, it is increased from zero in steps of $+1 \times 10^{-4}\,\mathrm{m}^{-1}$ to $+5 \times 10^{-4}\,\mathrm{m}^{-1}$, and from zero in steps of $-1 \times 10^{-4}\,\mathrm{m}^{-1}$ to $-5 \times 10^{-4}\,\mathrm{m}^{-1}$. Positive eigencurvatures refer to temperature gradients in which the top is cooler than the bottom. This results in concave warping of the plate: the central region of the plate is pressed into the Winkler foundation, and the corner regions lift-off from it, see Fig. 3.15(a). Vice versa, negative

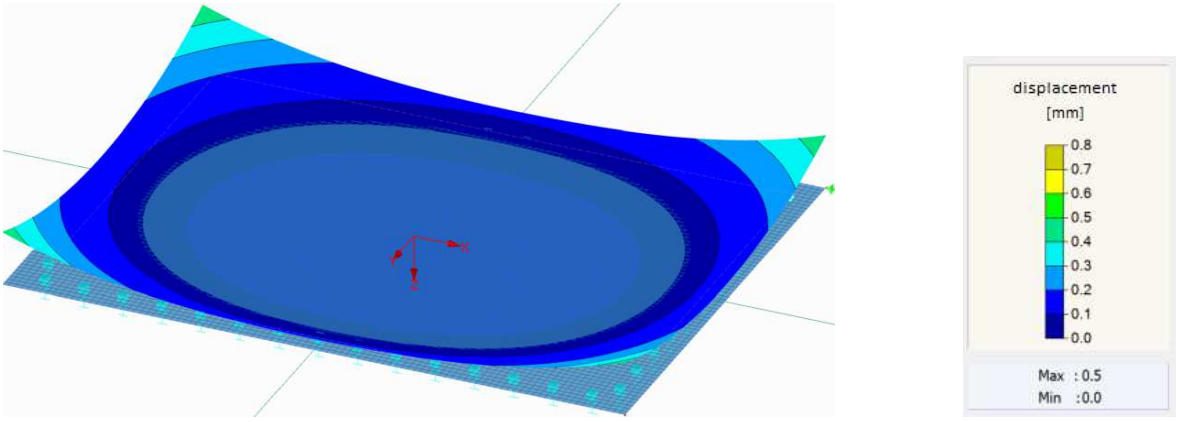

(a)

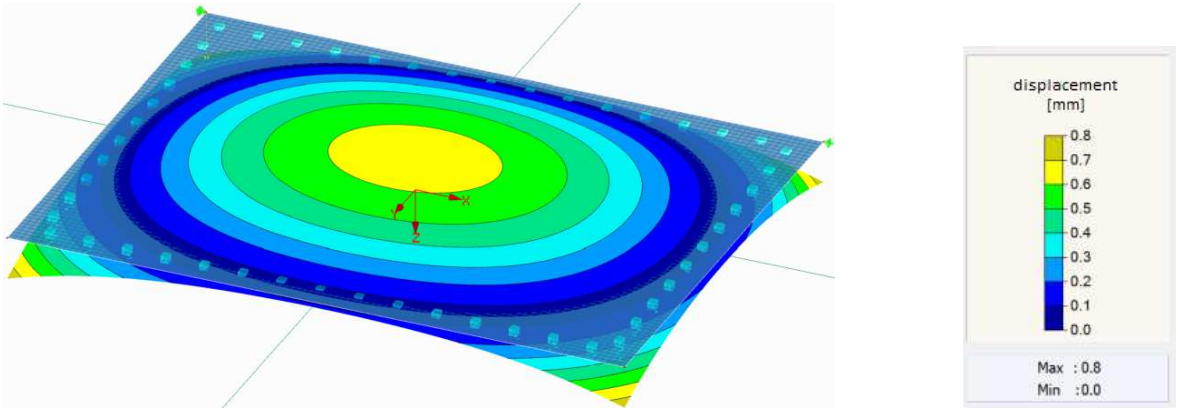

(b)

Fig. 3.15: Results from nonlinear FE analyses: deformed configurations of plates subjected to (a) positive eigencurvature $\kappa_m^e = +2.3 \times 10^{-4}\,\mathrm{m}^{-1}$, resulting in concave warping, and (b) negative eigencurvature $\kappa_m^e = -4.6 \times 10^{-4}\,\mathrm{m}^{-1}$, resulting in convex warping.

eigencurvatures refer to temperature gradients in which the top is warmer than the bottom. This results in convex warping of the plate: the central region of the plate lifts off from the Winkler foundation, the corner and edge regions are pressed into it, see Fig. 3.15(b).

Extreme values of the principal bending stress at the bottom of the plate are determined based on the results of the simulations, see the ordinate values of the circles in Fig. 3.16. Positive eigencurvatures result in compressive stresses at the bottom of the plate, see the right half of Fig. 3.16, and tensile stresses at the top. Vice versa, negative eigencurvatures result in tensile

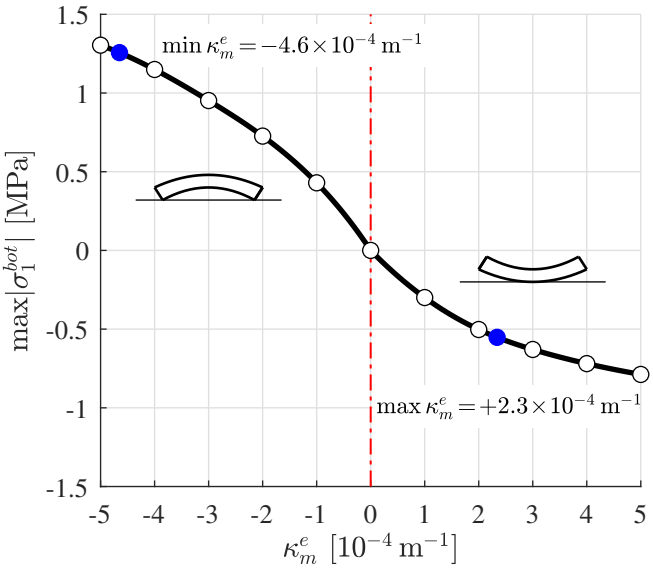

Fig. 3.16: Results from nonlinear FE analyses: extreme values of the principal bending stress at the bottom of the plate as a function of the prescribed eigencurvature; circles label numerical results, the solid lines are splines reproducing the simulation results and interpolating between them.

stresses at the bottom of the plate, see the left half of Fig. 3.16, and compressive stresses at the top.

Eigencurvatures of the temperature-monitored plate, computed according to Eq. (2.44), range from $-4.6\times10^{-4}\,\mathrm{m}^{-1}$ to $+2.3\times10^{-4}\,\mathrm{m}^{-1}$, see also the blue circles in Fig. 3.16. The corresponding extreme values of the principal bending stresses at the bottom of the plate range from +1260 kPa to −550 kPa. Because bending stresses are antisymmetric with respect to the midplane of the plate, the corresponding extreme values of the bending stresses at the top of the plate range from −1260 kPa to +550 kPa. The thermal stresses resulting from constrained eigencurvatures of the plate are illustrated exemplarily in Fig. 3.17.

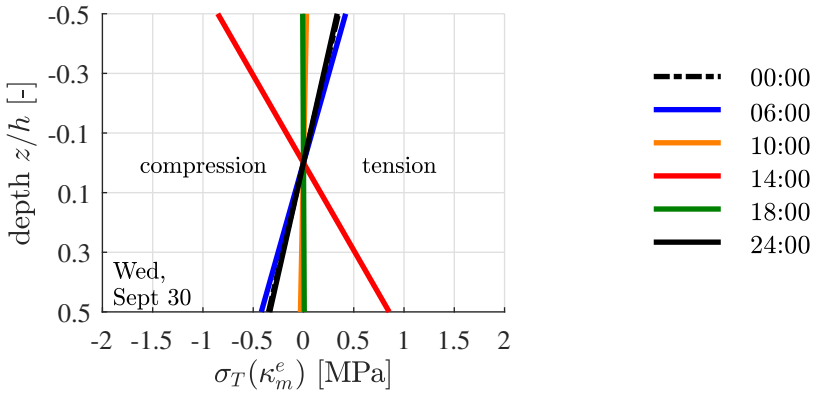

Fig. 3.17: Exemplary results of nonlinear FE analyses: thermal stresses resulting from the constrained eigencurvature of the plate; the shown results refer to September 30, 2015, see Fig. A.1 of Appendix A for all results.

The following results obtained for September 30, 2015 are noteworthy:

- In the early afternoon, the temperature at the top is larger than at the bottom, see Fig. 3.12. This results in convex warping of the plate which goes along with tensile stresses at the bottom and compressive stresses at the top of the plate, see the red graph in Fig. 3.17.
- During nighttime and early in the morning, the temperature at the top is smaller than at the bottom, see Fig. 3.12. This results in concave warping of the plate which goes along with compressive stresses at the bottom and tensile stresses at the top of the plate, see the black and blue graphs in Fig. 3.17.
- In the later morning and in the later afternoon, there are no significant temperature differences throughout the thickness of the plate, see Fig. 3.12. This refers to small eigencurvatures and, thus, to rather small maximum principal bending stresses, see the orange and green graphs in Fig. 3.17.

3.6 Stresses resulting from prevented eigendistortions of the generators of the plate

Thermal stresses resulting from eigendistortion of the generators of the plate are quantified based on Eq. (2.51), evaluated for elastic properties of the plate according to Eqs. (3.9) and (3.10), as well as for the total eigenstrains $\alpha_T \Delta T$, the eigenstretches ε^e_m, and the eigencurvatures κ^e_m computed before. The obtained stress distributions have a vanishing mean and a vanishing first moment, i.e. they do neither result in normal forces per unit length nor in bending moments per unit length, see e.g. Fig. 3.17.

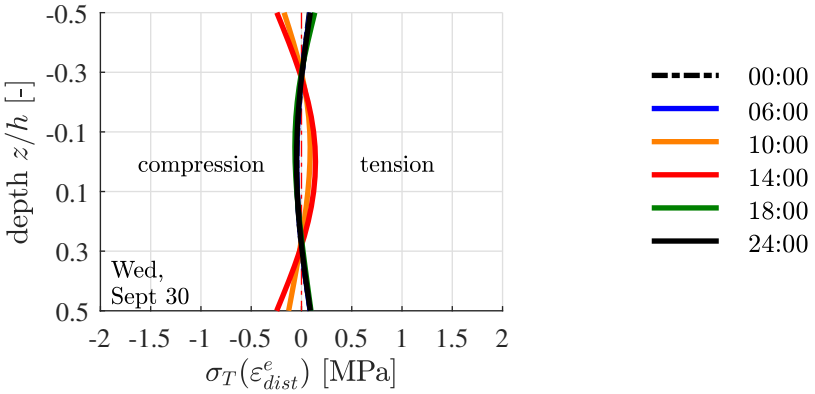

Fig. 3.18: Exemplary results of engineering thermo-mechanical analysis: thermal stresses resulting from the prevented eigendistortions of the generators of the plate; the shown results refer to September 30, 2015, see Fig. A.1 of Appendix A for all results.

The following results obtained for September 30, 2015 are noteworthy:

- Heating of the plate in the morning and during the early afternoon results in compressive stresses in the top and bottom regions of the plate, while tensile stresses are activated in the region around the midplane of the plate, see the orange and red graphs in Fig. 3.18.
- Cooling of the plate during the later afternoon and nighttime results in tensile stresses in the top and bottom regions of the plate, while compressive stresses are activated around the midplane of the plate, see the black, blue, and green graphs in Fig. 3.18.
- The thermal stresses are the larger, the larger the overall curvature of the temperature profile. Virtually linear temperature distributions result in almost vanishing nonlinear thermal stresses, see Fig. A.1, and compare, e.g., the distributions of the temperature and of the nonlinear thermal stresses on October 2 (see page 59) with those on October 7 (see page 64).

3.7 Total thermal stresses

The total thermal stresses are equal to the sum of the thermal stresses resulting from the constrained eigencurvatures of the plate (Section 3.5) and of the thermal stresses resulting from the prevented eigendistortions of the generators of the plate (Section 3.6):

$$\sigma_T \quad = \quad \sigma_T(\kappa_m^e) + \sigma_T(\varepsilon_{dist}^e)\,, \tag{3.13}$$

see e.g. Fig. 3.19(d). Extreme stress distributions are typically obtained in the early afternoon and in the early morning. During these two periods of the day, the two contributions to the total thermal stresses amplify each other at the top of the plate, and they diminish each other at the bottom of the plate, see also Table 3.1. This phenomenon is discussed in more detail in the following two paragraphs, based on the results obtained for September 30, 2015, see Fig. 3.19.

Tab. 3.1: Signs of both contributions to the total thermal stresses, typically obtained in the early afternoon and in the early morning.

	constrained eigencurvatures		**prevented eigendistortions**	
	early afternoon	early morning	early afternoon	early morning
Top	compression	tension	compression	tension
Midplane	–	–	tension	compression
Bottom	tension	compression	compression	tension

In the early afternoon, the top of the plate is warmer than its bottom, see the red graph in Fig. 3.19(a). This results in convex warping of the plate which goes along with compressive stresses at the top of the plate and tensile stresses at the bottom, see the red graph in Fig. 3.19(b). Prevented eigendistortions of the generators of the plate result in compressive stresses at the top and bottom of the plate, while tensile stresses are activated around its midplane, see the red graph in Fig. 3.19(c). Thus, the two thermal stress contributions are compressive (= mutually

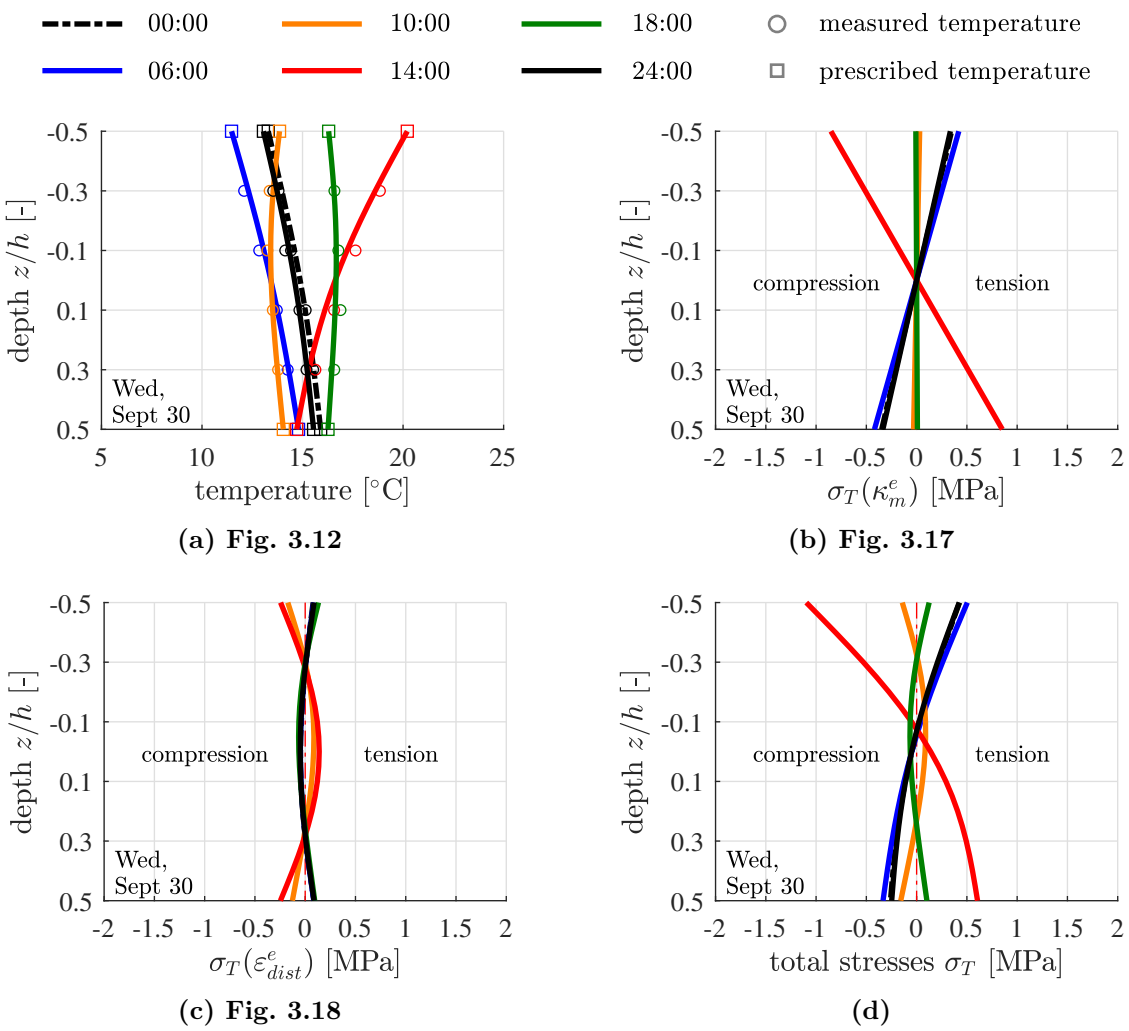

(a) Fig. 3.12 **(b) Fig. 3.17**

(c) Fig. 3.18 **(d)**

Fig. 3.19: Exemplary results of engineering thermo-mechanical analysis: (a) temperature distributions, (b) thermal stresses resulting from constrained eigencurvatures of the plate, (c) thermal stresses resulting from the prevented eigendistortions of the generators of the plate, and (d) total thermal stresses; the shown results refer to September 30, 2015, see Fig. A.1 of Appendix A for all results.

amplifying) at the top of the plate, while tensile stresses from the first contribution counteract compressive stresses from the second contribution at the bottom, see the red graph in Fig. 3.19(d).

In the early morning, the top of the plate is cooler than its bottom, see the blue graph in Fig. 3.19(a). This results in concave warping of the plate which goes along with tensile stresses at the top of the plate and compressive stresses at the bottom, see the blue graph in Fig. 3.19(b). Prevented eigendistortions of the generators of the plate result in tensile stresses at the top and bottom of the plate, while compressive stresses are activated around the midplane of the plate, see the blue graph in Fig. 3.19(c). Thus, the two contributions to the total thermal stresses are tensile (= mutually amplifying) at the top of the plate, while compressive stresses from the first contribution counteract tensile stresses from the second contribution at the bottom of the plate, see the blue graph in Fig. 3.19(d).

Chapter 4

Discussion of results obtained for the entire monitoring period

4.1 Bounding envelopes of temperature and stress distributions

As for the discussion of the results obtained for the entire monitoring period from September 23 to October 15, 2015, envelopes of temperature and stress distributions are discussed, see Fig. 4.1. These envelopes are boundaries which are reached at least once during the monitoring period, but not exceeded, e.g. the temperature at the top of the plate was always larger than or equal to 5.5°C and always smaller than or equal to 24.6°C, see Fig. 4.1(a). The following discussion is focused on tensile stresses, because they are essential for the design of concrete pavements, see e.g. [23].

By analogy to the results obtained for September 30, see Fig. 3.19, the two stress contributions are mutually amplifying at the top of the plate, but their extreme values do not occur simultaneously. The largest tensile stress from the constrained eigencurvatures of the plate amounts to +0.55 MPa, see Fig. 4.1(b). The largest tensile stress from the prevented eigendistortions of the generators of the plate amounts to +0.30 MPa, see Fig. 4.1(c). The largest total stress is slightly smaller than the sum of the two extreme values and amounts to +0.74 MPa, see Fig. 4.1(c).

The two stress contributions diminish each other at the bottom of the plate. The largest tensile stress from the constrained eigencurvatures of the plate amounts to +1.26 MPa, see Fig. 4.1(b), the largest total stress to +0.89 MPa.

4.2 Daytime heating is typically faster than nighttime cooling

As regards the total stresses at the top of the plate, the absolute value of the largest compressive stress is larger than the largest tensile stress, i.e. $|-1.84\,\text{MPa}| > +0.74\,\text{MPa}$, see Fig. 4.1(b). At the bottom of the plate, in turn, the absolute value of the largest compressive stress is quite similar to the largest tensile stress: $|-0.84\,\text{MPa}| \approx +0.89\,\text{MPa}$. This is a consequence of the fact that daytime heating of the plate occurs faster than nighttime cooling.

Fast daytime heating results in significant temperature differences between the top and the bottom of the plate and in significant nonlinearities of the temperature distributions across the thickness of the plate.

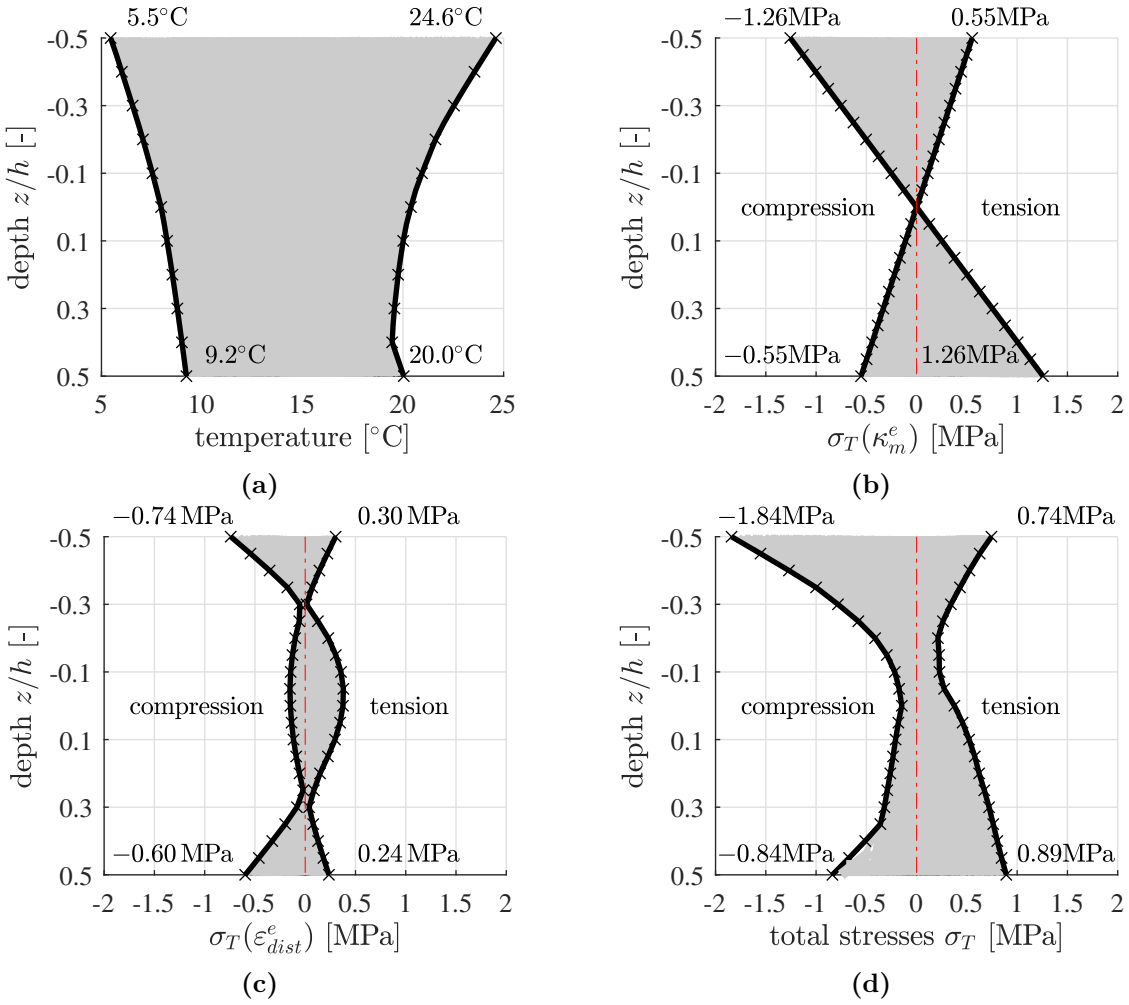

Fig. 4.1: Overview over results obtained for the entire monitoring period from September 23 to October 15, 2015: envelopes of temperature and stress distributions

- The significant temperature gradients result in significant convex warping of the plate. This manifests itself in significant compressive stresses at the top and significant tensile stresses at the bottom of the plate.
- The significant nonlinearities of the temperature distributions, in turn, result in significant compressive stresses at the top and the bottom of the plate.

Mutual amplification of thermal stress contributions at the top results in daily extreme values of compressive stresses at the top. Mutual attenuation of thermal stress contributions at the bottom results in smaller daily extreme values of tensile stresses at the bottom.

Slow nighttime cooling results in less significant temperature differences between the top and the bottom of the plate and in less significant nonlinearities of the temperature distributions across the thickness of the plate.

- The less significant temperature gradients result in less significant concave warping of the plate. This manifests itself in less significant tensile stresses at the top and less significant compressive stresses at the bottom of the plate.
- The less significant nonlinearities of the temperature distributions, in turn, result in less significant tensile stresses at the top and the bottom of the plate.

Mutual amplification of thermal stress contributions at the top results in daily extreme values of tensile stresses at the top. Mutual attenuation of thermal stress contributions at the bottom results in daily extreme values of compressive stresses at the bottom.

4.3 Tensile stresses and implications for the design of concrete pavements

The tensile strength of concrete typically ranges from 2 MPa to 3 MPa. The largest tensile stress at the bottom of the plate occurred during the early afternoon and amounted to 0.89 MPa, see Fig. 4.1(d). Thus, the degree of utilization, which is equal to the stress-to-strength ratio, ranged from 29.7 % to 44.5 %. This is particularly relevant for plates subjected to traffic loads associated with wheels running predominantly in the early afternoon over the center of the plate, such that the service loads also result in tensile stresses at the bottom of the plate, further increasing the degree of utilization. The largest tensile stress at the top of the plate occurred during the early morning amounted to 0.74 MPa, Fig. 4.1(d). Thus, the degree of utilization ranged from 24.7 % to 37.0 %. This is particularly relevant for plates subjected to traffic load associated with wheels running predominantly during the early morning over the corners and along the edges of the plate, such that the service loads also result in tensile stresses at the top of the plate, further increasing the degree of utilization.

Determination of the 23 daily maxima of the *total* tensile thermal stresses occurring at the top and at the bottom of the plate, and quantification of their mean values and standard deviations yields

$$\text{top:} \qquad \max \sigma_T \;=\; +0.50 \pm 0.17\,\text{MPa}\,, \tag{4.1}$$

$$\text{bottom:} \qquad \max \sigma_T \;=\; +0.42 \pm 0.37\,\text{MPa}\,. \tag{4.2}$$

Similar determination of the 23 daily maxima of the tensile thermal stresses *resulting from the constrained eigencurvatures of the plate*, and quantification of their mean values and standard deviations yields

$$\text{top:} \qquad \max \sigma_T(\kappa_m^e) \;=\; +0.39 \pm 0.13\,\text{MPa}\,, \tag{4.3}$$

$$\text{bottom:} \qquad \max \sigma_T(\kappa_m^e) \;=\; +0.61 \pm 0.49\,\text{MPa}\,. \tag{4.4}$$

Eqs. (4.1)–(4.4) underline that disregarding the thermal stresses resulting from the prevented eigendistortions of the generators of the plate relative to the thermal stresses resulting from the

constrained eigencurvatures of the plate results in an underestimation of the largest tensile stress at the top of the plate by 22 %, and in overestimation by 45 % at the bottom of the plate.

4.4 Sign changes of thermal stresses resulting from daily temperature fluctuations

Subsequent cycles of heating and cooling of the plate go along with changing mathematical signs of the two contributions to the total thermal stresses. The change of sign of stresses resulting from the prevented eigendistortions of the generators of the plate typically occurs *earlier* than the change of sign of stresses resulting from the constrained eigencurvatures of the plate. This can be illustrated e.g. based on the results obtained for October 2, 2015, see Fig. 4.2.

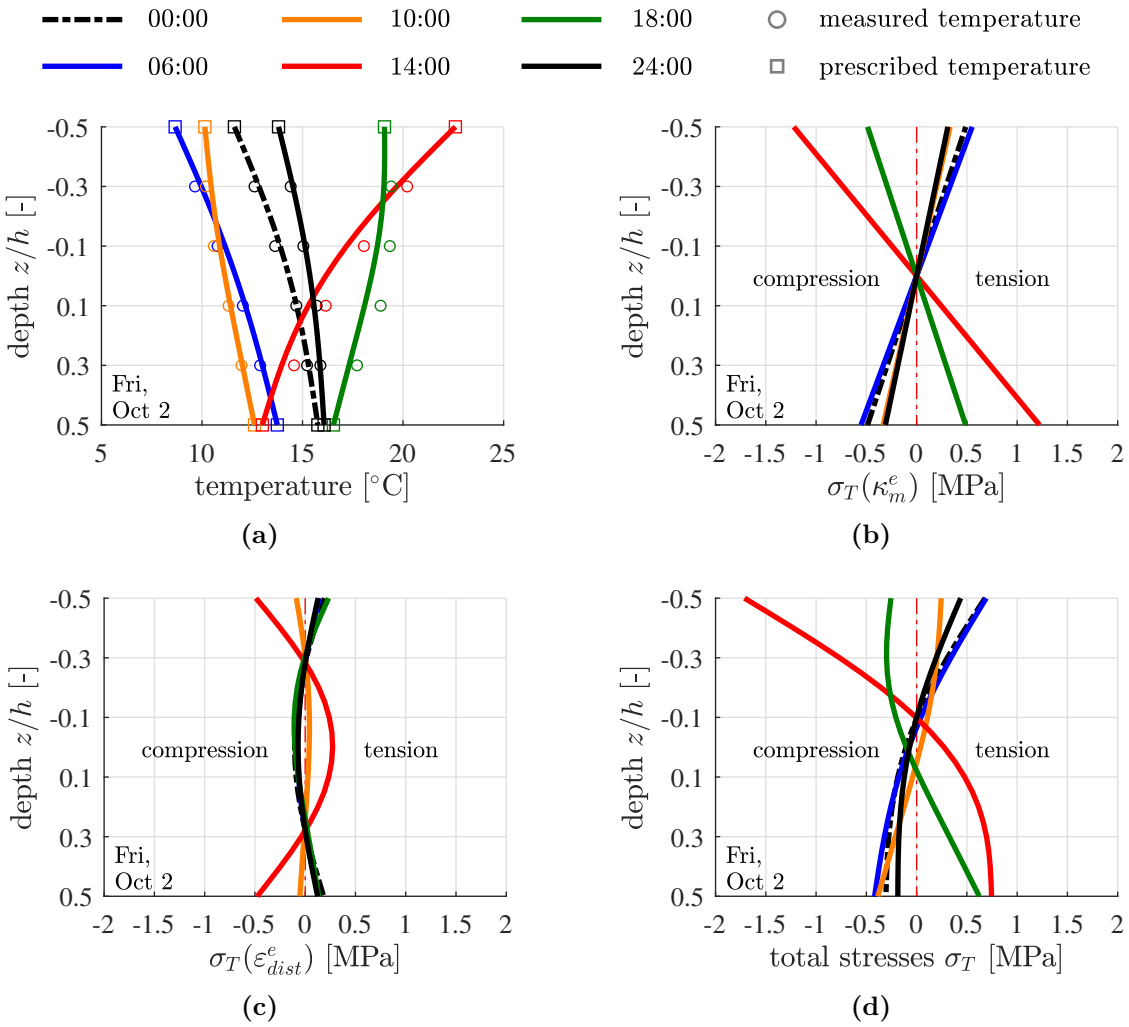

Fig. 4.2: Exemplary results of engineering thermo-mechanical analysis: (a) temperature distributions, (b) thermal stresses resulting from constrained eigencurvatures of the plate, (c) thermal stresses resulting from the prevented eigendistortions of the generators of the plate, and (d) total thermal stresses; the shown results refer to October 2, 2015.

At 6 o'clock in the morning, see the blue graphs in Figs. 4.2, the top of the plate was significantly cooler than the bottom of the plate. Heat was flowing upwards and the plate showed concave warping. At the top of the plate, mutual amplification of tensile stresses resulted in the largest tensile stress of the day, amounting to +0.69 MPa. Mutual attenuation of thermal stress contributions occurred at the bottom of the plate. Nonetheless, the largest compressive stress of the day was reached there, amounting to −0.42 MPa.

At 10 o'clock in the morning, see the orange graphs in Figs. 4.2, solar heating had increased the temperature of the top surface, but heat was still flowing upwards. Despite the initiated heating at the top, the plate showed still concave warping, resulting in tensile stresses at the top and compressive stresses at the bottom. The sign of the thermal stresses resulting from the prevented eigendistortions of the generators of the plate, in turn, had already changed, resulting in compressive stresses both at the top and bottom of the plate.

At 2 o'clock in the afternoon, see the red graphs in Figs. 4.2, the top of the plate was significantly warmer than the bottom of the plate. Heat was flowing downwards and the plate showed convex warping. At the top of the plate, mutual amplification of compressive stresses resulted in the largest compressive stress of the day, amounting to −1.71 MPa. Mutual attenuation of thermal stress contributions occurred at the bottom of the plate. Nonetheless, the largest tensile stress of the day was reached there, amounting to +0.75 MPa.

At 6 o'clock in the afternoon, see the green graphs in Figs. 4.2, the top surface had already started to cool down, but heat was still flowing downwards. Despite the initiated cooling at the top, the plate showed still convex warping, resulting in compressive stresses at the top and tensile stresses at the bottom. The sign of the thermal stresses resulting from the prevented eigendistortions of the generators of the plate, in turn, had already changed, resulting in tensile stresses both at the top and bottom of the plate.

At midnight, see the black solid graphs in Figs. 4.2, the top of the plate was significantly cooler than the bottom of the plate. Heat was flowing upwards and the plate showed concave warping. Mutual amplification of tensile stresses took place at the top of the plate, mutual attenuation at the bottom.

4.5 Limitations of the present study and future outlook

The limitations of the presented study provide motivation for future work:

- The analyzed monitoring period covered 23 days in autumn 2015. It is desirable, to extend it to several years. This will ensure that also extreme weather events are monitored. Hot summer days interrupted by sudden hail showers are known to represent a particular threat to the integrity of concrete pavements [31].

- The monitoring data were captured at one specific location in Lower Austria. It is desirable, to install and run such field testing sites at many other locations which are representative for the climatic conditions of other geographic regions.

- Thermal stresses resulting from constrained eigencurvatures of the plate were computed for one realistic value of the modulus of subgrade reaction, see Eq. (3.11). In the future, it is desirable to perform a sensitivity analysis based on a range of typical stiffnesses of the sub-construction.

It is well known that passenger cars are significantly less harmful to pavements that trucks, and the latter are again significantly less harmful than significantly overloaded heavy good vehicles. A similar situation exists with temperature loadings. Regular seasonal and daily temperature fluctuations are less harmful than rare extreme weather events such as extremely hot summer days interrupted by a sudden hail shower, compare the thermal stresses computed herein with the ones documented in [31]. In the context of a semi-probabilistic design approach, it will be interesting to quantify the probability of differently severe extreme weather events, and to design pavements in a way that they can withstand the extreme weather events expected during their service life without getting significantly damaged.

Chapter 5

Conclusions

In the present thesis, a thermo-mechanical analysis was described for a concrete plate which is part of highway "A2 – Süd Autobahn", near the junction *Bad Vöslau*, in Lower Austria, and for which temperature measurements are available for the period of time from September 23 to October 15, 2015. Two contributions to thermal stresses were quantified: the one from constrained eigencurvatures of the plate *and* the one from prevented eigendistortions of generators of the plate. From the obtained results, the following conclusions are drawn.

- Extreme values of daily thermal stresses are typically reached in the early morning and in the early afternoon.
- In the early morning, the top of the plate is cooler than the bottom of the plate. Thus, the plate exhibits concave warping. This goes along with tensile principal bending stresses at the top and compressive stresses at the bottom. The self-equilibrated stresses resulting from the prevented eigendistortions of the generators of the plate are tensile both at the bottom and at the top of the plate, as well as compressive in the region of the midplane of the plate.
- In the early afternoon, the top of the plate is warmer than the bottom of the plate. Thus, the plate exhibits convex warping. This goes along with compressive principal bending stresses at the top and tensile stresses at the bottom. The self-equilibrated stresses resulting from the prevented eigendistortions of the generators of the plate, are compressive both at the bottom and at the top of the plate, as well as tensile in the region of the midplane of the plate.
- Thus, both in the early morning and in the early afternoon, the two contributions to the total thermal stresses amplify each other at the top of the plate and diminish each other at the bottom of the plate.

Tensile thermal stresses are of great interest when it comes to the design of pavements:

- In the analyzed period of time, the daily maxima of the tensile stresses amount to $0.50 \pm 0.17\,\mathrm{MPa}$ at the top and to $0.42 \pm 0.37\,\mathrm{MPa}$ at the bottom of the plate.
- Following international guidelines for pavement design by disregarding thermal stresses resulting from prevented eigendistortions of the plate generators leads to daily maxima of

the tensile stresses amounting to $0.39 \pm 0.13\,\mathrm{MPa}$ at the top and to $0.61 \pm 0.49\,\mathrm{MPa}$ at the bottom of the plate.

- Thus, disregarding thermal stresses resulting from prevented eigendistortions of the plate generators leads to an underestimation of the expected values of the daily maxima of tensile stresses at the top of the plate by 22 % and to an overestimation of these expected values at the bottom of the plate by 45 %.

Tensile stresses also result from traffic loads. Tensile stresses are activated (i) at the bottom of the plate, if traffic loads are positioned in the middle of the plate, and (ii) at the top of the plate, if traffic loads are positioned in the vicinity of a corner or an edge. These stresses are standardly superimposed with tensile thermal stresses resulting from prevented eigencurvatures of the plate.

- If the largest total tensile stress is obtained at the top of the plate, the underestimation of the actual thermal stresses results in an unsafe design.
- If the largest total tensile stress is obtained at the bottom of the plate, the overestimation of the actual thermal stresses results in an overly conservative and, thus, uneconomic design.
- Thus, performing a few additional analytical calculations, such as presented in this study, is inexpensive and has the potential to lead to pavement designs that can be both safer and more economic.

These analytical calculations are organized as follows. The thermal eigenstrains are computed by multiplying temperature changes with the coefficient of thermal expansion of concrete: $\alpha_T \Delta T$. The eigenstretches of the plate are equal to the mean value of the eigenstrain distribution:

$$\varepsilon_m^e = \frac{1}{h} \int_{-\frac{h}{2}}^{+\frac{h}{2}} \alpha_T \Delta T \; \mathrm{d}z \,. \tag{2.32}$$

The eigencurvatures of the plate are equal to the first moment of the eigenstrain distribution:

$$\kappa_m^e = \frac{12}{h^3} \int_{-\frac{h}{2}}^{+\frac{h}{2}} \alpha_T \Delta T \, z \; \mathrm{d}z \,. \tag{2.39}$$

The thermal stresses resulting from prevented eigendistortions of the generators of the plate follow simply as

$$\sigma_T = -\frac{E}{1-\nu} \Big(\alpha_T \Delta T - \varepsilon_m^e - \kappa_m^e z \Big) \,. \tag{2.51}$$

These stresses are distributed nonlinearly across the thickness of the plate. They have a vanishing mean value, and a vanishing first moment.

Appendices

Appendix A

Summary of results: temperature, eigenstrain, and stress distributions

The following pages contain diagrams illustrating the results of the performed thermo-mechanical analysis. One page each is dedicated to one day of temperature measurements. The left column of figures refers to eigenstrains, the right column to the temperature evolution and to thermal stresses:

- total eigenstrains
- eigenstrains from eigenstretches
- eigenstrains from eigencurvatures
- eigenstrains from eigendistortions
- temperature evolution
- thermal stresses resulting from constrained eigencurvatures of the plate
- thermal stresses resulting from prevented eigendistortion of the plate
- total thermal stresses

Each one of these quantities is evaluated at six time instants of the day, at 0:00, 6:00, 10:00, 14:00, 18:00 and 24:00.

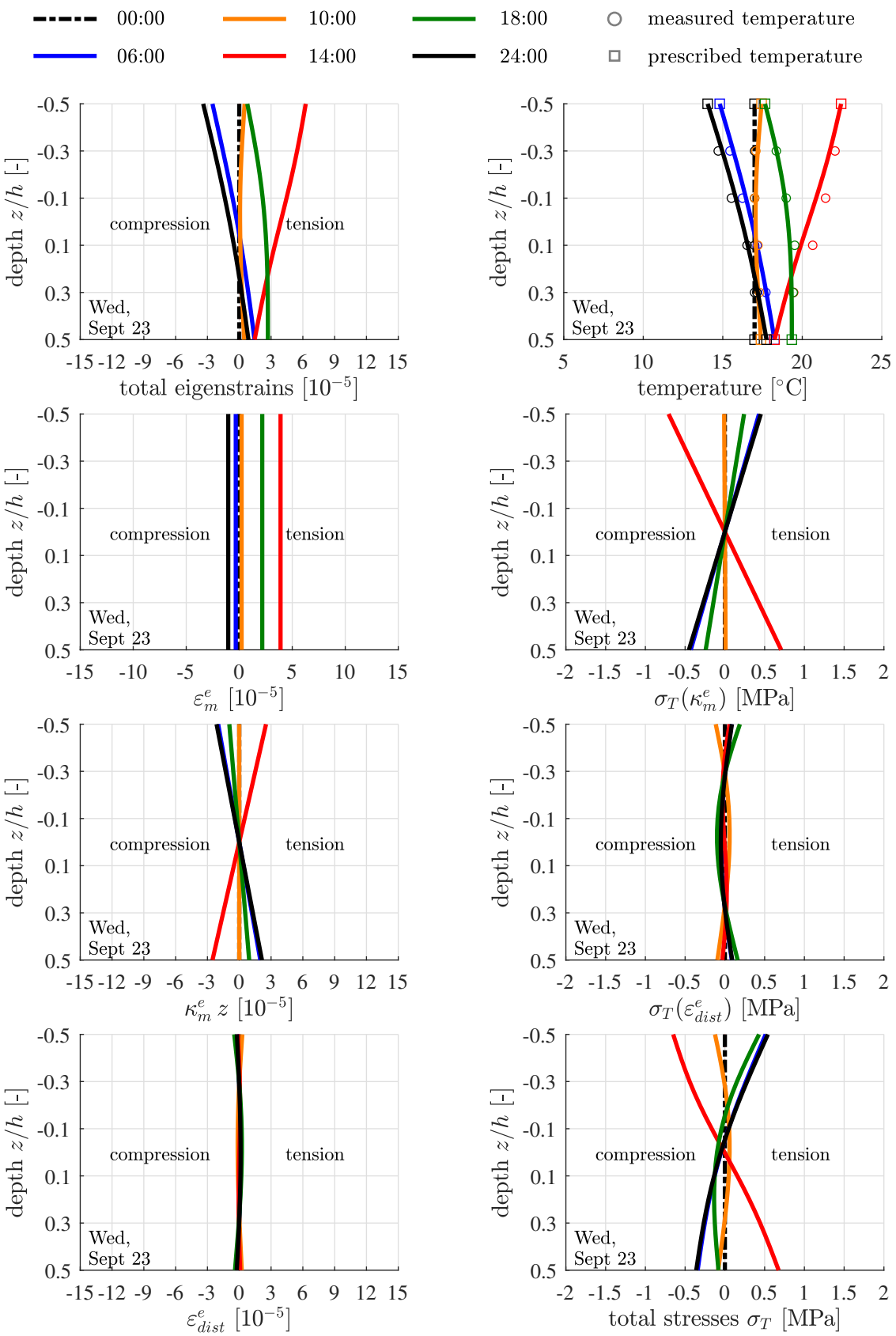

Fig. A.1: Results of the thermo-mechanical analysis regarding September 23; the figure is continued on the following pages.

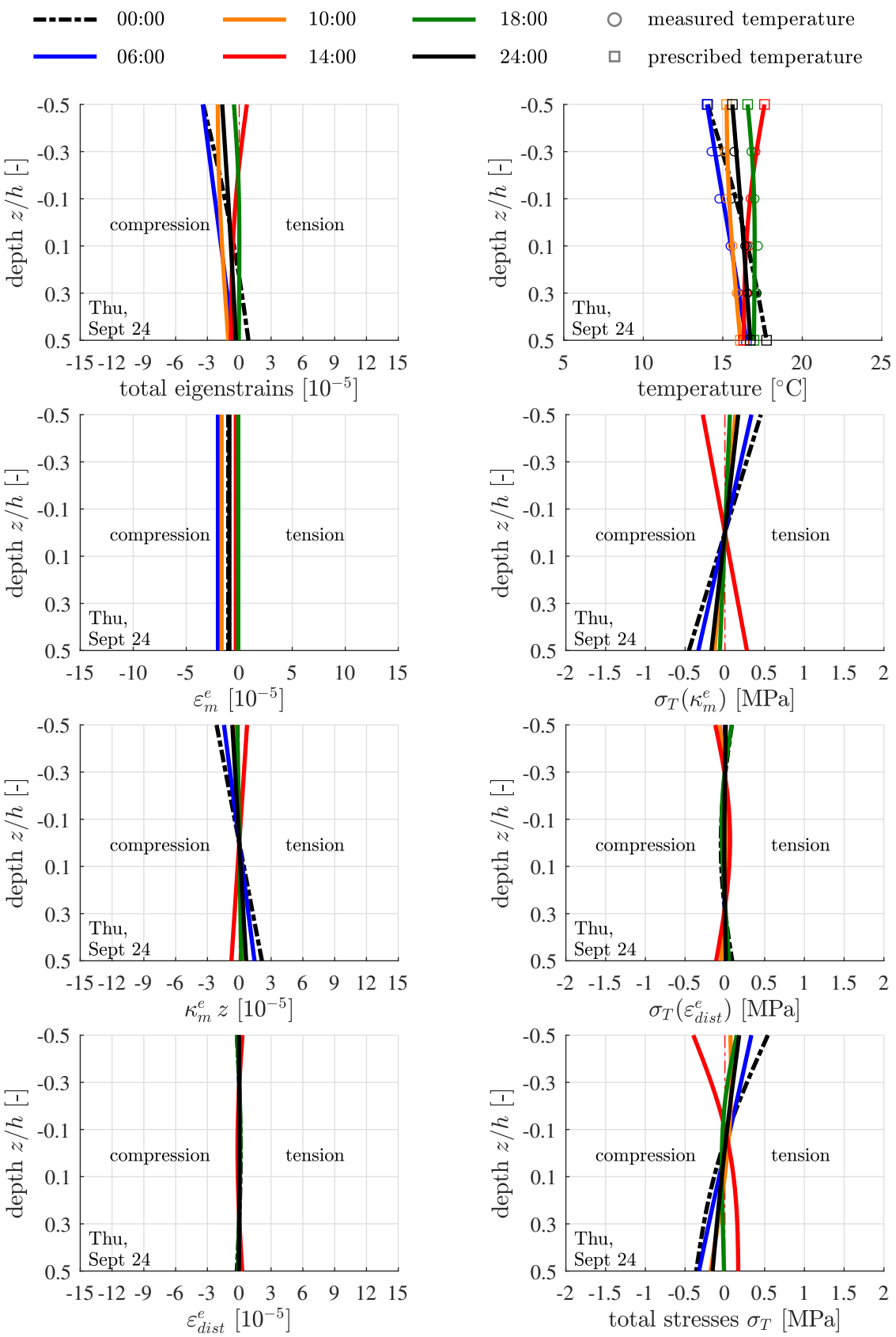

Fig. A.1 [cont'd]: Results of the thermo-mechanical analysis regarding September 24

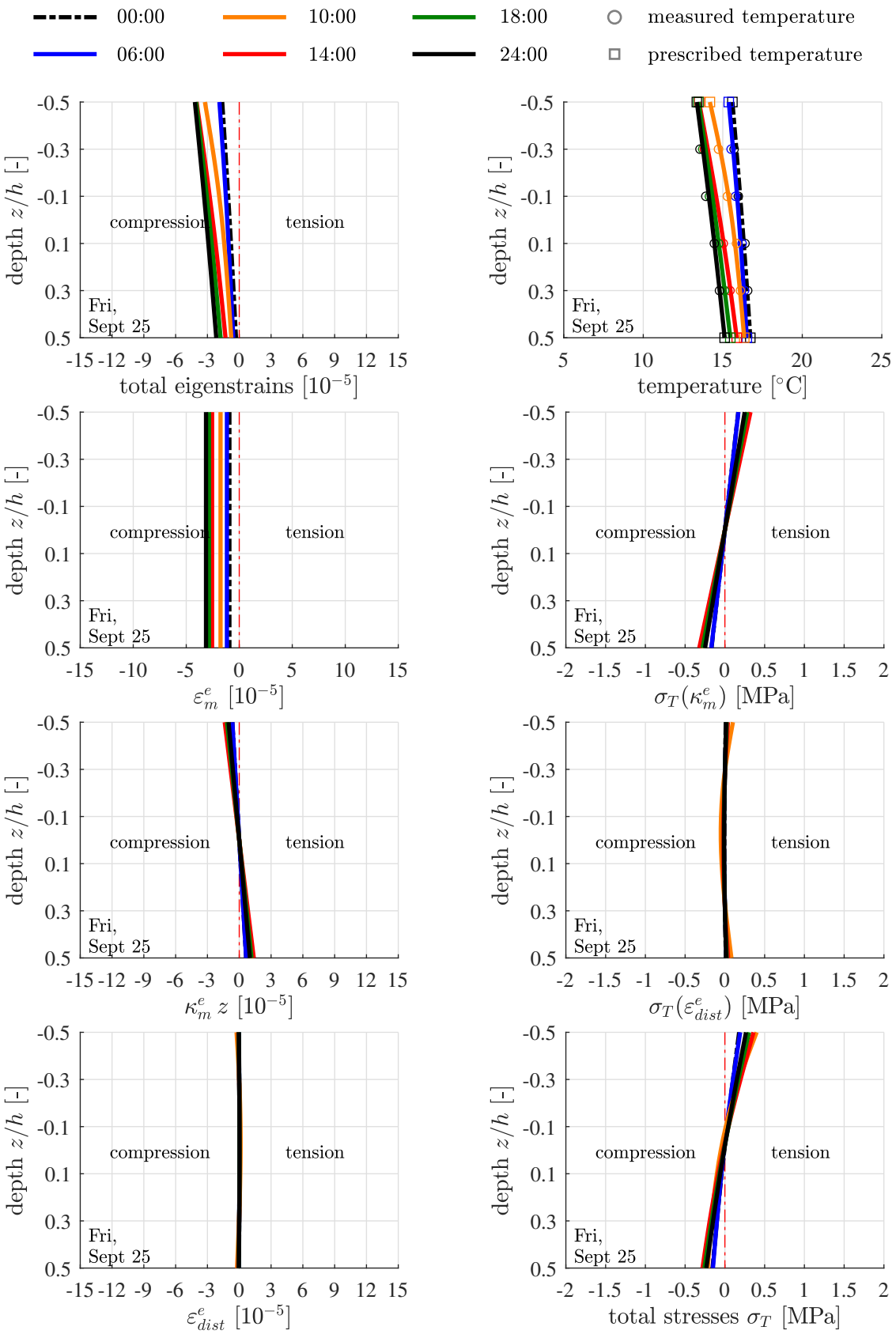

Fig. A.1 [cont'd]: Results of the thermo-mechanical analysis regarding September 25

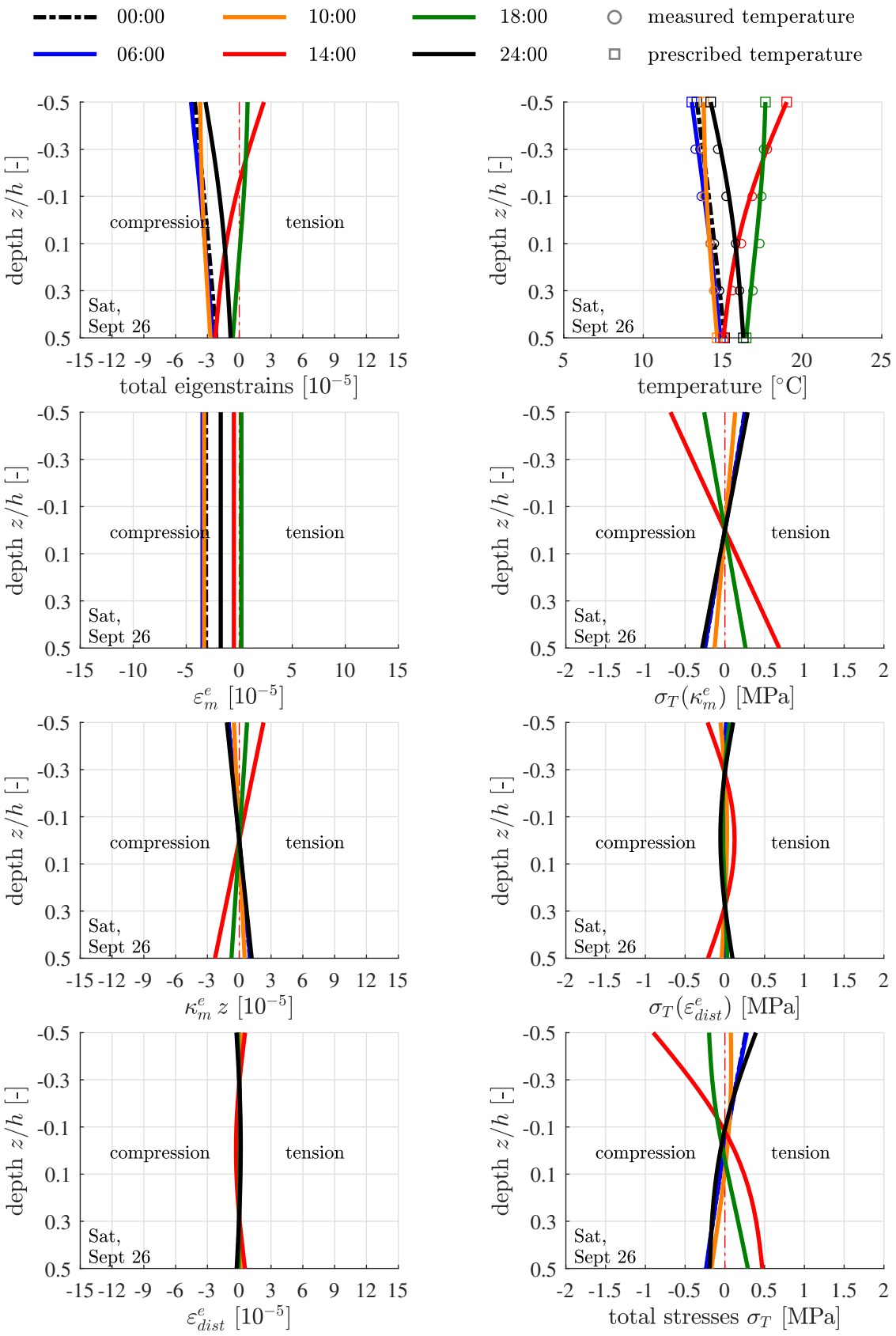

Fig. A.1 [cont'd]: Results of the thermo-mechanical analysis regarding September 26

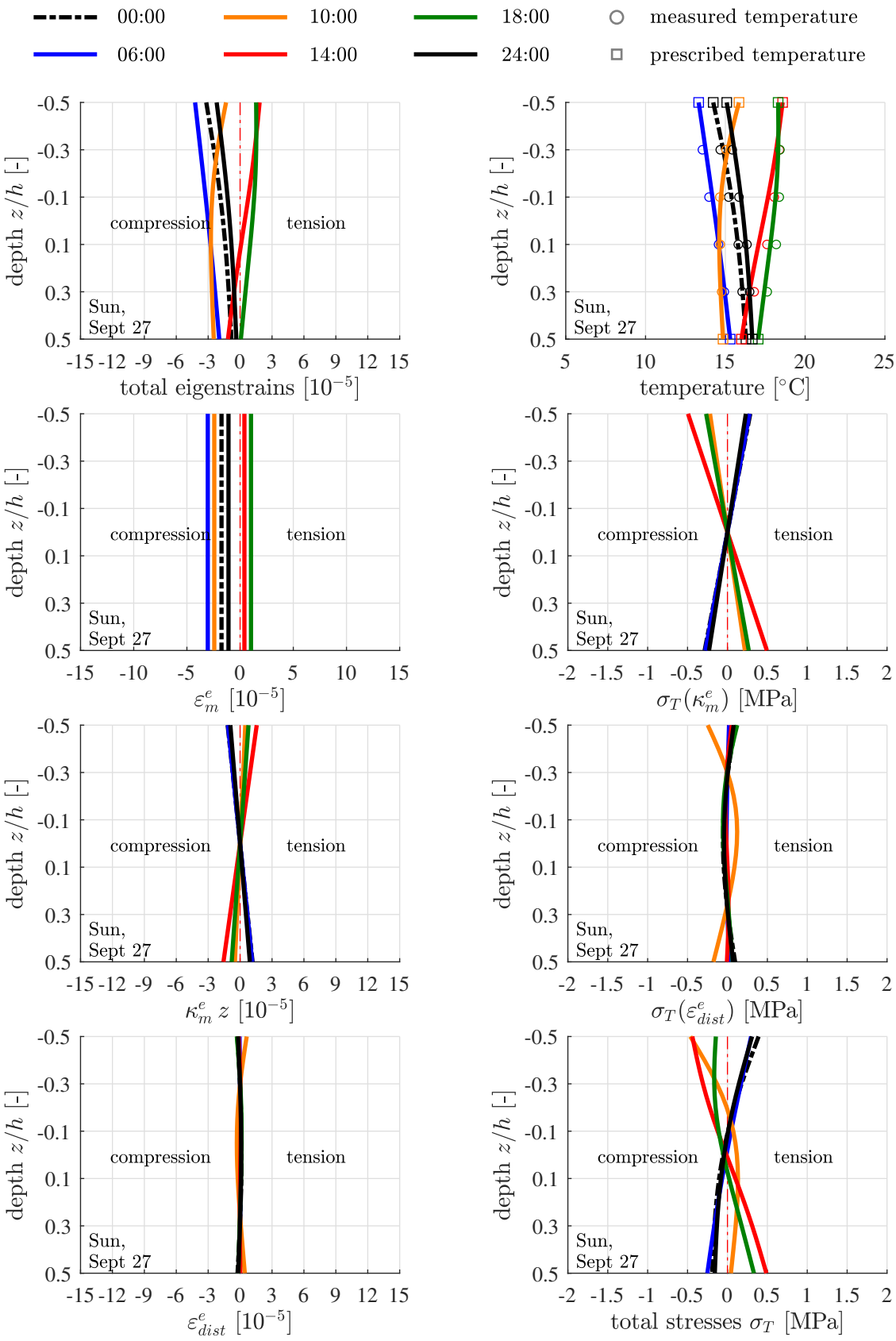

Fig. A.1 [cont'd]: Results of the thermo-mechanical analysis regarding September 27

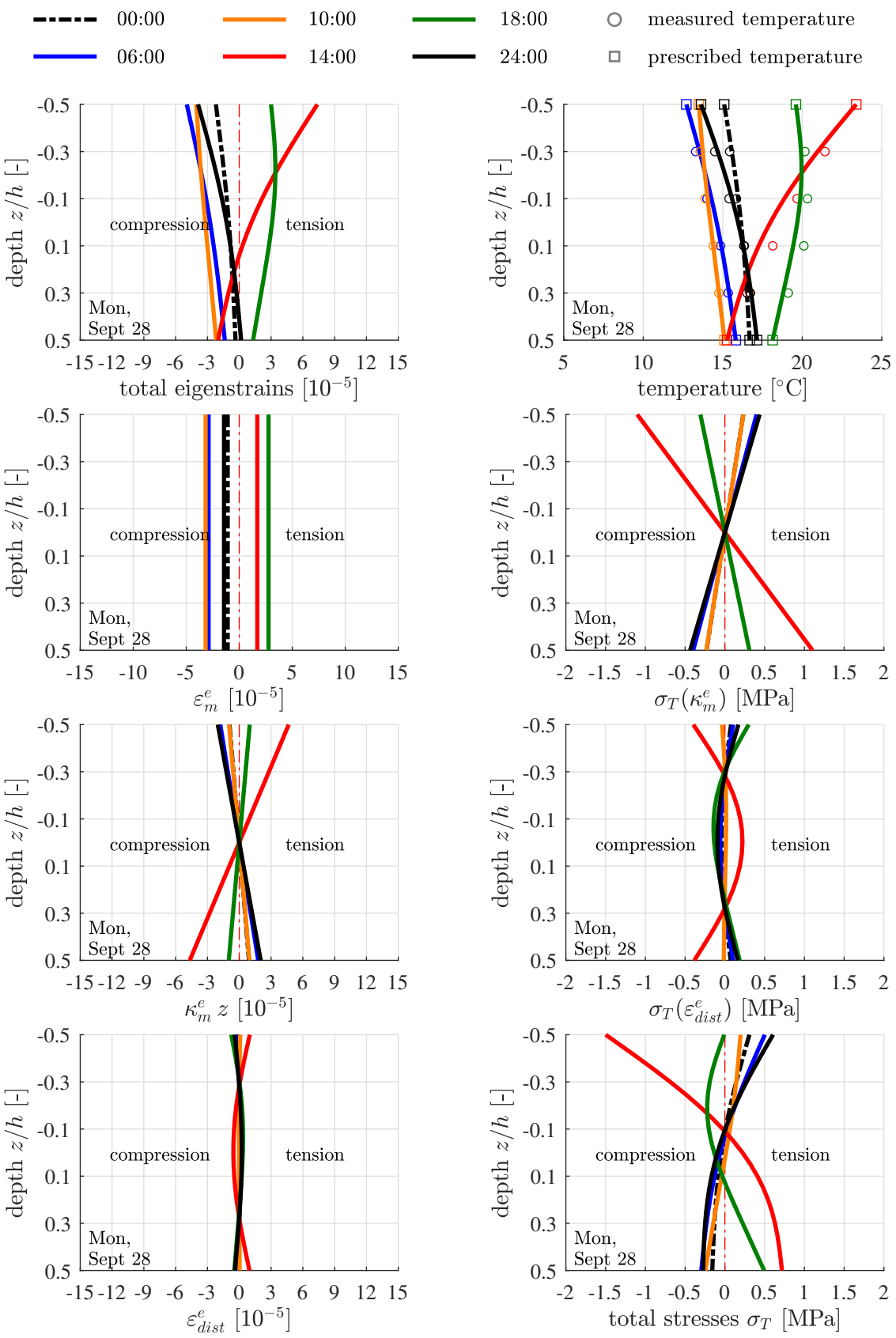

Fig. A.1 [cont'd]: Results of the thermo-mechanical analysis regarding September 28

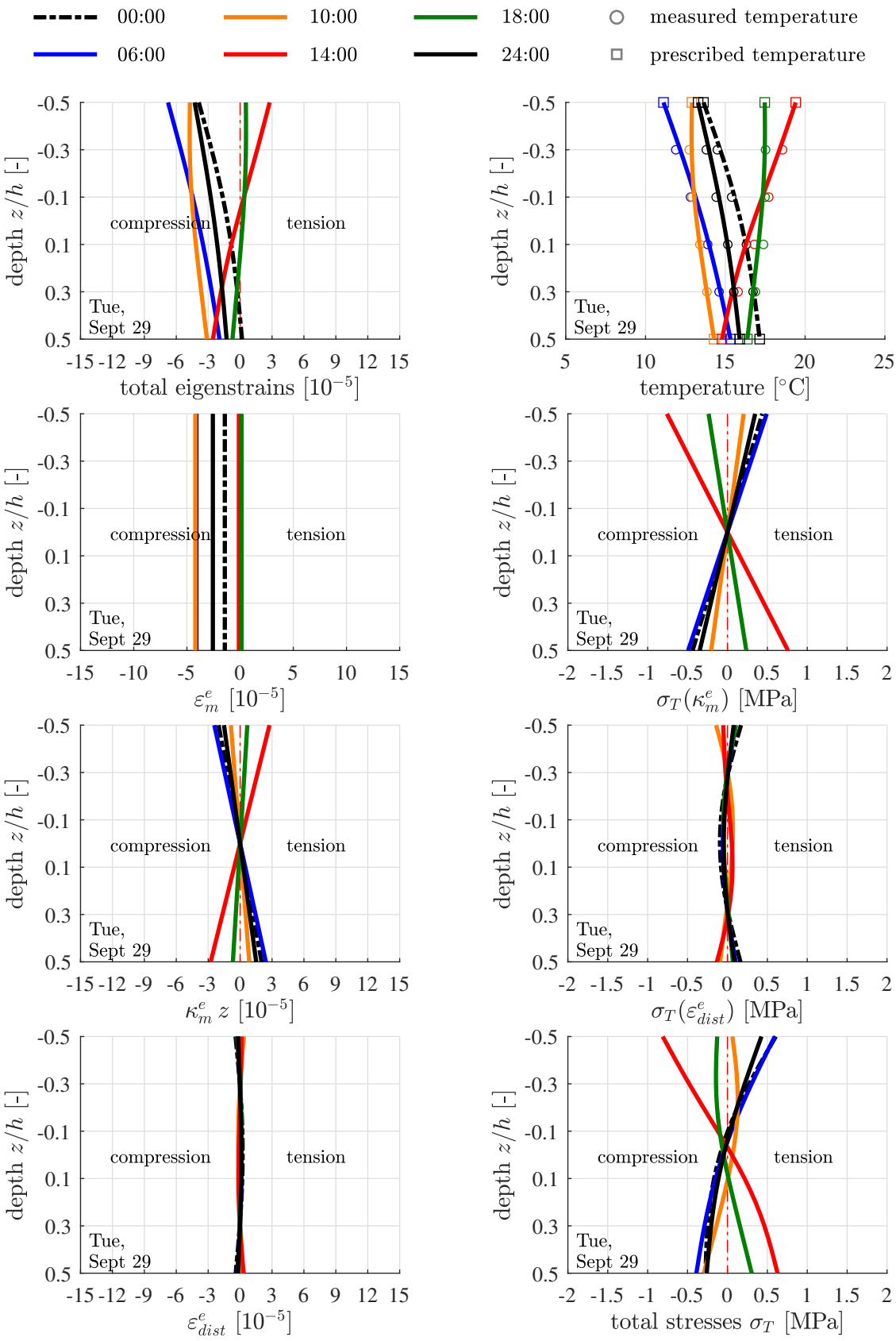

Fig. A.1 [cont'd]: Results of the thermo-mechanical analysis regarding September 29

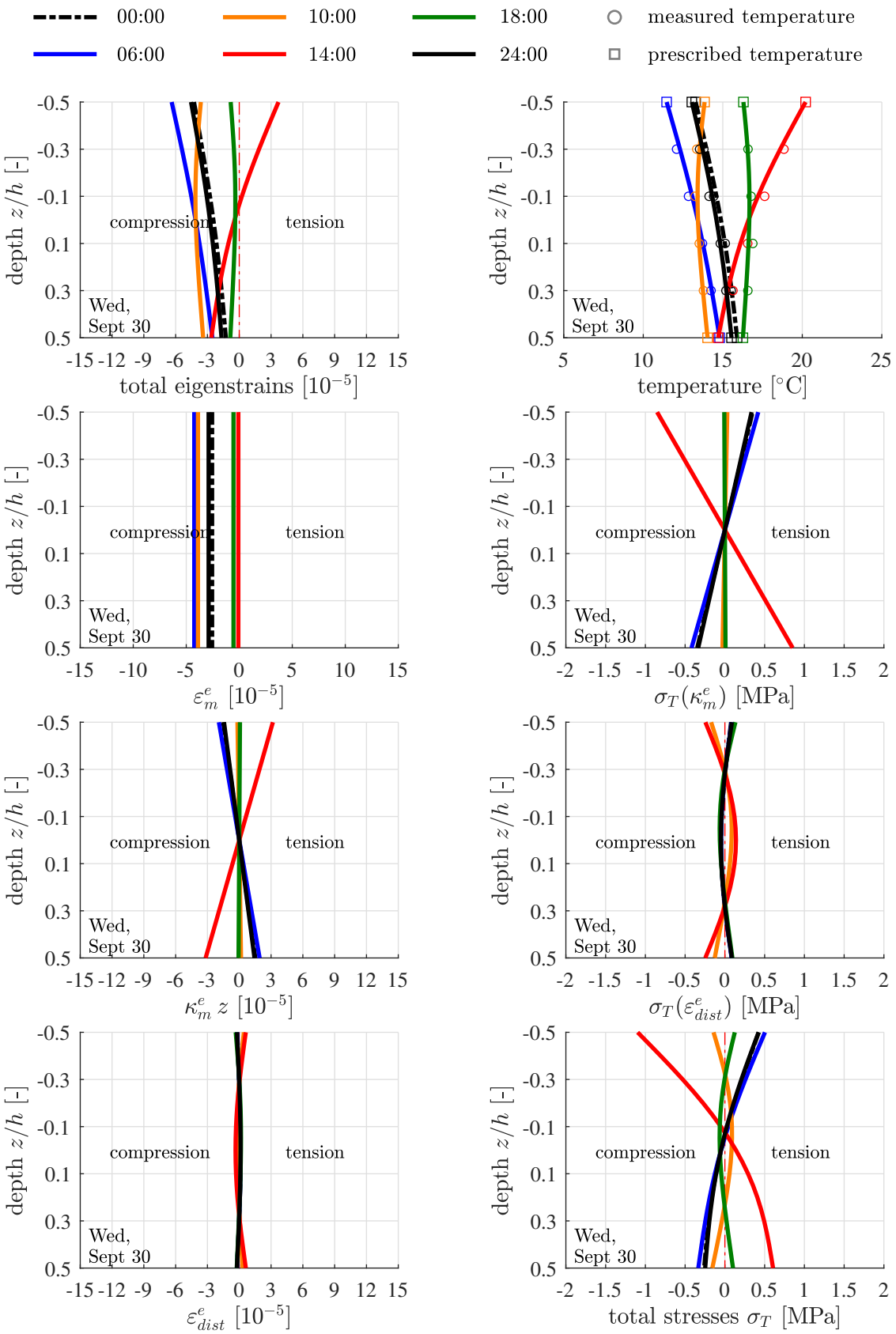

Fig. A.1 [cont'd]: Results of the thermo-mechanical analysis regarding September 30

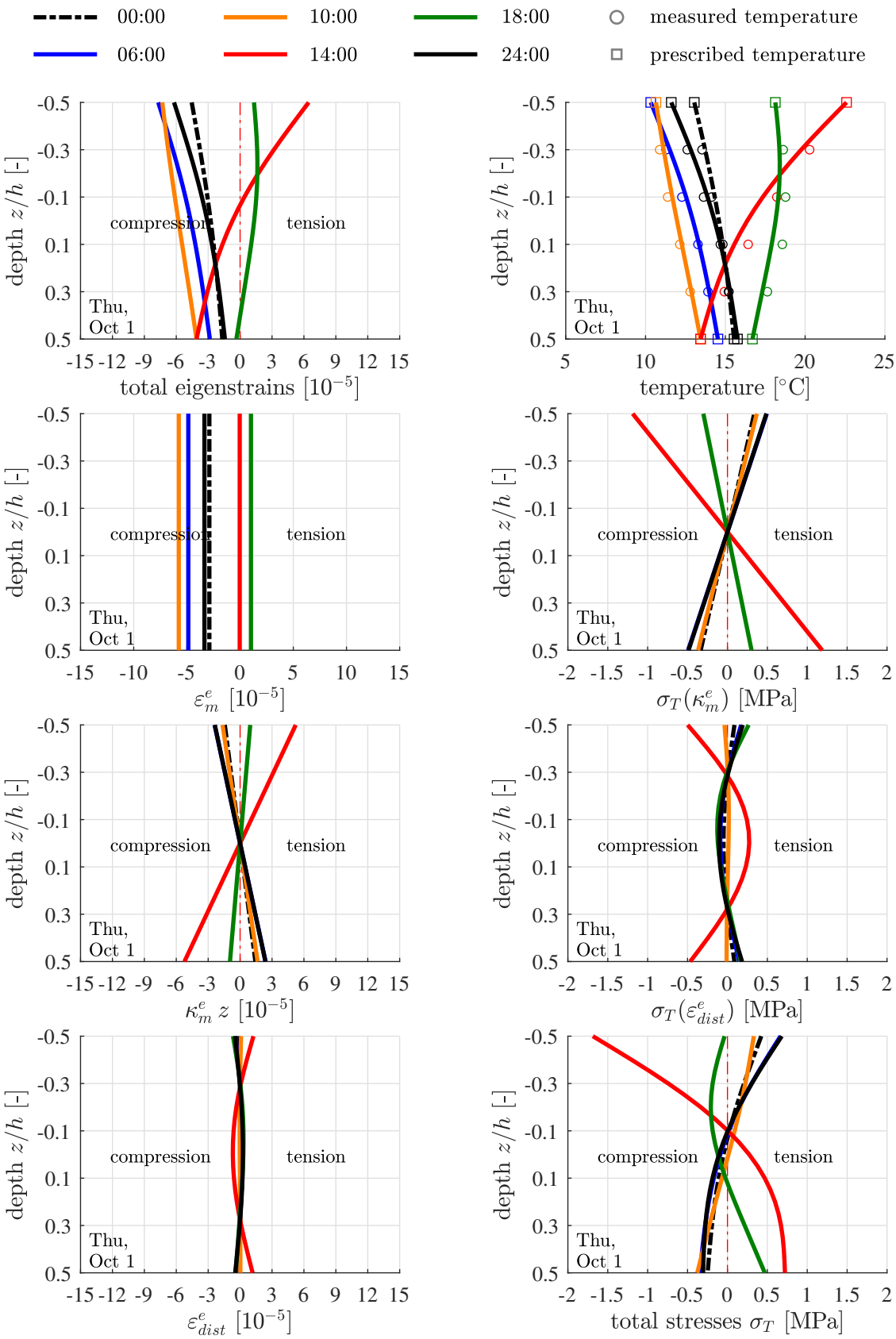

Fig. A.1 [cont'd]: Results of the thermo-mechanical analysis regarding October 1

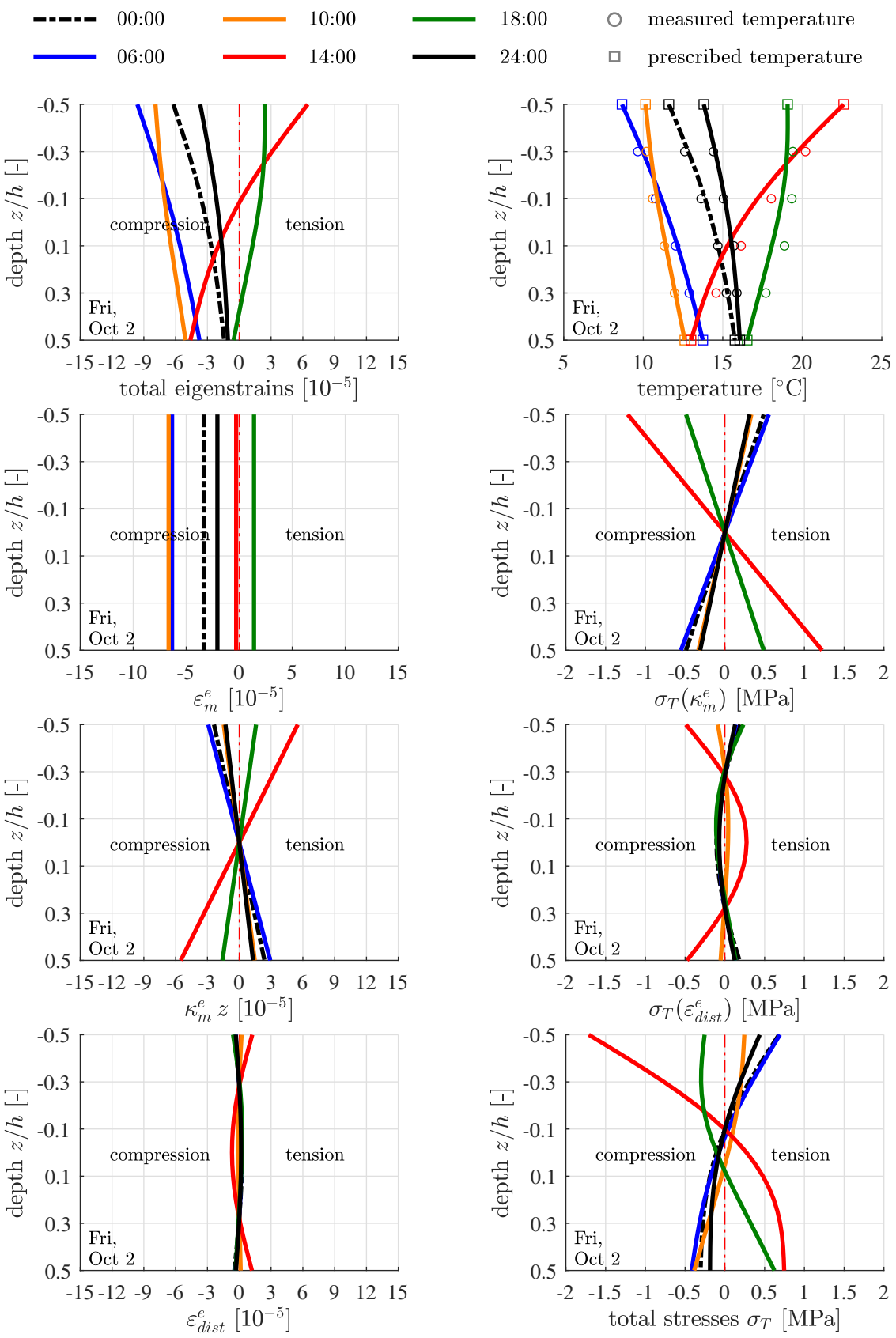

Fig. A.1 [cont'd]: Results of the thermo-mechanical analysis regarding October 2

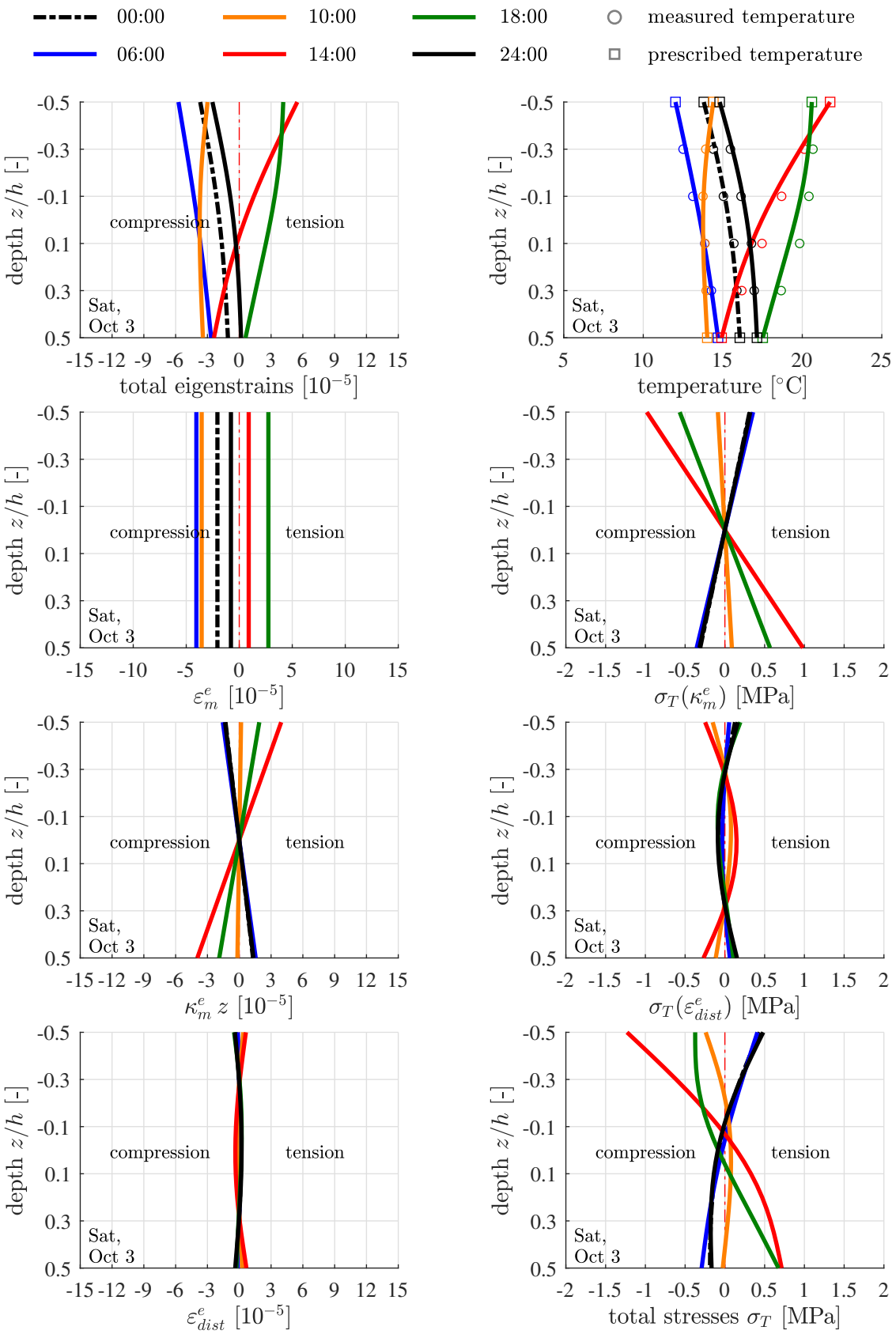

Fig. A.1 [cont'd]: Results of the thermo-mechanical analysis regarding October 3

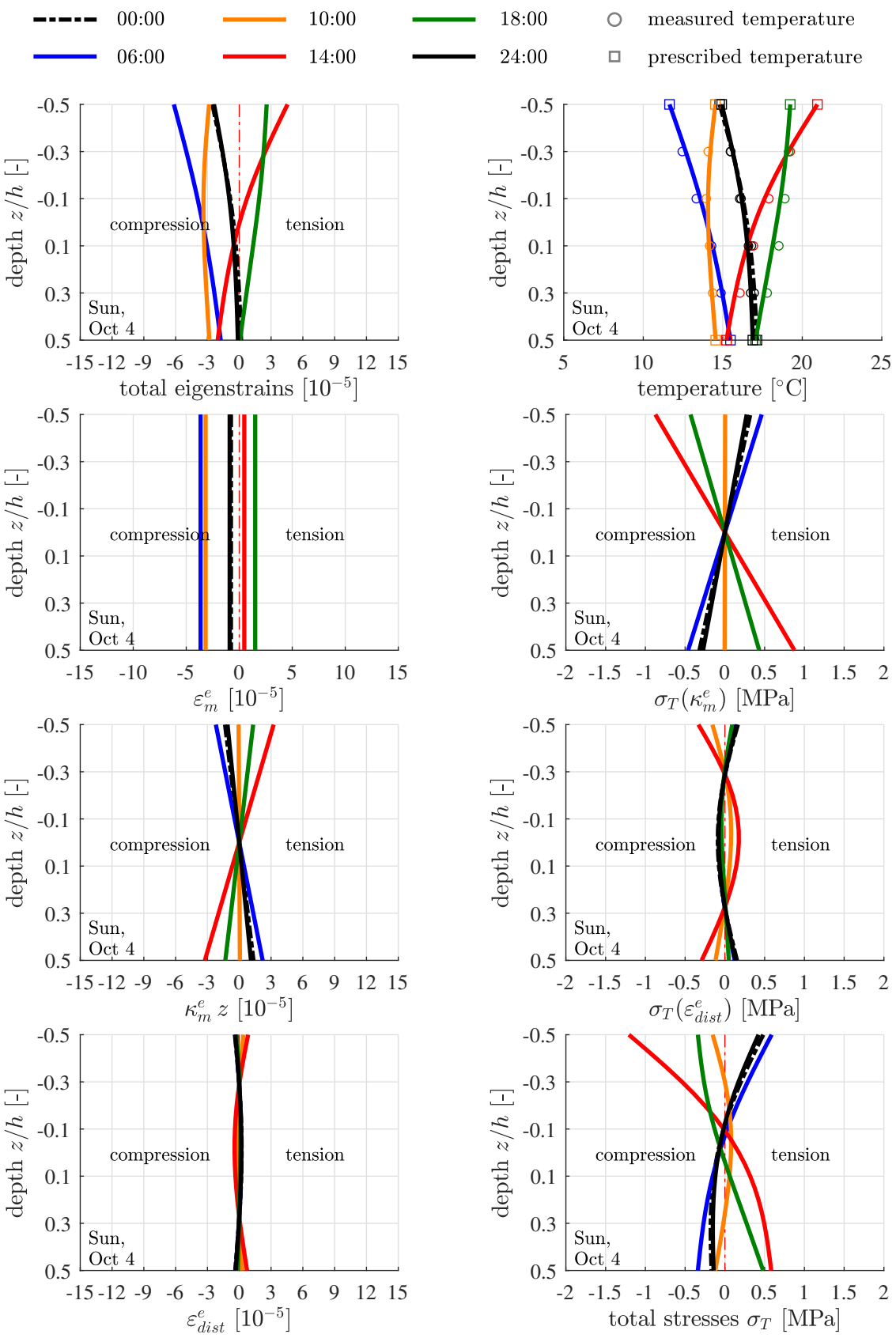

Fig. A.1 [cont'd]: Results of the thermo-mechanical analysis regarding October 4

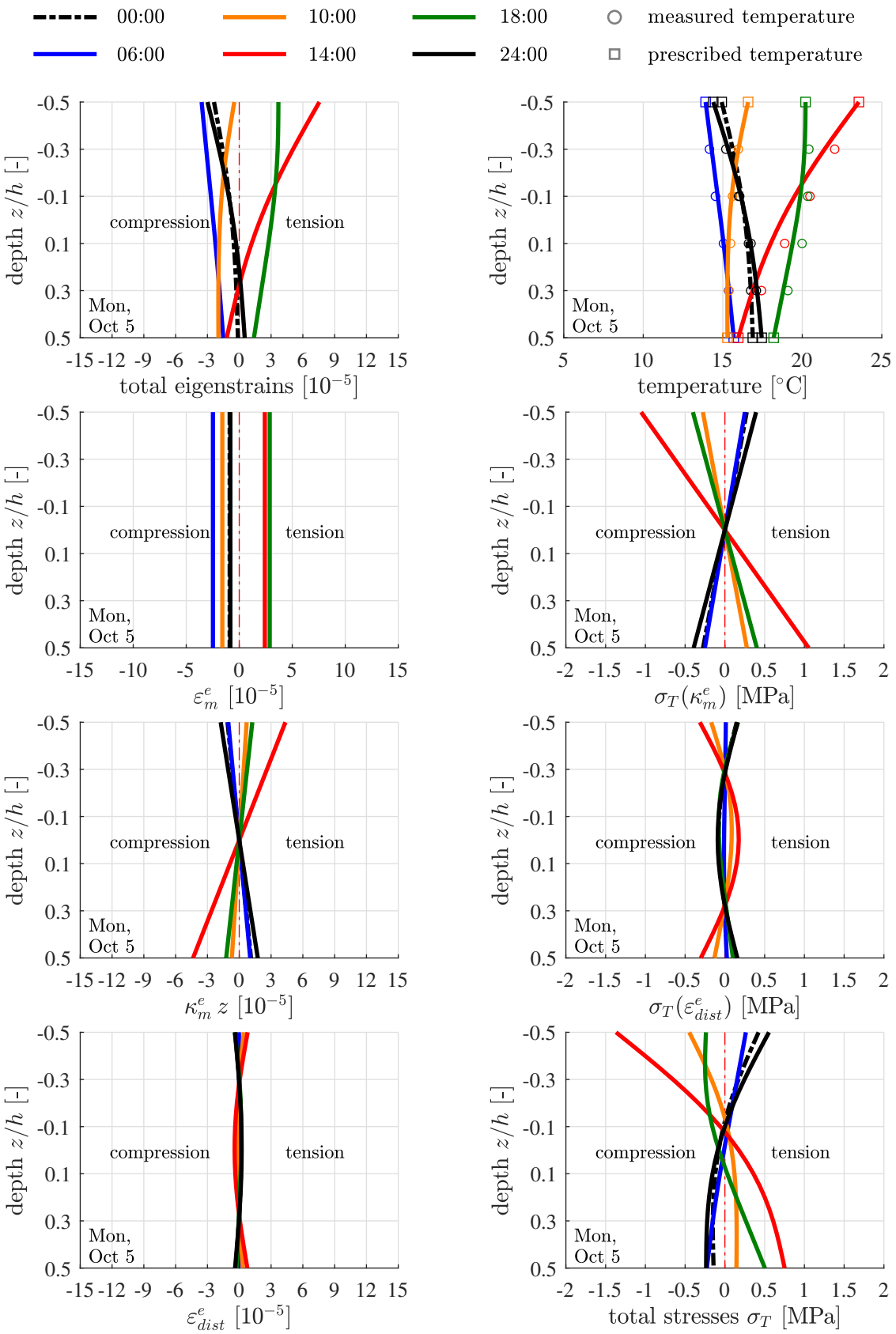

Fig. A.1 [cont'd]: Results of the thermo-mechanical analysis regarding October 5

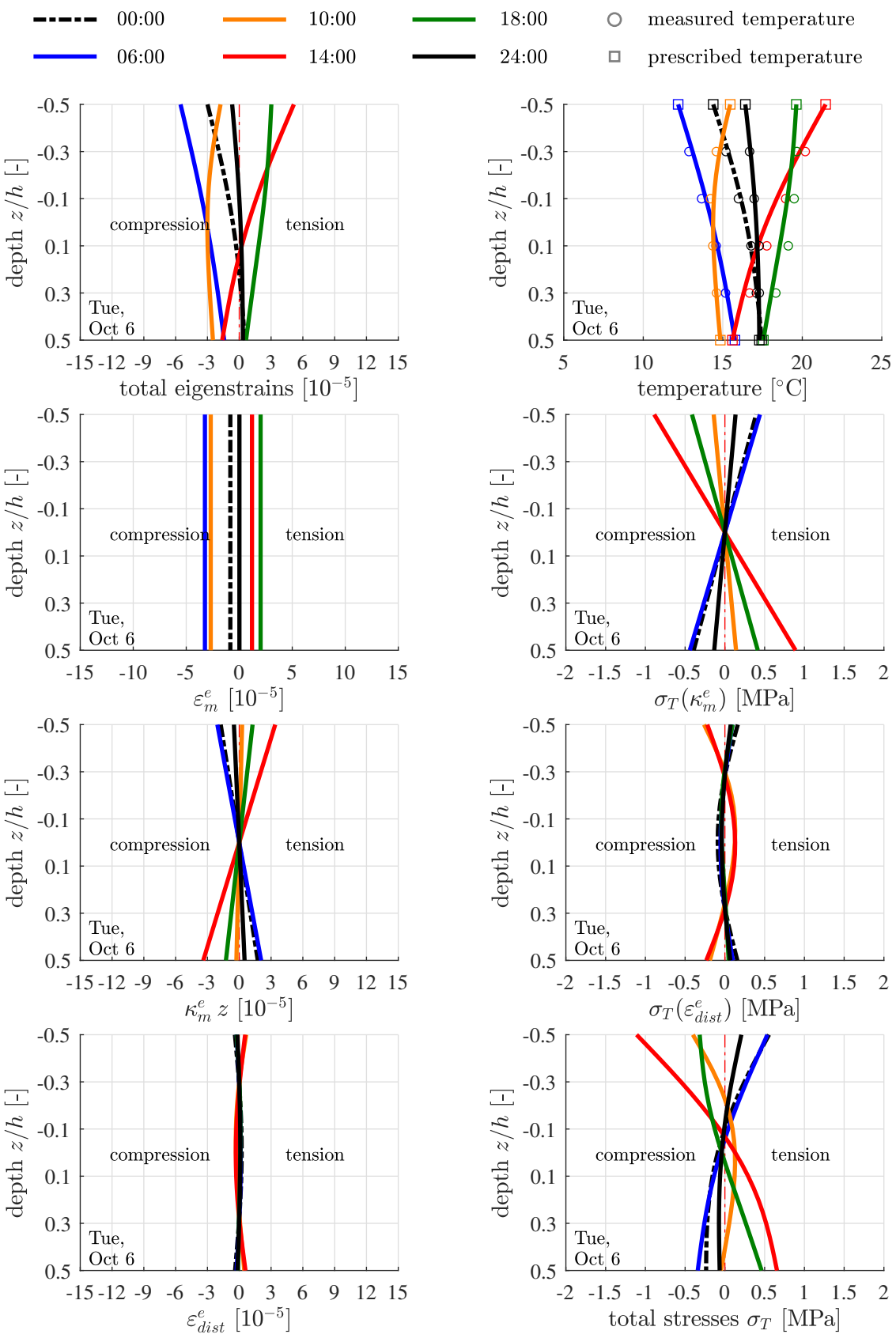

Fig. A.1 [cont'd]: Results of the thermo-mechanical analysis regarding October 6

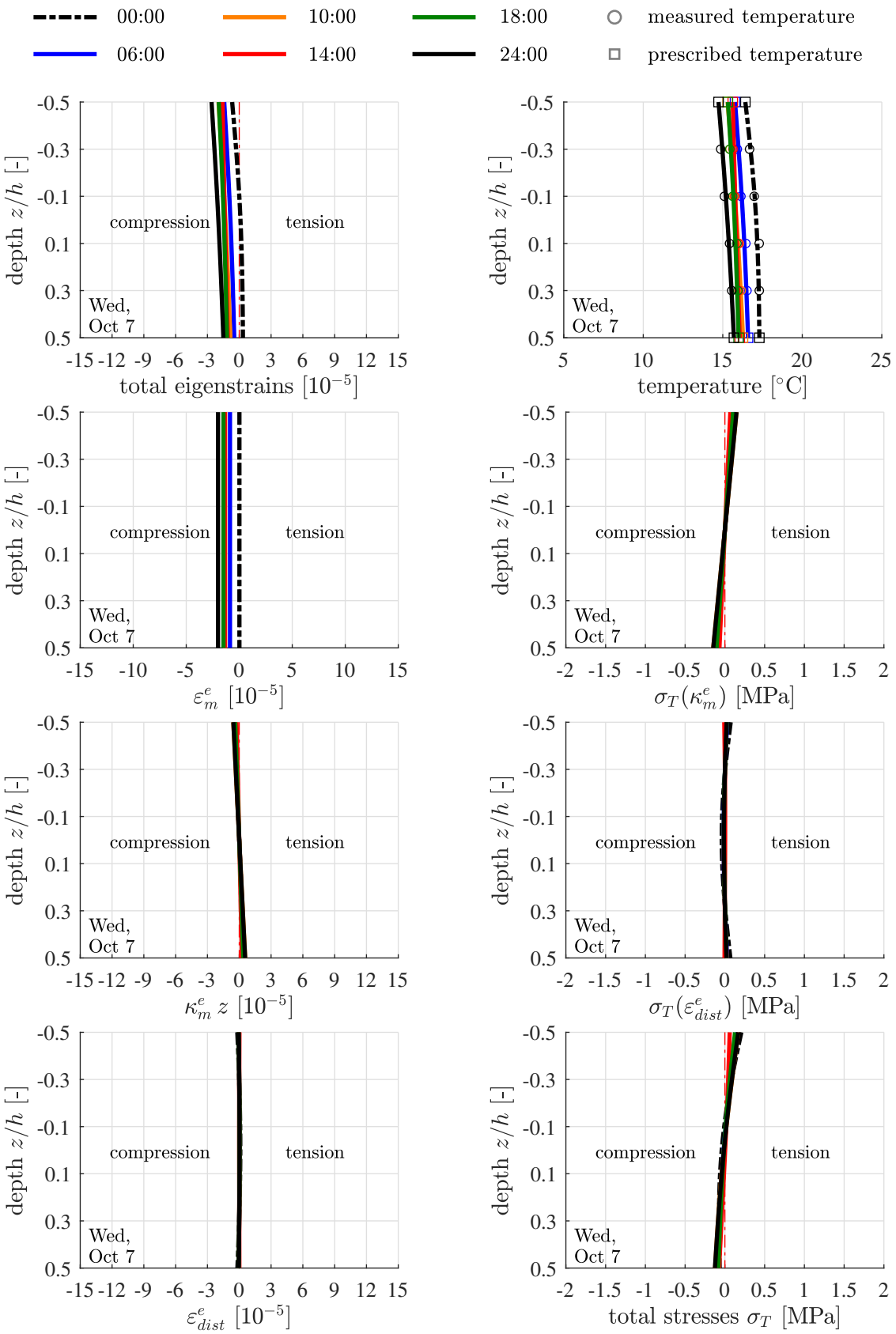

Fig. A.1 [cont'd]: Results of the thermo-mechanical analysis regarding October 7

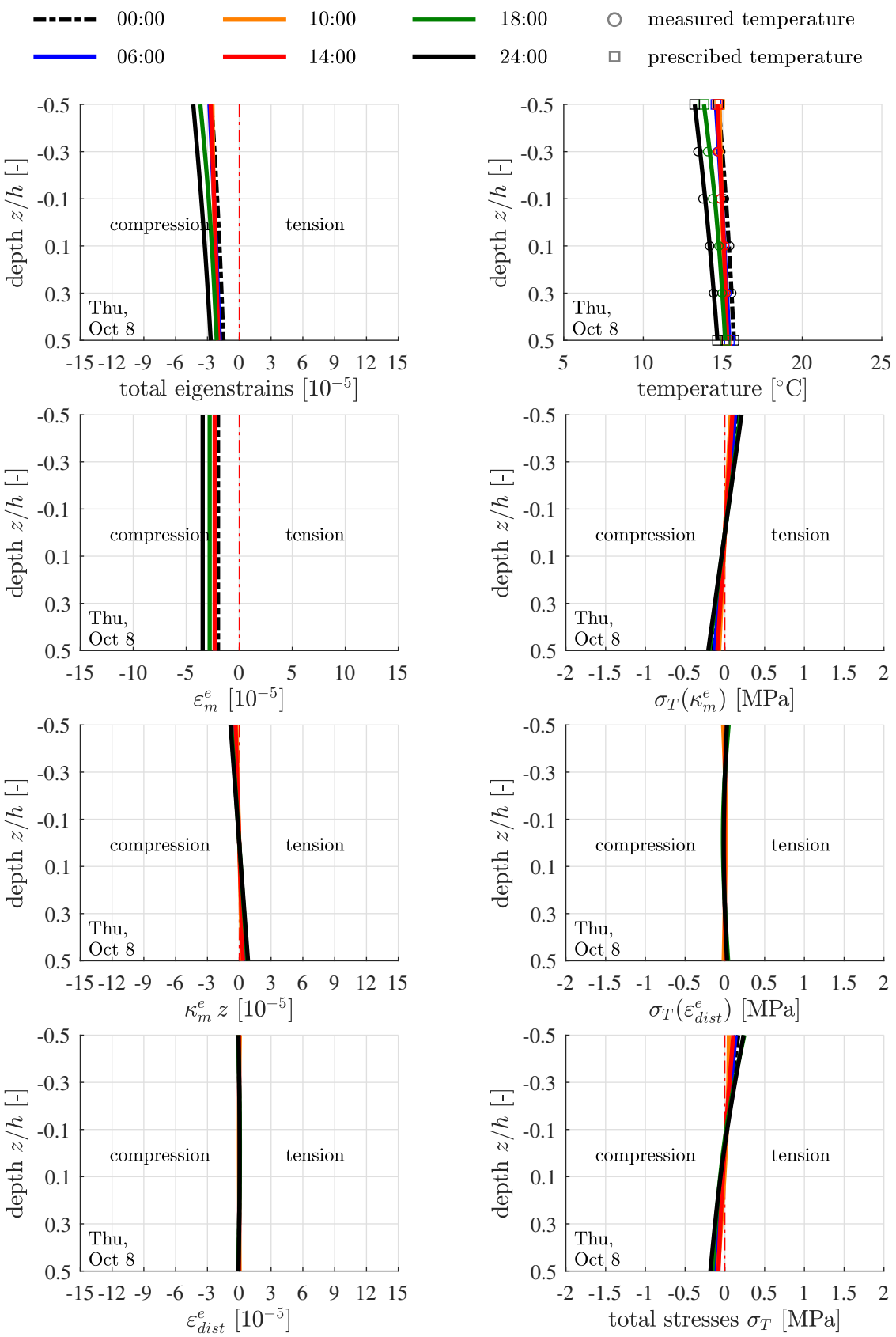

Fig. A.1 [cont'd]: Results of the thermo-mechanical analysis regarding October 8

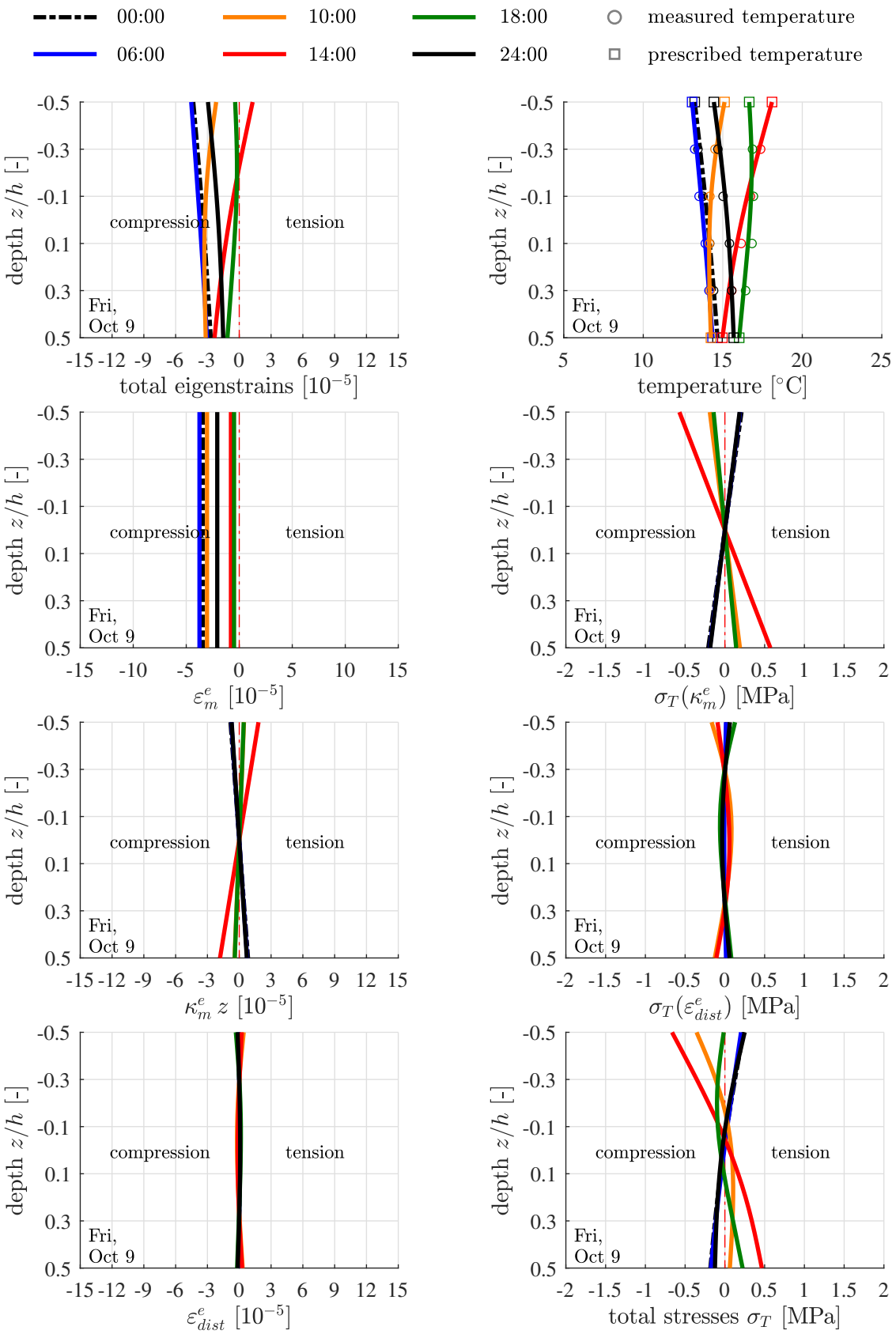

Fig. A.1 [cont'd]: Results of the thermo-mechanical analysis regarding October 9

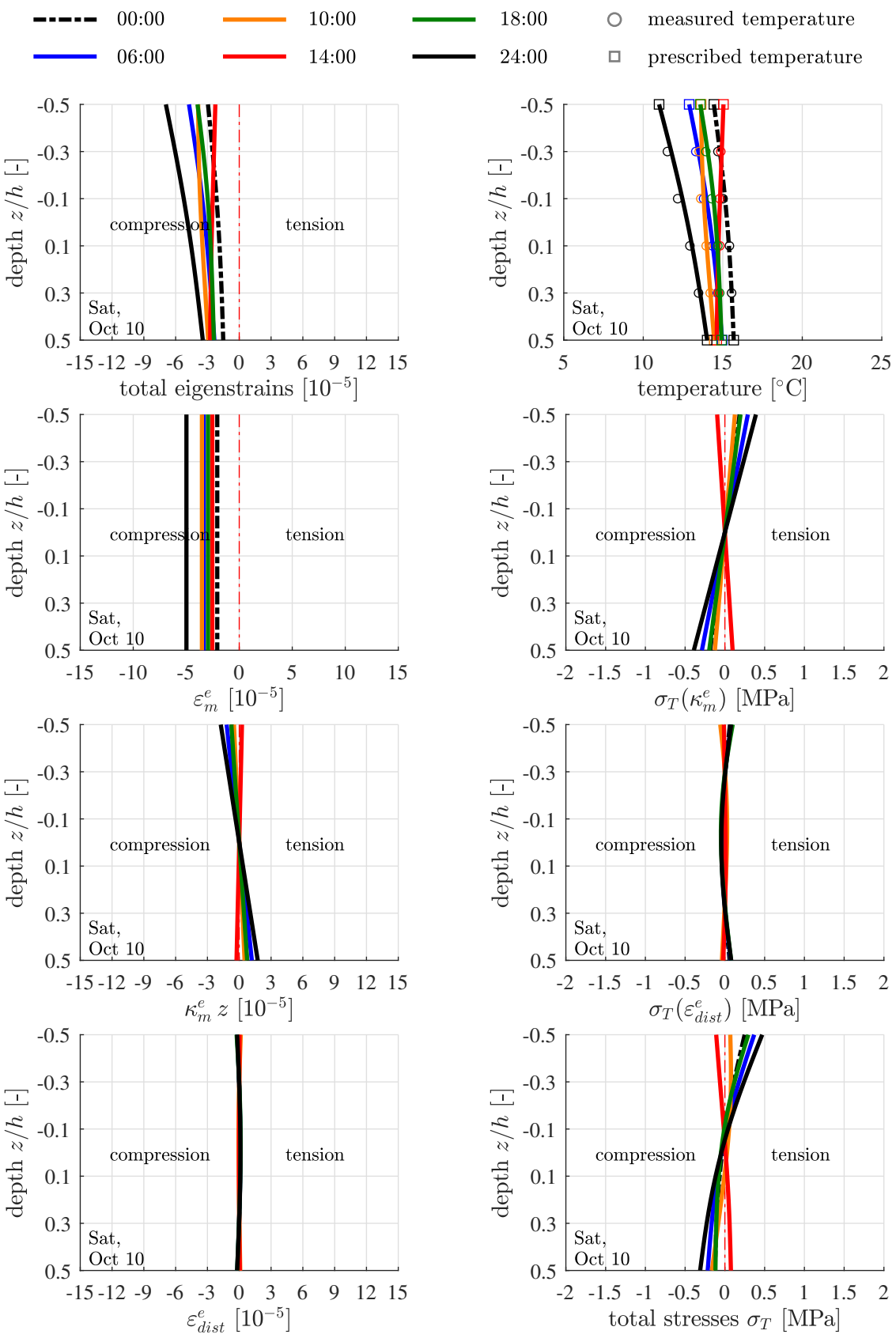

Fig. A.1 [cont'd]: Results of the thermo-mechanical analysis regarding October 10

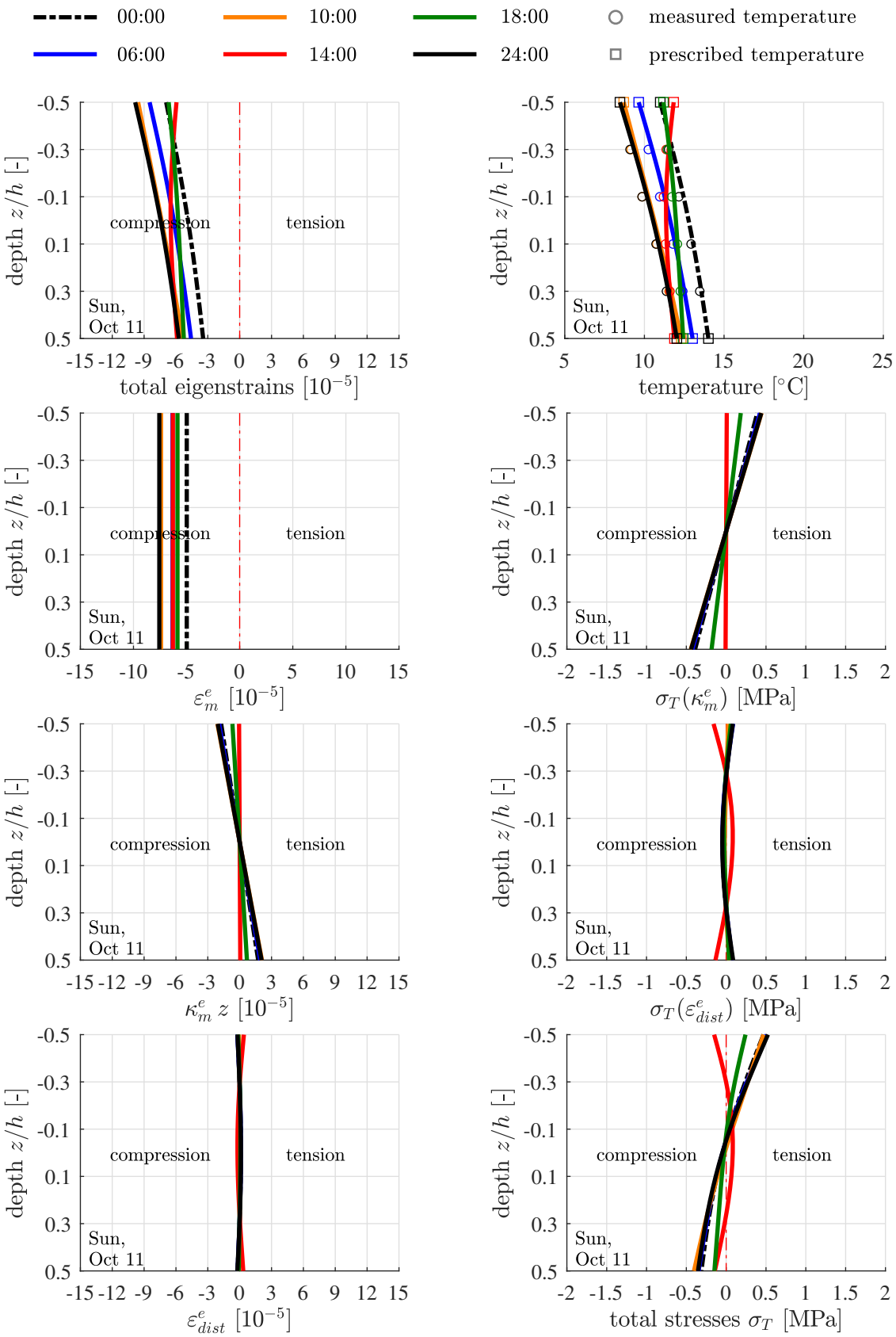

Fig. A.1 [cont'd]: Results of the thermo-mechanical analysis regarding October 11

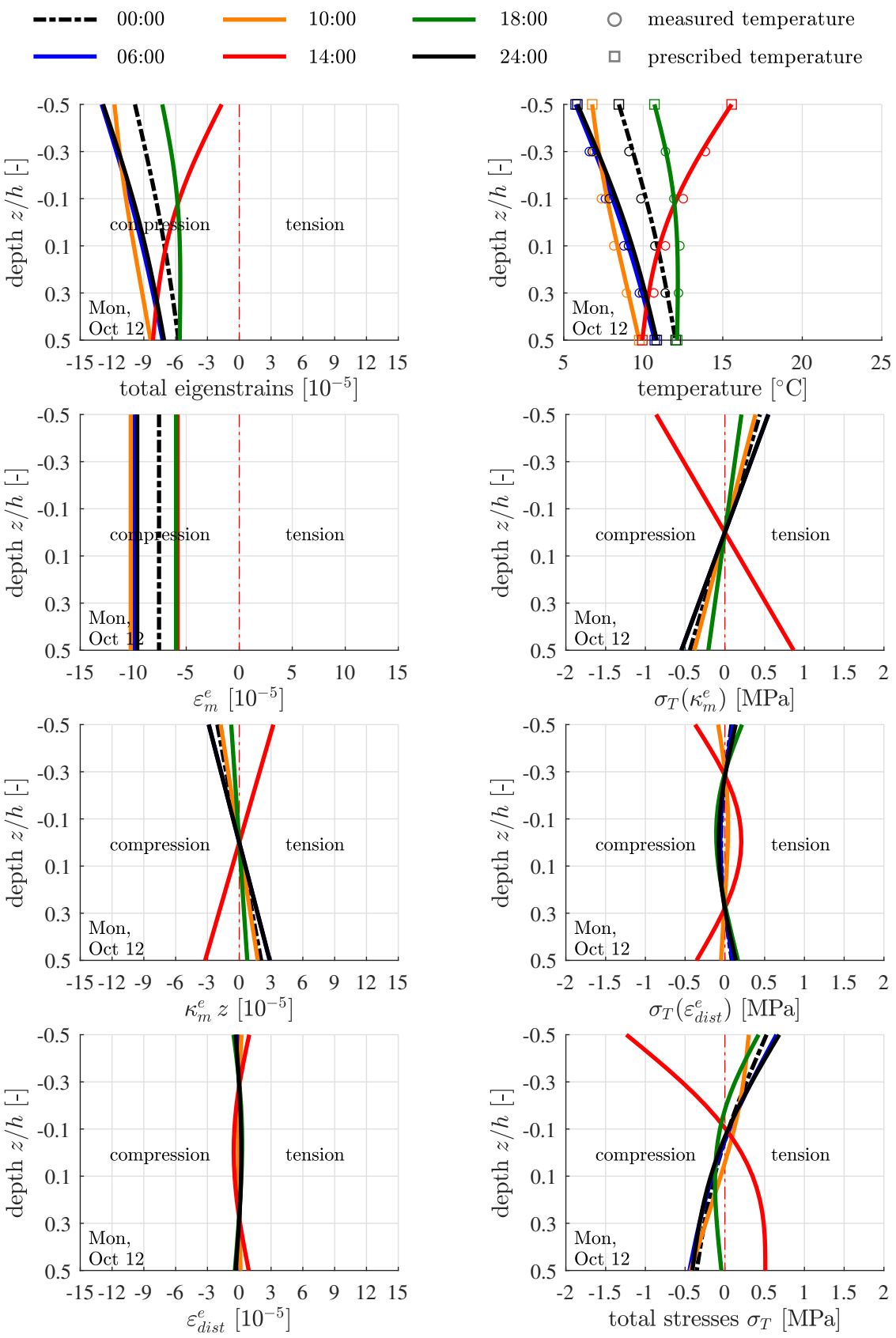

Fig. A.1 [cont'd]: Results of the thermo-mechanical analysis regarding October 12

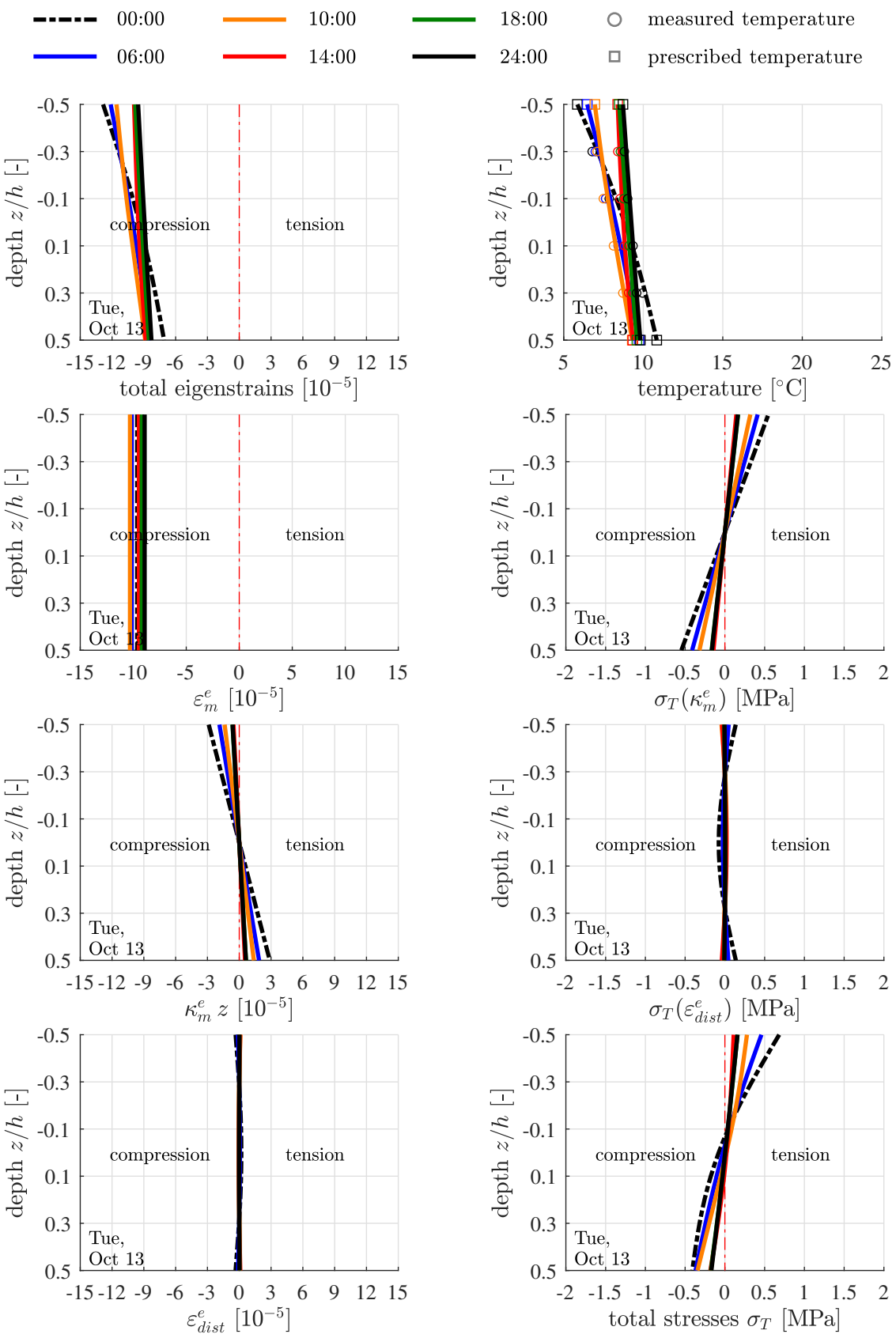

Fig. A.1 [cont'd]: Results of the thermo-mechanical analysis regarding October 13

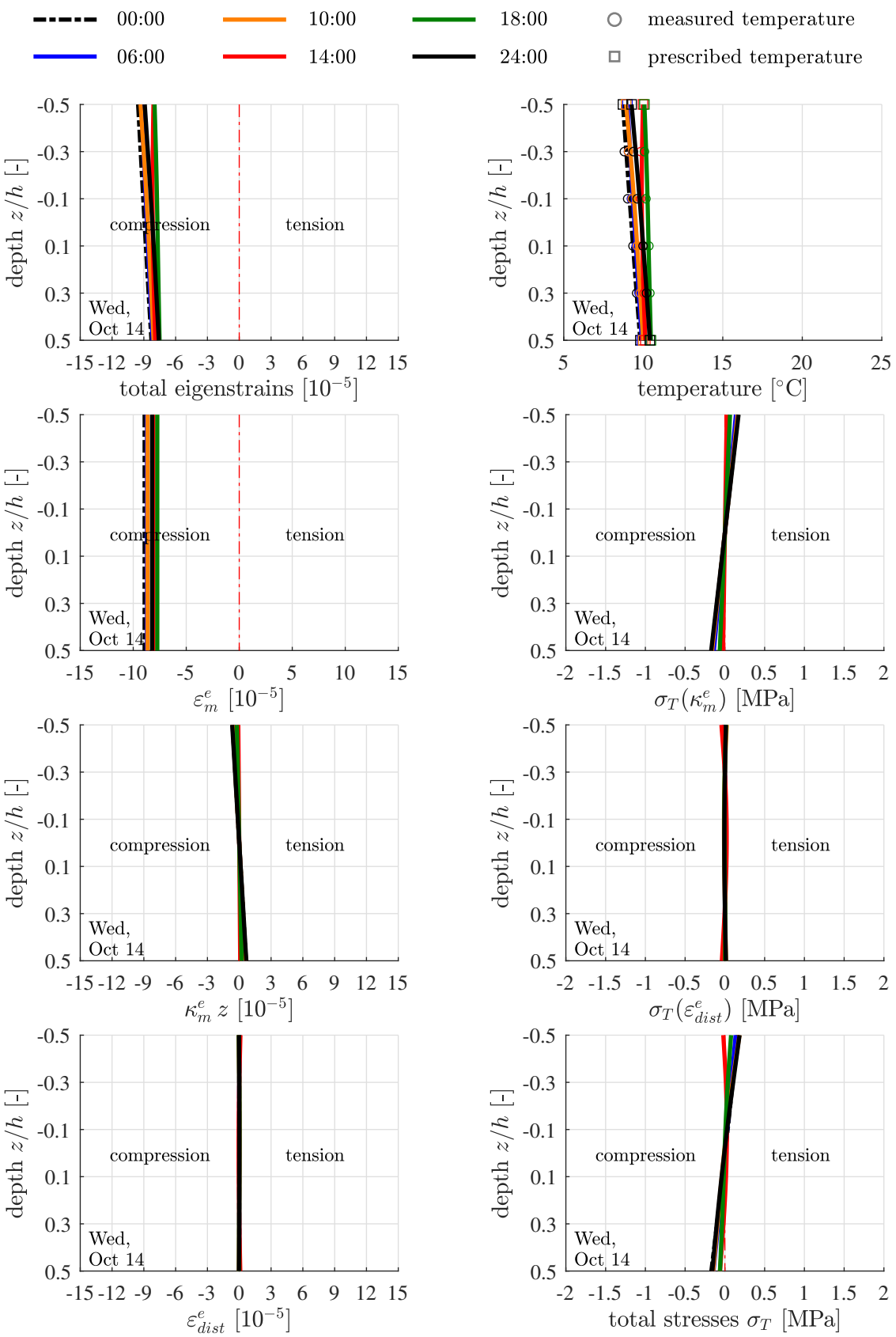

Fig. A.1 [cont'd]: Results of the thermo-mechanical analysis regarding October 14

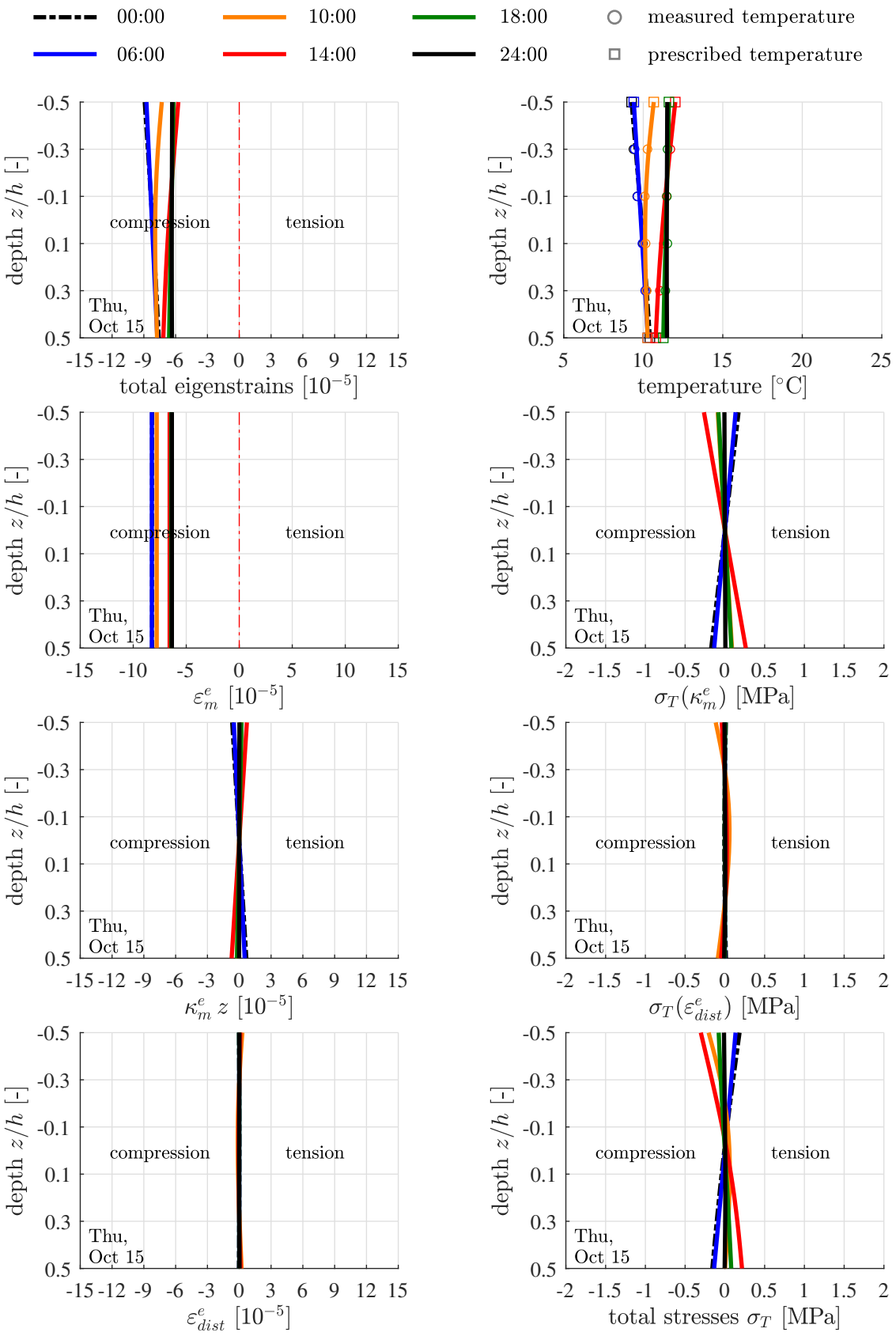

Fig. A.1 [cont'd]: Results of the thermo-mechanical analysis regarding October 15

Appendix B

List of symbols

symbol	meaning
a	thermal diffusivity of concrete
α_T	coefficient of thermal expansion of concrete
c	heat capacity of concrete
$\Delta T_i^{bot}(t)$, $\Delta T_i^{top}(t)$	i^{th} temperature step at the bottom and top surface
$\Delta T(z,t)$	change of temperature, measured relative to T_{ref}
E	modulus of elasticity of concrete
ε_{xx}, ε_{yy}	normal strain components in x- and y-direction
ε_m^e	eigenstretch of the midsurface
$\varepsilon_{m,x}$, $\varepsilon_{m,y}$	stretches of the midsurface in x- and y-direction
ε_{dist}^e	eigendistortion of the generators of the plate
$\varepsilon_{xx}^e = \varepsilon_{yy}^e = \varepsilon_{zz}^e$	eigenstrains in x-, y- and z-direction
g	gravitational acceleration
h	thickness of the plate
$H(t-t_i)$	Heaviside function
k	thermal conductivity of concrete
K	modulus of subgrade reaction of an elastic Winkler foundation
κ_m^e	eigencurvature of the midsurface
$\kappa_{m,x}$, $\kappa_{m,y}$	curvatures of the midsurface in x- and y-direction
l_x, l_y	length and width of the plate
$\max \lvert\sigma_1^{bot}\rvert$	extrem value of the principal bending stress at the bottom of the plate
m_{xx}, m_{yy}	bending moments per unit length
n_{xx}, n_{yy}	normal forces per unit length
ν	Poisson's ratio of concrete
N_i	number of considered temperature steps
p	dead load of the conrete plate
ρ	mass density of concrete
S	boundary of the plate
σ_{xx}, σ_{yy}	normal stress components of Cauchy's tensor in x- and y-direction

symbol	meaning
$\sigma_T(\varepsilon^e_{dist})$	thermal stresses resulting from eigendistortion of the generators of the plate
$\sigma_T(\kappa^e_m)$	thermal stresses resulting from eigencurvature of the plate
σ_T	total thermal stresses
t	time variable
$\langle t - t_i \rangle$	Macaulay operator
$T^{bot}(t)$, $T^{top}(t)$	temperature history at the bottom and top surface
$T(z,t)$	temperature variable
T_{ref}	reference temperature
u, v, w	displacement components in x-, y- and z-direction
u_m, v_m, w_m	displacement components in x-, y- and z-direction referring to the midplane
V	volume of the plate
x, y, z	Cartesian coordinates

Bibliography

[1] J. M. Armaghani, T. J. Larsen, and L. L. Smith. "Temperature Response of Concrete Pavements". In: *Transportation Research Record* 1121 (1987), pp. 23–33.

[2] I. Asadi, P. Shafigh, Z. F. Hassan, and N. B. Mahyuddin. "Thermal conductivity of concrete – A review". In: *Journal of Building Engineering* 20 (2018), pp. 81–93.

[3] Asfinag. *Autobahnnetz*. 2020. URL: `http://services.asfinag.at/web/trafficdata/poi-highways` (visited on 10/14/2020).

[4] M. Ausweger. "Spannungen und Verformungen gerader Einzelstäbe zufolge Temperaturbeanspruchung". Bachelorarbeit. Technische Universität Wien, 2016.

[5] H. Bing, G. W. Chai, R. van Staden, and H. Guan. "Development of Prediction Model for Doweled Joint Concrete Pavement Using Three-Dimensional Finite Element Analysis". In: *Applied Mechanics and Materials* 587-589 (2014), pp. 1047–1057.

[6] B. Choubane and M. Tia. "Nonlinear Temperature Gradient Effect on Maximum Warping Stresses in Rigid Pavements". In: *Transportation Research Record* 1370 (1992), pp. 11–19.

[7] Dlubal Software GmbH. *RFEM – FEM Structural Analysis Software*. Am Zellweg 2, 93464 Tiefenbach, Germany, 2020.

[8] L. Eberhardsteiner, K. Foltin, K. Bayraktarova, K. Haselbauer, B. Pichler, M. Aminbaghai, P. Pratscher, and R. Blab. *Optimierte Bemessung starrer Aufbauten von Straßen (OBESTAS)*. Research rep. Bundesministerium für Verkehr, Innovation und Technologie; ÖBB-Infrastruktur AG; ASFINAG, 2016. 147 pp.

[9] M. Eisenberger and J. Clastornik. "Vibrations and Buckling of a beam on a variable Winkler elastic foundation". In: *Journal of Sound and Vibration* 115(2) (1987), pp. 233–241.

[10] M. M. Elbadry and A. Ghali. "Temperature variations in concrete bridges". In: *Journal of Structural Engineering* 109 (1983), pp. 2355–2374.

[11] Å. Hermansson. "Mathematical model for paved surface summer and winter temperature: comparison of calculated and measured temperatures". In: *Cold Regions Science and Technology* 40 (2004), pp. 1–17.

[12] J. E. Hiller and J. R. Roesler. "Simplified Nonlinear Temperature Curling Analysis for Jointed Concrete Pavements". In: *Journal of Transportation Engineering* 136 (2010), pp. 654–663.

[13] R. Höller, M. Aminbaghai, L. Eberhardsteiner, J. Eberhardsteiner, R. Blab, B. Pichler, and C. Hellmich. "Rigorous amendment of Vlasov's theory for thin elastic plates on elastic Winkler foundations, based on the Principle of Virtual Power". In: *European Journal of Mechanics/ A Solids* 73 (2019), pp. 449–482.

[14] International Federation for Structural Concrete (fib—Fédération Internationale du Béton). *fib Model Code for Concrete Structures 2010*. Berlin: Ernst & Sohn, 2010. ISBN: 978-3-433-03061-5.

[15] A. M. Ioannides and L. Khazanovich. "Nonlinear temperature effects on multilayered concrete pavements". In: *Journal of transportation engineering* 124 (1998), pp. 128–136.

[16] K.-H. Kim, S.-E. Jeon, J.-K. Kim, and S. Yang. "An experimental study on thermal conductivity of concrete". In: *Cement and Concrete Research* 33 (2003), pp. 363–371.

[17] C.-M. Kuo, K. T. Hall, and M. I. Darter. "Three-dimensional Finite Element Model for analysis of concrete pavement support". In: *Transportation Research Record* 1505 (1995), pp. 119–127.

[18] P. Mackiewicz. "Thermal stress analysis of jointed plane in concrete pavements". In: *Applied Thermal Engineering* 73 (2014), pp. 1169–1176.

[19] H. A. Mang and G. Hofstetter. *Festigkeitslehre*. 4th ed. Berlin Heidelberg: Springer Vieweg, 2013. ISBN: 978-3-642-40751-2.

[20] A. R. Mohamed and W. Hansen. "Effect of Nonlinear Temperature Gradient on Curling Stress in Concrete Pavements". In: *Transportation Research Record 1568* 970813 (1997), pp. 65–71.

[21] J. Murin, M. Aminbaghai, V. Kutis, and J. Hrabovsky. "Modal analysis of the FGM beams with effect of axial force underlongitudinal variable elastic Winkler foundation". In: *Engineering Structures* 49 (2013), pp. 234–247.

[22] *ÖNORM EN 1992-1-2: 2019-11-01: Bemessung und Konstruktion von Stahlbeton- und Spannbetontragwerken. Teil 1-2: Allgemeine Regeln – Tragwerksbemessung für den Brandfall*. Wien: Austrian Standards, Nov. 2019.

[23] P. Rahn and A. D. e. a. Biehler. *Mechanistic-Empirical Pavement Design Guide. A Manual of Practice*. Washington: American Association of State Highway and Transportation Officials, 2008. ISBN: 978-1-56051-423-7.

[24] *RVS: Richtlinie und Vorschriften für das Straßenwesen*. Wien: Bundesministerium für Verkehr, Innovation und Technologie and Forschungsgesellschaft Straße – Schiene – Verkehr, Mar. 2020.

[25] Z. Q. Siddique, M. Hossain, and D. Meggers. "Temperature and Curling Measurements on Concrete Pavement". In: Proceedings of the Mid-Continent Transportation Research Symposium 2005. Ames, Iowa, USA, 2005, pp. 1–12.

[26] A. M. Tabatabaie and E. J. Barenberg. "Finite-Element Analysis of Jointed or Cracked Concrete Pavements". In: *Transportation Research Record* 671 (1978), pp. 11–19.

[27] L. Teller and C. Sutherland. "The structural design of concrete pavements; parts 1+2". In: *Division of tests, bureau of public roads* 16(8-9) (1935), pp. 145–189.

[28] J. Thomlinson. "Temperature variations and consequent stresses produced by daily and seasonal temperature cycles in concrete slabs". In: *Concrete Constructional Engineering* 36(6) (1940), pp. 298–307.

[29] Time and D. AS. *Wetterrückblick für Bad Vöslau, Niederösterreich, Österreich – Oktober 2015*. 2020. URL: `https://www.timeanddate.de/wetter/oesterreich/bad-voeslau/rueckblick?month=10&year=2015` (visited on 10/15/2020).

[30] V. Z. Vlasov and N. N. Leont'ev. *Beams, plates and shells on elastic foundations*. Jerusalem: Israel Program for Scientific Translations, 1966.

[31] H. Wang, R. Höller, M. Aminbaghai, C. Hellmich, Y. Yuan, H. Mang, and B. L. Pichler. "Concrete pavements subjected to hail showers: A semi-analytical thermoelastic multiscale analysis". In: *Engineering Structures* 200 (109677) (2019).

[32] H. Westergaard. "Analysis of stresses in concrete pavements due to variations of temperature". In: Highway research board proceddings. Vol. 6. Washington, USA, 1927, pp. 201–215.

[33] E. Winkler. *Die Lehre von der Elasticitaet und Festigkeit: mit besonderer Rücksicht auf ihre Anwendung in der Technik; für polytechnische Schulen, Bauakademien, Ingenieure, Maschinenbauer, Architekten etc. [Lessons on elasticity and strength of materials: with special consideration of their application in technology; for polytechnical schools, building academies, engineers, mechanical engineers, architects,etc]*. Prague: Dominicus, 1867.

[34] J. Zhang, T. Fwa, K. Tan, and X. Shi. "Model for Nonlinear Thermal Effect on Pavement Warping Stresses". In: *Journal of Transportation Engineering* 129 (2003), pp. 695–702.